Monitoring of a geothermal borehole field: Data analysis and calibration of a prediction model

Auteur : Rouxhet, Théo
Promoteur(s) : François, Bertrand
Faculté : Faculté des Sciences appliquées
Diplôme : Master en ingénieur civil des mines et géologue, à finalité spécialisée en géologie de l'ingénieur et de l'environnement
Année académique : 2024-2025
URI/URL : http://hdl.handle.net/2268.2/23288

UNIVERSITE DE LIEGE
FACULTE DES SCIENCES APPLIQUEES

Monitoring of a geothermal borehole field: Data analysis and calibration of a prediction model

ROUXHET Théo

Thesis presented to obtain the degree of:

Master of Science in Geological and Mining Engineering,

professional focus in environmental and geological engineering

Thesis supervisor:
FRANÇOIS Bertrand

Other jury members:
ORBAN Philippe
GERARD Pierre

Academic year: **2024 - 2025**

Abstract

Near-surface closed-loop geothermal systems have an important role to play in the decarbonisation of energy. Thanks to their ability to reduce greenhouse gas emissions and their widespread availability throughout the year, it is essential that these technologies are supported by appropriate design studies to ensure their long-term performance and sustainability.

This master thesis aims to analyse the monitoring data from an existing geothermal installation and to calibrate an analytical heat transfer model to reproduce the evolution of underground temperatures. The datasets come from the heat pump system of the "Relais des Ingénieurs" residence in Louvain-la-Neuve. A preliminary filtering and analysis of the raw datasets were required to address interruptions in geothermal system operation and anomalies in data acquisition, allowing for the computation of the thermal load extracted from the ground. In a second step, a considerable portion of the data was excluded due to abnormally high thermal loads, resulting in a reduced analysis period representing approximately 15% of the total monitoring duration. The analytical model developed by Erol et al. (2015), designed to simulate the thermal response of multiple borehole heat exchangers and capable of accounting for discontinuous extractions and groundwater flow, is then calibrated.

Main model parameters, including initial ground temperature, the thermal conductivity of the ground, grout, and pipe, volumetric heat capacity, and specific discharge, are calibrated sequentially to minimise the discrepancy between simulated and monitored fluid temperatures. The model fit is assessed using error metrics such as the root mean square error and mean absolute error. Calibration is conducted for both daily and hourly thermal loads. Results show that the model can accurately reproduce measured temperatures when properly calibrated, highlighting the value of data monitoring in improving geothermal model predictions and system design, especially when daily thermal loads are used.

Despite the limitations of the available data, the study proves robust and could be enhanced through improved instrumentation and longer monitoring campaigns.

Acknowledgments

I would like to express my sincere gratitude to all those who have contributed, directly or indirectly, to the completion of this Master's thesis.

I am particularly grateful to my supervisor, Mr. Bertrand François, for his continuous support, valuable guidance, and numerous pieces of advice throughout this work.

I would also like to thank the other members of the jury for the time and attention they dedicated to evaluating my work.

I also extend my thanks to Mr. William Verschure, project operator at Karno, for the time he devoted to helping me better understand the dataset through our numerous phone discussions.

I warmly thank my family; my parents, my brothers, my sister, and my grandmother, for their constant encouragement and steadfast support, both for this project and throughout my entire academic path.

Finally, I wish to thank my classmates from the second year of the Master's programme in Geology, without whom the last two years would not have been the same.

Contents

1 Introduction **1**
1.1 Context . . . 1
1.2 Objectives and content of the work . . . 3

2 State of the art **5**
2.1 Geothermal energy . . . 5
2.1.1 Origin and history . . . 5
2.1.2 Advantages . . . 6
2.2 Geothermal systems . . . 8
2.2.1 General principles . . . 8
2.2.2 Near-surface geothermal systems . . . 10
2.3 Heat pumps . . . 14
2.3.1 General principles . . . 14
2.3.2 Performance coefficients . . . 15
2.4 Heat transfer processes . . . 16
2.4.1 Heat conduction . . . 17
2.4.2 Heat advection and convection . . . 18
2.4.3 Thermal dispersion . . . 18
2.4.4 Heat conservation equation in saturated porous media . . . 18
2.5 Temperature modelling . . . 19
2.5.1 Infinite line source model . . . 19
2.5.2 Finite line source model . . . 20
2.5.3 Infinite cylindrical source model . . . 22
2.5.4 Conclusion . . . 22

3 General context of the Relais des Ingénieurs site **24**
3.1 Geographical Context . . . 24
3.2 Geological context . . . 26
3.3 Hydrogeological context . . . 30

4 Analytical model **33**
4.1 Main equations . . . 33
4.2 Input parameters . . . 35

5 Datasets **38**
5.1 Dataset 1 . . . 38
5.1.1 Description . . . 38

5.1.2 Analysis . . . 39
5.2 Dataset 2 . . . 47
5.2.1 Description . . . 47
5.2.2 Analysis . . . 48

6 Calibration **50**
6.1 Thermal load . . . 50
6.2 Initial ground temperature . . . 53
6.2.1 Daily thermal loads . . . 53
6.2.2 Hourly thermal loads . . . 55
6.3 Thermal conductivity . . . 56
6.3.1 Daily thermal loads . . . 57
6.3.2 Hourly thermal loads . . . 58
6.4 Volumetric heat capacity . . . 59
6.4.1 Daily thermal loads . . . 59
6.4.2 Hourly thermal loads . . . 61
6.5 Borehole thermal resistance . . . 62
6.5.1 Grout thermal conductivity . . . 62
6.5.2 Probe thermal conductivity . . . 65
6.6 Groundwater specific discharge . . . 66
6.6.1 Daily thermal loads . . . 67
6.6.2 Hourly thermal loads . . . 72
6.7 Adaptation of the geothermal system . . . 75

7 Conclusions and perspectives **77**

Bibliography **79**

Appendices **82**
A.1 Regional geology . . . 82
A.2 Drilling report . . . 86
A.3 Flow meters for the flow rate . . . 90
A.4 Estimation of glycol-water (20%) mixture properties . . . 90
A.5 Hydraulic layout of the RDI . . . 92
A.6 DHW tank and heat pump inlet temperature evolutions . . . 94
A.7 Hourly evolution of the two circuits temperatures . . . 94
A.8 Hourly evolution of extracted ground energy over time . . . 95
A.9 Specific discharge . . . 96

List of Figures

1.1 Final energy consumption in households, EU, 2022 (%) (Eurostat, 2023). 2
1.2 Final energy consumption in the residential sector by use, EU, 2022 (Terajoules (TJ)) (modified from Eurostat, 2023). 2
1.3 Share of different sectors in total emissions in Belgium in 2023 (modified from "Émissions par secteur", n.d.). 3

2.1 Generalized rate of temperature increase with depth within Earth (Earle, 2015). 5
2.2 Ruins of the Roman bathing facility at the thermal springs of Badenweiler in the Rhine rift valley (southern Germany) (Stober & Bucher, 2021). 6
2.3 Relationship between surface air temperature and ground temperature (Preene & Powrie, 2009). 7
2.4 Open-loop geothermal system with a well-doublet (Dassargues, 2019). 10
2.5 Illustration of the basic working principle of a low-temperature seasonal ATES system (Bloemendal & Hartog, 2018). 11
2.6 Horizontal closed-loop systems (Mahmoud et al., 2023; Stober & Bucher, 2021). 12
2.7 General design of a borehole heat exchanger system (Stober & Bucher, 2021). 13
2.8 Schematic illustration of types of probe tube design (Stober & Bucher, 2021). 14
2.9 Basic layout of geothermal heat pump system (Self et al., 2013). 15
2.10 Contribution of the ground and external power for a COP of 4 (modified from Dassargues and François, 2024). 16
2.11 Temperature profile in the ground given by the ILS model (parameters are listed in TABLE 2.3) (Philippe et al., 2009). 20
2.12 Temperature profile around the borehole (which extends from z = 0 to 100 m at r = 0) given by the FLS model at t = 6 months (Philippe et al., 2009). 21
2.13 Isotherm curves in steady state for the FLS mode, representing the long-term temperature distribution once thermal equilibrium is reached. 22

3.1 Location of the Relais des Ingénieurs in the Walloon Brabant region (modified from "Portail cartographique", 2024). 25
3.2 Location of the Relais des Ingénieurs in its neighbourhood (modified from "WalOnMap", 2025). 26
3.3 Geological context near the RDI site (modified from "WalOnMap", 2025). 28
3.4 Regional hydrogeological map of Wavre-Chaumont-Gistoux (modified from Ruthy, 2017). 31
3.5 Legend for FIGURE 3.4 (Ruthy, 2017). 32
3.6 Cross-section from the hydrogeological map of Wavre-Chaumont-Gistoux (FIGURE 3.4) (modified from Ruthy, 2017). 32

5.1 Evolution of ground temperature with raw data. 40
5.2 Hourly and daily mean ground temperatures, filtered to exclude inactive periods except during the summer shutdown (green arrow) for continuity. 41
5.3 Temperature evolution in the domestic hot water tank and at the inlet of the Heat Pump (HP) on the primary circuit, from 02/11/2024 to 05/11/2024. 42
5.4 Daily evolution of heat pump inlet and outlet temperatures for the primary and secondary loops, distinguishing between domestic hot water and heating operation modes. 44
5.5 Hourly evolution of energy extracted from the ground using the nominal power. 45
5.6 Daily evolution of energy extracted from the ground using the nominal power. 46
5.7 Comparison of daily extracted ground energy using three different calculation methods. . . 47
5.8 Comparison of daily ground energy extracted using four different calculation methods. . . 49

6.1 Localisation of the geothermal system and the observation point with an observation point at the centre of the central borehole, used for model-data comparison. 50
6.2 Comparison between the modelled and monitored fluid temperature evolution when E_{ground} is computed with the four different methods. 52
6.3 Comparison between the modelled and monitored fluid temperature evolution when E_{ground} is computed at each time step and summed daily, for the period from 09/01/2024 to 11/03/2024 (corresponding to the dark blue arrow in FIGURE 6.2). 53
6.4 Comparison between modelled and monitored fluid temperature evolution for different values of the initial ground temperature T_0. 54
6.5 Comparison between the modelled and monitored fluid temperature evolution when the initial ground temperature T_0 is 10.4 °C. 55
6.6 Comparison between modelled and monitored fluid temperature evolution for different values of the initial ground temperature T_0, using hourly thermal loads. 56
6.7 Comparison between modelled and monitored ground temperature evolution for different values of the thermal conductivity k_m. 58
6.8 Comparison between modelled and monitored fluid temperature evolution for different values of the thermal conductivity k_m, using hourly thermal loads. 59
6.9 Comparison between modelled and monitored fluid temperature evolution for different values of the volumetric heat capacity $\rho_b c_b$. 60
6.10 Comparison between modelled and monitored fluid temperature evolution for different values of the volumetric heat capacity $\rho_b c_b$, using hourly thermal loads. 62
6.11 Comparison between modelled and monitored fluid temperature evolution for different values of the thermal conductivity of the grout k_b. 63
6.12 Comparison between modelled and monitored fluid temperature evolution for different values of the thermal conductivity of the filling material k_b, using hourly thermal loads. . . 65
6.13 Comparison between the average modelled fluid temperature evolution at the centre of each borehole, and the monitored fluid temperature evolution for different values of groundwater specific discharge u_x. 68
6.14 Modelled fluid temperature evolution at the centre of each borehole in the absence of groundwater flow ($u_x = 0$ m/s). 69
6.15 Modelled fluid temperature evolution at the centre of each borehole with a groundwater specific discharge of $u_x = 8.57 \cdot 10^{-7}$ m/s. 70
6.16 Configuration of the observation points located at the centre of each borehole, used to assess the spatial variability of the modelled fluid temperature under groundwater flow occurring along the x-axis. 70

6.17 Modelled temperature evolutions at multiple observation points located inside and outside the boreholes, and the monitored fluid temperature evolution, for a groundwater specific discharge of $8.57 \cdot 10^{-7}$ m/s. 71
6.18 Localisation of the geothermal system and observation points with an observation point at the centre of the central borehole and observation points outside the boreholes. 72
6.19 Comparison between the average modelled fluid temperature at the centre of each borehole and the monitored fluid temperature for different values of groundwater specific discharge u_x, using hourly thermal loads. 73
6.20 Comparison of average modelled fluid temperatures using hourly thermal loads for two configurations, showing reduced fluctuations with higher grout conductivity and specific discharge. 74
6.21 Modelled temperature evolution at multiple observation points located outside the boreholes, and the monitored fluid temperature evolution, for a groundwater specific discharge of $8.57 \cdot 10^{-7}$ m/s, using hourly thermal loads. 75
6.22 Comparison of modelled ground temperature evolution at the borehole centre and at 0.5 m distance, for a borehole depth of 61 m. 76

A.1 Regional geological map of Wavre-Chaumont-Gistoux (modified from Herbosch & Blockmans, 2012a). 83
A.2 Geological cross-section b-b' from FIGURE A.1 (modified from Herbosch & Blockmans, 2012a). 84
A.3 Geological cross-section c-c' from FIGURE A.1 (modified from Herbosch & Blockmans, 2012a). 85
A.4 Legend of the lithologies for FIGURES A.1 to A.3 (Herbosch & Blockmans, 2012a). 86
A.5 Borehole 1 - located downstream (modified from Resolia, 2023a).[1]. 87
A.6 Borehole 2 - located in the middle (modified from Resolia, 2023a).[2]. 88
A.7 Borehole 3 - located upstream (modified from Resolia, 2023a)[3]. 89
A.8 Measured flow rate: 19 L/min 90
A.9 Measured flow rate: 28.5 L/min 90
A.10 Measured flow rate: 37 L/min 90
A.11 Flow meters measuring the volumetric flow rate in the geothermal loop for each probe. . . 90
A.12 Evolution of the thermal conductivity of glycol-water fluid as a function of glycol concentration. 91
A.13 Evolution of the specific heat capacity of glycol-water fluid as a function of glycol concentration. 91
A.14 Evolution of the density of glycol-water fluid as a function of glycol concentration. 92
A.15 Evolution of the dynamic viscosity of glycol-water fluid as a function of glycol concentration. 92
A.16 Hydraulic layout of the RDI (modified from Resolia, 2023b)[4]. 93
A.17 Temperature evolution in the domestic hot water tank and at the inlet of the heat pump (HP) on the primary circuit, from 01/11/2024 to 21/11/2024. The green arrow marks the period selected for further analysis (see FIGURE 5.3). 94
A.18 Hourly evolution of heat pump inlet and outlet temperatures for the primary and secondary loops, distinguishing between domestic hot water and heating operation modes. 95
A.19 Comparison of hourly evolution of extracted ground energy using three calculation methods. 96
A.20 Modelled temperature evolution at multiple observation points located inside and outside the boreholes, and the monitored fluid temperature evolution, for a groundwater specific discharge of 0 m/s. 97

A.21 Comparison of modelled ground temperature evolution at different external observation points, using daily thermal loads and a groundwater specific discharge of $8.57 \cdot 10^{-7}$ m/s. . 98
A.22 Comparison of modelled ground temperature evolution at multiple external observation points, using hourly thermal loads and a groundwater specific discharge of $8.57 \cdot 10^{-7}$ m/s. 98
A.23 Modelled fluid temperature evolution at the centre of each borehole in the absence of groundwater flow ($u_x = 0$ m/s), using hourly thermal loads. 99
A.24 Modelled fluid temperature evolution at the centre of each borehole with a groundwater specific discharge of $u_x = 8.57 \cdot 10^{-7}$ m/s, using hourly thermal loads. 99

List of Tables

2.1 Different kinds of geothermal energy systems (Dassargues & François, 2024). 9
2.2 Example of thermal conductivity values (CSTC, 2016). 17
2.3 Parameters for the resolution of the ILS model (Philippe et al., 2009). 20
2.4 Comparison of thermal models by applicability over time scales 23

6.1 RMSE between modelled and monitored fluid temperature for different initial ground temperatures T_0. 55
6.2 RMSE between modelled and monitored ground temperature for different values of ground thermal conductivity k_m. 58
6.3 RMSE and MAE between modelled and monitored ground temperature for different values of volumetric heat capacity $\rho_b c_b$. 61
6.4 RMSE and MAE between modelled and monitored fluid temperature, and corresponding borehole thermal resistance R_b for different values of the grout thermal conductivity k_b. . . 64
6.5 RMSE and MAE between modelled and monitored fluid temperature, and corresponding borehole thermal resistance R_b for different values of the thermal conductivity of the probe k_p. 66
6.6 RMSE between the monitored fluid temperature and the average modelled fluid temperature at the centre of the three boreholes, for different values of groundwater specific discharge u_x. 68

Chapter 1

Introduction

1.1 Context

In Belgium and many other countries, heating buildings, whether tertiary or residential, represents a significant share of energy consumption. In the European Union (EU), in 2022, residential heating accounted for the main energy used by households, with a percentage of 63.5%. The percentage of energy used by households for water heating is the second highest, representing 14.9%. In contrast, space cooling accounts for only 0.6% of the total energy consumed by a household (FIGURE 1.1). Belgium is the fourth European country using the highest proportion of energy for household heating. In the EU in 2022, the share of fuels in the final energy consumption of the residential sector for space heating was mainly natural gas (36.3%), renewables and biofuels (31.4%), and oil and petroleum products (13.1%) (Eurostat, 2023) (FIGURE 1.2). Consequently, greenhouse gas emissions are important. In Belgium, in 2023, residential and tertiary heating accounted for 17.6% of emissions ("Émissions par secteur", n.d.) (FIGURE 1.3). The challenge of decarbonizing this sector is therefore crucial. In addition to the climatic and environmental aspects, the geopolitical context is also a factor. Indeed, the current war situations have shown European countries such as Belgium that relying on a country like Russia for energy production is not viable in terms of resource availability, economics, or social stability.

It has therefore become essential to adapt energy sources for heating buildings, heating domestic water and cooling buildings. A solution exists and is found everywhere beneath our feet, geothermal energy! Through the use of underground probes (closed-loop systems) or doublet pumping wells (open-loop systems), coupled with a heat pump, geothermal energy can be extracted. This process provides an inexhaustible and environmentally friendly source of thermal and electrical energy on a human timescale. Even though geothermal energy depends on soil temperature, which varies with location on Earth, this energy has the potential to become a major energy source in the future because it is available everywhere and withdrawals are continuously replenished (Stober & Bucher, 2021). The uptake of efficient heating and cooling technologies such as geothermal heat pumps could lead to a mitigation of potential global warming and help achieve environmental impact targets (Naicker & Rees, 2019). Geothermal energy requires minimal surface space, and is available 24 hours a day, 365 days a year.

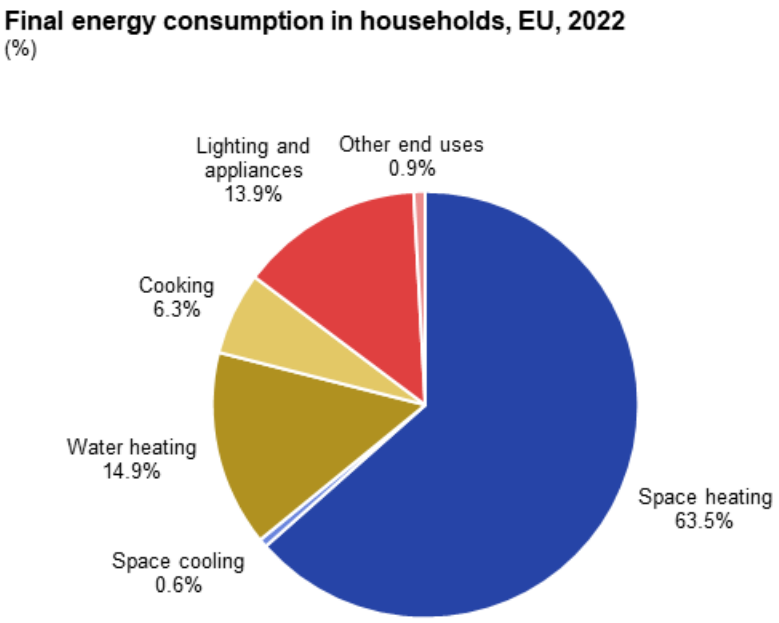

FIGURE 1.1: Final energy consumption in households, EU, 2022 (%) (Eurostat, 2023).

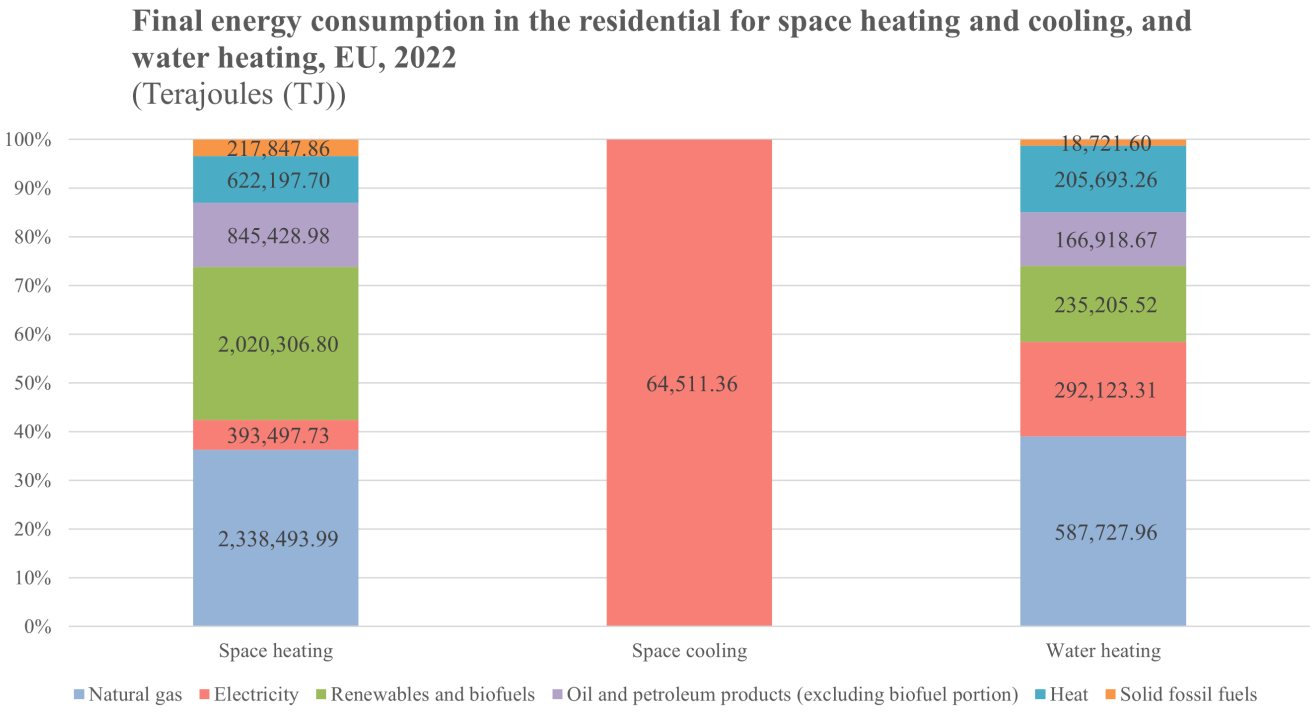

FIGURE 1.2: Final energy consumption in the residential sector by use, EU, 2022 (Terajoules (TJ)) (modified from Eurostat, 2023).

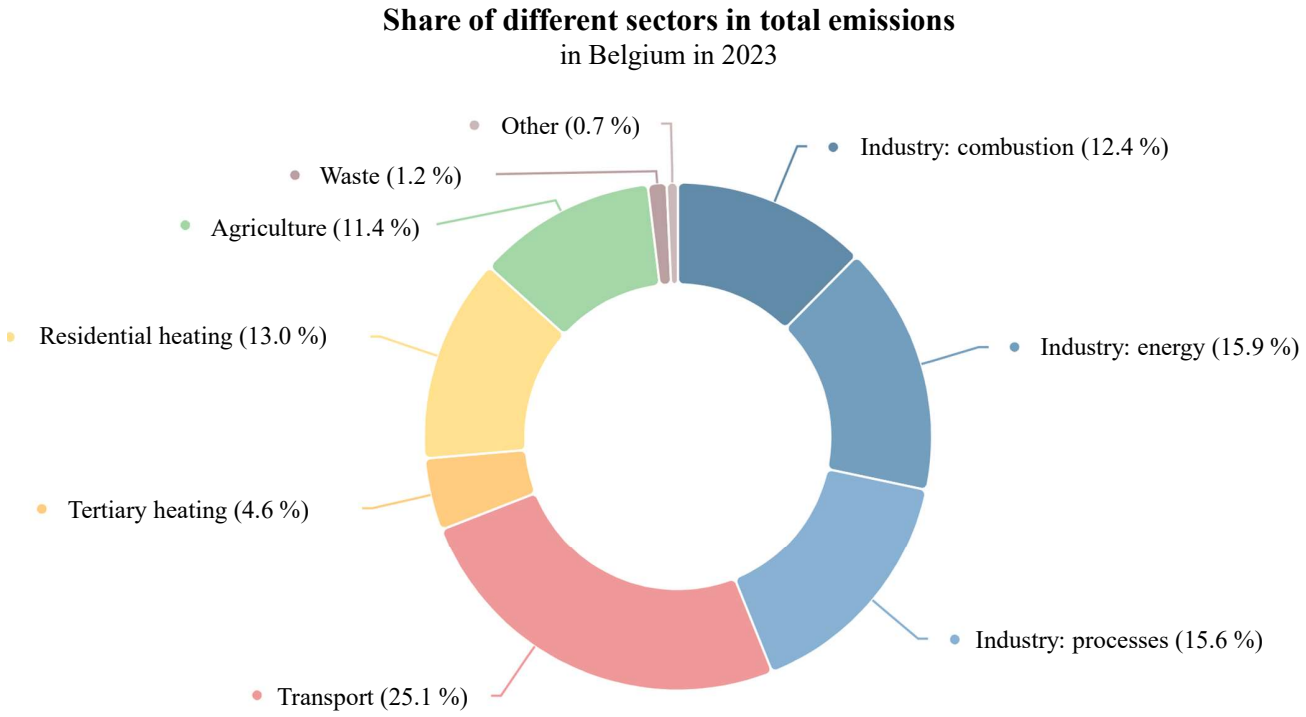

FIGURE 1.3: Share of different sectors in total emissions in Belgium in 2023 (modified from "Émissions par secteur", n.d.).

1.2 Objectives and content of the work

The "Relais des Ingénieurs" (RDI) residence in Louvain-la-Neuve is a building equipped with three geothermal boreholes coupled to a heat pump. Monitoring data from this heat pump have been collected over a period of more than one year. In this work, datasets are analysed to extract relevant information required for model calibration. The analytical heat transfer model developed by Erol et al. (2015) is then calibrated to reproduce the evolution of the underground temperature, with the goal of matching the simulated results as closely as possible to the monitored values. The objective is to adjust and optimise the model parameters so that the simulated temperature evolution within the borehole heat exchangers closely corresponds to the monitoring data. This calibration process enables more accurate predictions of subsurface temperature conditions, improving the design and sizing of geothermal systems based on the energy demand of the building. Moreover, the parameter calibration also makes it possible to predict the future evolution of the ground heat reservoir under different building energy demand scenarios. Finally, better sizing of geothermal systems through model calibration can contribute to increasing the number of installations of these technologies, thereby promoting the transition to low-carbon heating solutions and contributing to the reduction of greenhouse gas emissions.

To achieve these objectives, the work is structured into several CHAPTERS. It begins with a literature review covering the principles of geothermal energy, heat pumps, borehole heat exchangers, the heat transfer equation, and analytical thermal models. This theoretical background is necessary to define the concepts used throughout the study. The following CHAPTER presents the general context of the Relais des Ingénieurs site. Particular attention is given to the geological and hydrogeological settings, as they

determine the thermal properties of the ground. CHAPTER 4 introduces the analytical model developed by Erol et al. (2015), and presents the initial values assigned to its input parameters based on the characteristics of the site and literature. The practical part of the study begins with the analysis of the monitoring datasets, used to estimate the thermal load extracted from the ground. This is followed by CHAPTER 6, which presents the core results of the thesis. It describes the step-by-step calibration of model parameters, including the initial ground temperature, thermal conductivity of the ground, grout, and probe, volumetric heat capacity, and specific discharge. Both daily and hourly thermal loads are used for comparison. The performance of the model is assessed using error metrics such as Root Mean Square Error (RMSE) and Mean Absolute Error (MAE). The work concludes by summarising the findings and proposing perspectives for future research.

Chapter 2

State of the art

2.1 Geothermal energy

2.1.1 Origin and history

Geothermal energy is underground heat, i.e., the thermal energy stored in the Earth's body. At the core-mantle boundary, the temperature reaches around 3000 °C, while at the Earth's surface, the average temperature is about 14 °C due to climatic influences. The driving force of heat flow is the temperature difference between the Earth's surface and interior, which continually attempts to eliminate ΔT. The geothermal gradient, which is the rate of temperature increase with depth, has an average value of 3 °C per 100 meters in the near-surface region in Central Europe. Internal heat is not only due to the remaining heat from the primordial energy of planetary accretion. In fact, this heat originates from different sources: about 70% is generated by the decay of radioactive elements in the crust, specifically ^{238}U,^{235} U,^{232} Th,^{40} K in the continental crust (Stober & Bucher, 2021). FIGURE 2.1 illustrates the temperature evolution with depth using a 3 °C/100 m gradient over the first few hundred metres in the lithosphere. At 0 meters depth, the temperature corresponds to the average external temperature.

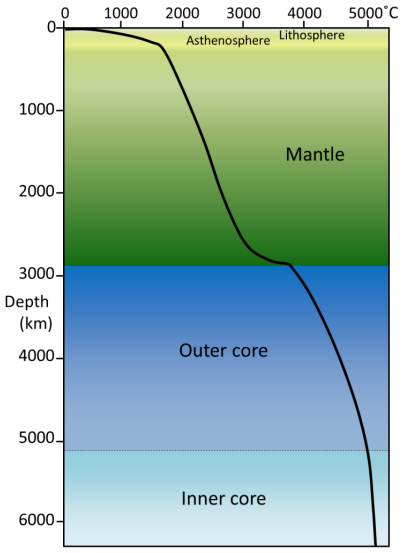

FIGURE 2.1: Generalized rate of temperature increase with depth within Earth (Earle, 2015).

The use of geothermal energy is not recent. In fact, it has been used by humanity since its existence.

Hot springs and hot pools, which are surface manifestations of geothermal energy, have long been used for bathing and health treatments, but also for heating and cooking. Archaeological finds show that geothermal springs were used by North American Indigenous people several thousand years ago. Civilizations such as the Romans, Japanese, Turks, Icelanders, and Maori from New Zealand have documented the occurrence and use of hot springs for cooking, bathing, and heating homes (Stober & Bucher, 2021).

FIGURE 2.2: Ruins of the Roman bathing facility at the thermal springs of Badenweiler in the Rhine rift valley (southern Germany) (Stober & Bucher, 2021).

More recently, the first documented work reporting temperature measurements taken with a thermometer as a function of depth (the notion of geothermal gradient) dates back to 1740, based on observations made in a mine in France. However, it was only from the second half of the 19th century and the rapid development of thermodynamics that the use of hot water for energy conversion began. Thermodynamics played a fundamental role in making energy conversion from hot steam to mechanical energy and then into electrical energy with the help of turbines and generators (Stober & Bucher, 2021). It was in northern Italy, in the Larderello region, that in 1827 the first plant for geothermal energy conversion was installed. A low-pressure steam boiler, naturally heated with geothermal water, was used for boron recovery and other substances dissolved in the thermal water. The geothermal steam was later used in reciprocating and centrifugal pumps and winches. It was also in Larderello, in 1904, that the first generation of electricity from geothermal steam occurred. This first experiment's success demonstrates the industrial value of geothermal energy (Dickson & Fanelli, 2013). Today, thanks to research advancements and technological progress, Iceland, for example, supplies 53% of its primary energy from geothermal sources (Stober & Bucher, 2021).

2.1.2 Advantages

As previously mentioned, geothermal energy is described as renewable and sustainable. It is renewable because a very large amount of heat is stored in the body of the planet, and human consumption cannot deplete this reservoir. However, if the rate of heat extraction exceeds the natural recharge rate, ground temperatures may decline, leading to a decrease in system performance over time. Additionally, in some locations, particularly due to the type of rock, the subsurface heat recharge rate is lower. For these reasons, proper planning is essential when implementing geothermal systems to ensure their long-term efficiency

and sustainability.

SECTION 1.1 highlighted the need to decarbonize energy production sources. Geothermal energy has a major role to play in this mission, as it does not directly produce CO_2. In fact, the heat pumps used to extract this energy do not emit greenhouse gases. However, they consume electricity. Therefore, the environmental impact varies depending on the country where the system is located, as it depends on how the electricity is generated there. Nevertheless, geothermal energy remains a more ecological solution than using energy produced from traditional fossil resources such as coal, oil, or gas.

In addition to being advantageous over fossil fuels, geothermal energy also presents benefits over other renewable energy sources such as solar or wind power. One of its main advantages is reliability. Reliability is explained by the ability of the energy source to be used consistently. Intermittent renewable resources, such as solar and wind power, produce electricity that is irregular and dependent on weather conditions, whereas geothermal energy can be used consistently over long periods without depending on the weather (Kulasekara & Seynulabdeen, 2019).

The annual variation in ground temperature at a depth of more than a few metres is much less than the annual variation in air temperature. This ground temperature stability enables geothermal systems to have a dual function, one during winter and the other one during summer. In summer, when the ground temperature is lower than the air temperature, the ground can potentially be used as a heat sink. Conversely, in winter, when the ground temperature is higher than the air temperature, it can be used as a heat source (FIGURE 2.3) (Preene & Powrie, 2009).

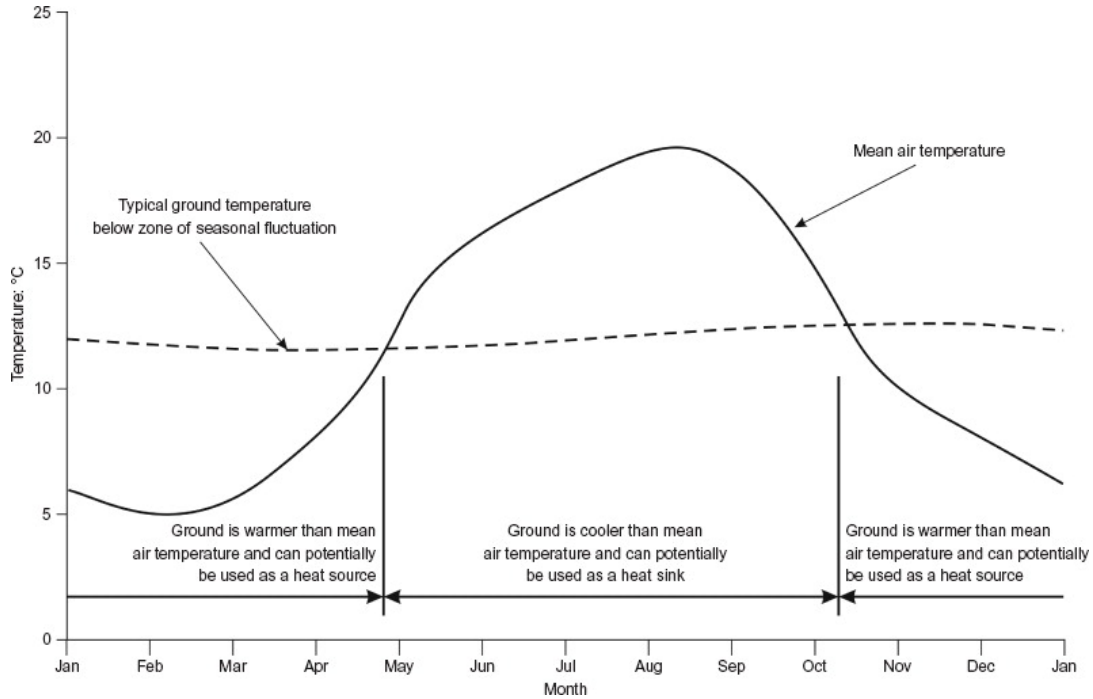

FIGURE 2.3: Relationship between surface air temperature and ground temperature (Preene & Powrie, 2009).

2.2 Geothermal systems

2.2.1 General principles

Geothermal systems use the ground and groundwater beneath a site as a heat source or sink to reduce energy costs and improve the environmental performance of buildings. There are different types of geothermal systems. They depend on a number of parameters and differ in terms of depth, the working principle (open or closed loops), the application (heating, cooling, heat storage, electricity production), the extracted power, and the cost. Generally speaking, a geothermal system is made up of three main elements: a heat source, a reservoir, and a fluid, which is the carrier that transfers the heat (Dickson & Fanelli, 2013). It is very important that these geothermal systems are correctly dimensioned so that the expected results are maintained over time.

A classification based on depth can be made to differentiate the different types of geothermal energy. Three main categories can be distinguished:

1. Category I: 1 - 5 metres deep
2. Category II: maximum 300 metres of depth
3. Category III: minimum 1000 meters of depth

Shallow geothermal energy (depths of less than 300 m) generally involves the use of heat pumps. This is because the heat in the ground generally corresponds to the average annual outside temperature, and a heat pump is needed to supply the building with the energy required for heating. These systems are usually called Ground (Source) Heat Pump systems (GSHP or GHP). Deep geothermal energy (depths greater than 300 m) refers to projects where the heat is used directly (Dassargues, 2019).

Very low-energy geothermal energy (temperature < 30°C), which is therefore generally at shallow depths, is one of the most economical, ecological, and sustainable techniques for satisfying the energy needs of a building for both heating and cooling ("Géothermie - Géolys", 2024). The TABLE 2.1 lists the different characteristics of geothermal energy systems for the categories listed above. The TABLE 2.1 indicates that the categories I and II operate at very low energy in open or closed systems. The category III operates at a higher energy because the depth is more important, as well as the temperature.

TABLE 2.1: Different kinds of geothermal energy systems (Dassargues & François, 2024).

Category	**Depth**	**Temperature**	**Enthalpy**	**Types**	**Soil/Rock**	**Water present**	**Uses**
Category I	1 - 5 metres	-10 - 25 °C	Very low energy	Horizontal loop fields and heat baskets	Soft soil	Water not recommended	Climate control (heating and/or cooling) of buildings - domestic hot water
Category II Closed systems	10 - 30 metres	0 - 25 °C	Very low energy	Energy piles and other geostructures	Soft soil	Water not essential	Climate control (heating and/or cooling) of buildings - domestic hot water
Category II Closed systems	50 - 300 metres	0 - 25 °C	Very low energy	Vertical loop fields	Soft or porous soil	Water not essential	Climate control (heating and/or cooling) of buildings - domestic hot water
Category II Open systems	10 - 100 metres	0 - 25 °C	Very low energy	Geothermal wells (pumping wells)	Saturated permeable subsoil (aquifer)	Aquifer	Climate control (heating and/or cooling) of buildings - domestic hot water
Category III	1,000 - 2,000 metres	50 - 100 °C	Low energy	Geothermal wells (pumping wells)	Porous or fractured rock	Hot water	High-temperature heating
Category III	4,000 - 5,000 metres	100 - 200 °C	Intermediate energy	Geothermal wells (pumping wells)	Fractured rock	Hot water or steam	Industrial applications or energy production
Category III	1,500 - 3,000 metres	>200 °C	High energy	Pumping wells / steam wells	Fractured rock	Steam	Energy production

2.2.2 Near-surface geothermal systems

In near-surface geothermal systems, the temperature generally does not exceed 25°C and the depth 300 m, although in general this depth is rarely greater than 150 m. Two systems can be distinguished between open and closed systems.

Open-loop systems

Open-loop systems require the presence of a shallow aquifer because they pump groundwater from the ground to the surface (Ground Water Heat Pumps, GWHPs) by one or more pumping and reinjection well doublets. The first well is used to extract the groundwater from the aquifer (production well). The groundwater is then passed through a heat transfer system (generally a heat pump). After that, the second well is used to discharge water back to the aquifer at a lower temperature than before (injection well) (FIGURE 2.4). To avoid mixing water of different geochemical compositions, which can cause environmental and operational difficulties, the wells should be located in the same aquifer. In rarer cases, a reinjection well may not be necessary, groundwater can be wasted and therefore does not return to the aquifer but is discharged into a surface water body, as long as it is permitted by its water characteristics and the environmental regulations. More and more doublet wells have dual functionality (production and injection well). This dual function allows the building to be heated in winter and cooled in summer by reversing the direction of water flow in the wells. In summer, heat is extracted from the building and reinjected into the ground. This type of system is called Aquifer Thermal Energy Storage (ATES) (FIGURE 2.5) (Figueira et al., 2024).

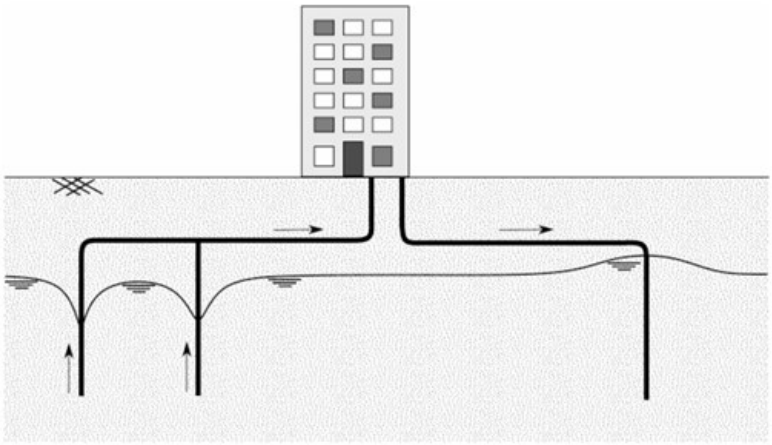

FIGURE 2.4: Open-loop geothermal system with a well-doublet (Dassargues, 2019).

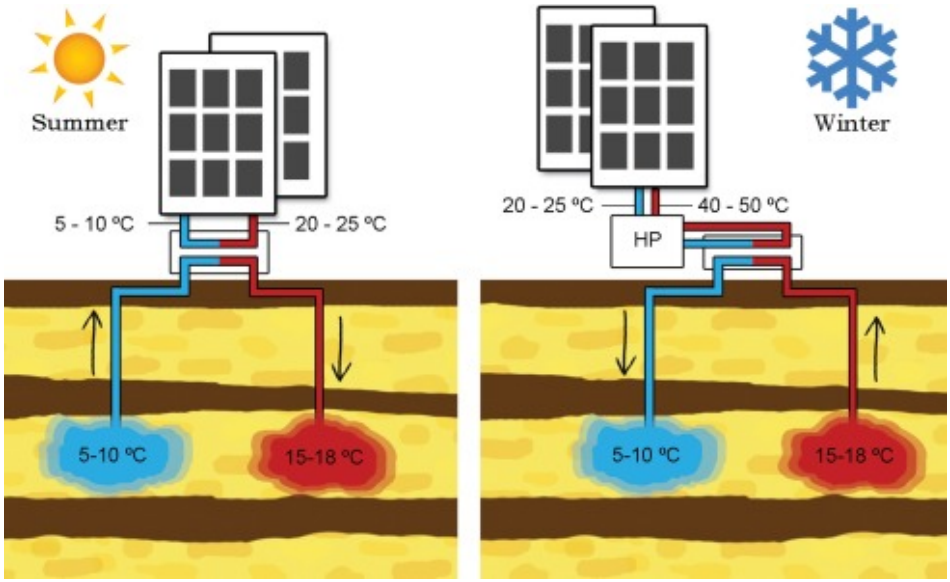

FIGURE 2.5: Illustration of the basic working principle of a low-temperature seasonal ATES system (Bloemendal & Hartog, 2018).

Closed-loop systems

Closed-loop system exchanges thermal energy with the ground only, unlike the open-loop system, it does not require the presence of an aquifer. In closed-loop systems, a heat transfer fluid circulates through a Ground Heat Exchanger (GHE) to extract/release heat from/to the ground. These systems are generally referred to as Ground-Coupled Heat Exchangers (GCHEs), or more specifically as Ground-Coupled Heat Pumps (GCHPs) when a heat pump is integrated. The flowing fluid can be water, anti-freezing liquid, refrigerant, or mixture (Mahmoud et al., 2023). There are two main categories of close-loop systems: horizontal systems and vertical systems.

1. **Horizontal closed-loop systems:**
   Horizontal closed-loop systems are more suitable for lower power demands, such as individual houses. These systems are placed at a shallow depth, generally 1-2 m. They still need to be installed below the maximum penetration depth of winter frost, but the system needs to be above the level of solar regeneration in the summer. The surface area required for installation can be quite large, as a length of 35 to 60 m of exchanger pipe per kW is required. Most of the time these systems are made of loops of pipes and come in series, parallel, basket, or slinky types (Dassargues, 2019; Stober & Bucher, 2021) (FIGURE 2.6).

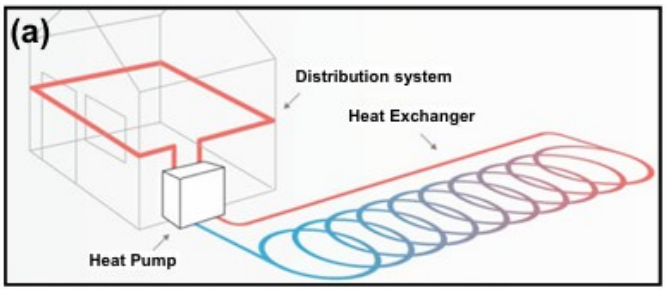

(a) Slinky-type

(b) Basket-type

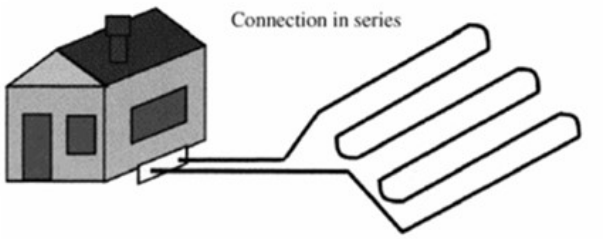

(c) Connections in series

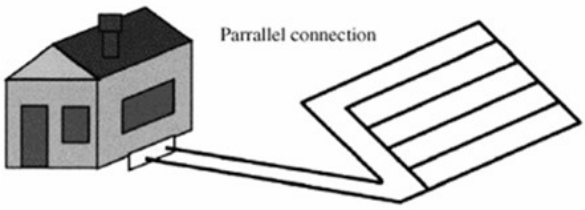

(d) Parallel connection

FIGURE 2.6: Horizontal closed-loop systems (Mahmoud et al., 2023; Stober & Bucher, 2021).

2. **Vertical closed-loop systems:**
Vertical closed-loop systems, as they mostly benefit from a constant annual ground temperature, are more efficient and more common. These closed-loop systems can be found in various structures such as concrete piles, foundation slabs, retaining walls, and tunnel structures or be a geothermal probe in a borehole, more commonly known as Borehole Heat Exchangers (BHEs). These systems involve making a borehole into which a geothermal probe is inserted. This probe can be single U-tube, double U-tube (most often) and coaxial. The annular space (between the ground and the tubing) is filled with a grouting material which must be thermally conductive and impermeable (FIGURE 2.7). Although this grouting material is not always necessary, as in the case of boreholes entirely drilled in highly permeable gravel, it is nonetheless of interest because it prevents contamination in the event of a leak of the circulating fluid. These systems, widely used for heating and cooling individual and collective buildings, produce between 20 W/m and 80 W/m (in temperate climate conditions). For optimum performance, rigorous studies must be carried out to ensure that the probe field is adequately dimensioned and configured. Unlike open-loop geothermal systems, closed-loop systems do not require specific hydraulic conductivity conditions. As a result, they are often considered suitable for a wide range of sites, and the importance of characterising the underground, particularly its thermal conductivity, is sometimes neglected. This lack of attention to site-specific thermal properties can lead to a strong mid-term decrease in the system efficiency and also to possible significant environmental impacts. As with open systems, geothermal probes can also be used to provide cooling in summer, either by reversing the operation of the heat pump or through passive cooling using the ground as a heat sink. The heat injected into the ground during summer can be reused during winter, a process known as Borehole Thermal Energy Storage (BTES). Ground heating can also be carried

out in combination with solar-thermal installations, which store excess heat during the warm season to meet demand during the cold season (Dassargues, 2019; Stober & Bucher, 2021).

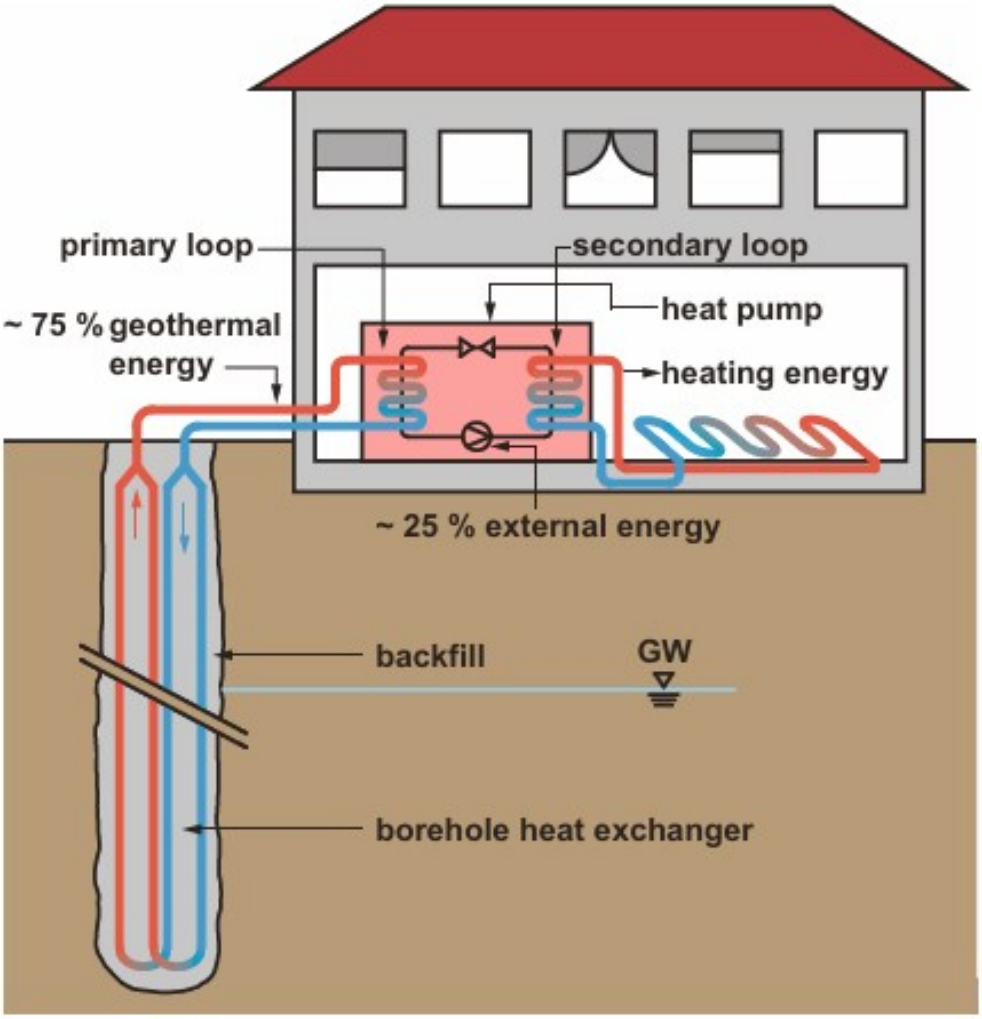

FIGURE 2.7: General design of a borehole heat exchanger system (Stober & Bucher, 2021).

Geothermal probes:
As previously discussed, geothermal probes are liquid-filled tubes (single, double U and coaxial, FIGURE 2.8) installed in a borehole. Single U-tube probes are closed, seamlessly drawn plastic tubes with a U-shaped foot. Double-U probes are simply two independent single-U tubes installed in the same borehole. A cold heat-transfer fluid circulates in the tube and picks up heat from the ground on its way down. The heated fluid moves up the tube after passing through the U-shaped foot until it reaches the heat pump. The heat pump uses the extracted ground heat to increase the fluid temperature of a secondary cycle. This second cycle is generally used to heat buildings or domestic hot water. The thermal properties of the ground and the system design mainly determine the length of the probe. The thermal properties of the probe, of the grouting material (backfill) and of the heat transfer fluid are also important. Unfortunately, most probes are made of polyethylene, which is a poor heat conductor with a low thermal conductivity (about $0.4\ W/(mK)$). To increase the efficiency of probes, by reducing the pump's power requirements, a low dynamic viscosity and

low density is needed (Stober & Bucher, 2021).

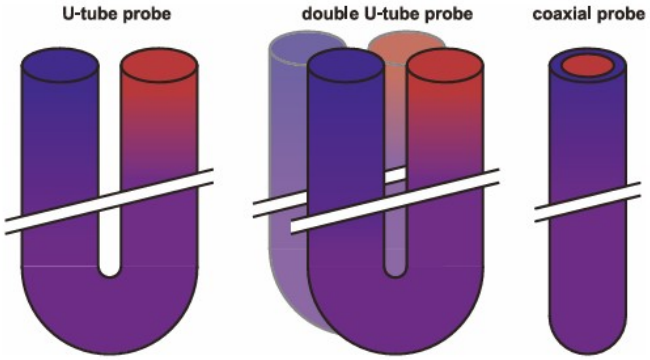

FIGURE 2.8: Schematic illustration of types of probe tube design (Stober & Bucher, 2021).

2.3 Heat pumps

2.3.1 General principles

Geothermal heat pumps can provide both an economically and environmentally beneficial solution for space heating and can also be used for space cooling. The mechanical work of a compressor (typically powered by electricity) enables the transfer of heat from a relatively low temperature source to a higher temperature sink. In other words, the heat pump facilitates heat exchange between the primary circuit (in the ground) and the secondary circuit (in the building). If the heat pump is reversible, it can also operate in cooling mode. In that case, the primary circuit serves as the heat sink and the secondary circuit as the heat source. The advantage of heat pumps is that they transport more thermal energy than the amount of energy required for their operation. Basic heat pumps function using the vapour-compression refrigeration cycle. The working fluid used is generally a refrigerant. The five major components of a heat pump include: a compressor, an expansion valve, a reversing valve (if a cooling mode is available), and two heat exchangers (an evaporator and a condenser) (FIGURE 2.9). The thermodynamic cycle of a heat pump operating in heating mode is as follows:

1. A liquid-dominated fluid, in a mixed liquid/vapour state, enters in the evaporator. Heat is transferred from the ground loop to the refrigerant, causing it to slightly increase in temperature and evaporate into a low-pressure vapour.

2. The vapour enters in the compressor, where the pressure is significantly increased. This compression results in a high-temperature and high-pressure vapour.

3. The hot vapour then flows into the condenser. Since its temperature is higher than that of the secondary circuit, heat is transferred from the refrigerant to the building's system.

4. The refrigerant then passes through an expansion valve, which reduces its pressure and consequently lowers its temperature. The cycle then restarts as the refrigerant re-enters the evaporator.

If the system includes a cooling mode, the reversing valve is used to redirect the flow of the fluid in the opposite direction within the cycle. In this case, the condenser becomes the evaporator, and vice versa. In some systems, an auxiliary component such as a desuperheater is also included. This additional heat

exchanger supplies heat to a domestic hot water tank. It transfers the heat from the compressed steam leaving the compressor to the water circulating in the tank, reducing the energy needed to heat the water. The layout shown in FIGURE 2.9 is a basic representation. In practice, many complexities can be added to the system depending on the specific installation and application context. (Dassargues & François, 2024; Self et al., 2013; Stober & Bucher, 2021).

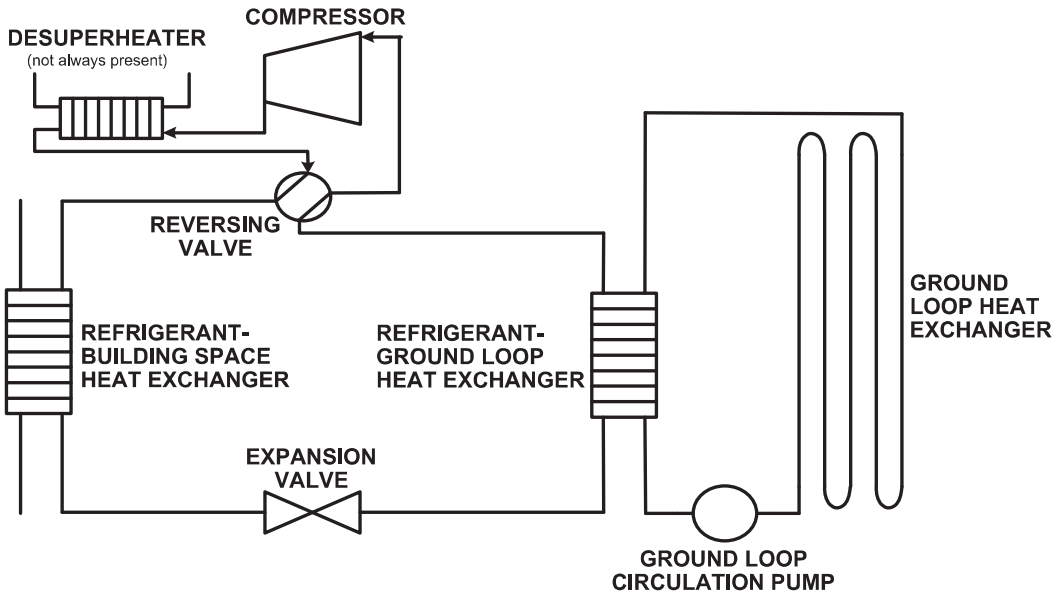

FIGURE 2.9: Basic layout of geothermal heat pump system (Self et al., 2013).

2.3.2 Performance coefficients

The performance of heat pumps is quantified by the Coefficient Of Performance (COP). This value can be estimated theoretically using the Carnot COP, which represents the maximum efficiency achievable by a heat pump operating according to the ideal reversed Carnot cycle. This ideal cycle operates between two thermal reservoirs, one cold and one hot, at temperatures T_L and T_H respectively. In this case, T_L represents the ground temperature (source side), which is colder than T_H, the condenser inlet temperature (sink side). The theoretical efficiency is given by:

$$COP_{Carnot} = \frac{T_H}{T_H - T_L} \tag{2.1}$$

However, in practice, the real COP of a heat pump is a fraction of the ideal COP due to thermal losses and technical imperfections. It can be expressed as:

$$COP = \eta \cdot COP_{Carnot} \tag{2.2}$$

where COP is the real performance coefficient of the heat pump, and η is the efficiency factor of the system (also known as the Carnot efficiency) (Dewallef, 2024; Lemort, 2023). The real COP can be interpreted in two ways: instantaneous and seasonal.

Instantaneous

The instantaneous COP is defined as the ratio between the thermal capacity delivered at the condenser and the electrical power consumed by the compressor plus auxiliary components (kW) (EQUATION 2.3). Since the thermal output at the condenser is greater than the electrical input, the ratio is greater than 100%. This is one of the reasons why the notion of COP was introduced. It is therefore important that heat pumps operate as efficiently as possible, as this directly affects the COP. The COP value increases when the temperature difference between the two circuits (source and sink) decreases. This value is independent of the energy consumed by the circulation pumps of the primary and secondary loops. Due to the relatively stable ground temperature all along the year, the ground source heat pumps may reach high COP values (COP > 5). As an example, for a COP of 4, 75% of the delivered heat is considered free from both an environmental (renewable) and financial (no cost) perspective. Only 25% of the total energy input (typically electricity) must be paid for (FIGURE 2.10) (Dassargues & François, 2024; Stober & Bucher, 2021).

$$COP = \frac{\text{Power output after heat pump } [kW]}{\text{Power input for operation } [kW]} \tag{2.3}$$

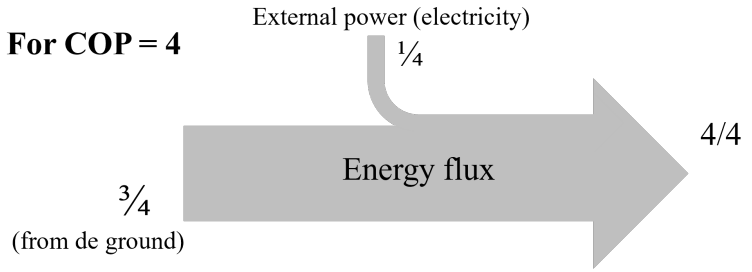

FIGURE 2.10: Contribution of the ground and external power for a COP of 4 (modified from Dassargues and François, 2024).

Seasonal

The Seasonal Performance Factor (SPF) is also an efficiency indicator. This factor is considered more significant and relevant for characterizing the performance of the system. This no longer expresses a power ratio but an energy ratio between the thermal energy released by the condenser and the energy supplied to the system to power the compressor (kWh). The efficiency of the heat pump is thus assessed over a longer time period. Unlike the COP, it does not depend only on the operating conditions but also on the habits of the user, the climatic situation, and other factors (Stober & Bucher, 2021).

2.4 Heat transfer processes

The heat transport equation in the subsurface involves 3 processes: heat conduction, convection/advection, and thermal dispersion. These 3 heat transport modes do not have the same influence on thermal distribution. The transport mechanisms and particularities of these processes will be described.

2.4.1 Heat conduction

Thermal conduction is a heat flux resulting from a thermal gradient. Heat flows naturally from regions of higher temperature to regions of lower temperature in any medium, whether it is porous and saturated, partially saturated, or completely dry. This heat conduction does not require the presence of fluid flow. The conduction flux of heat transfer is described by Fourier's linear law. It is expressed in watts per square meter $[W/m^2]$ and has the expression:

$$\mathbf{Q}_{T,\text{conduction}} = -\lambda_b \, \mathbf{grad}(T) = -\lambda_b \nabla T \tag{2.4}$$

where λ_b is the heat or thermal conductivity of the ground $[W/(mK)]$, and ∇T is the temperature gradient $[K/m]$. A proposed expression for thermal conductivity is as follows:

$$\lambda_b = \lambda_s(1-n) + \lambda_w n S_r + \lambda_g n(1-S_r) \tag{2.5}$$

with λ_s, λ_w, and λ_g being the thermal conductivities of solid particles, water, and air, respectively. EQUATION 2.5 expresses the thermal conductivity as a function of the proportion occupied by each constituent, by the presence of n the porosity and S_r the degree of saturation. It is a proposal, as different expressions exist depending on the assumptions made. In addition to depending on the porosity and the degree of saturation, λ_b depends on the lithology (mineralogy of the soil particles), the temperature, the pressure, and the properties of the fluids and the gases filling the pores and the fissures. However, for shallow heat transfer, the temperature and pressure dependences are often neglected. TABLE 2.2 presents typical values of thermal conductivity. Thermal conductivity is one of the most important parameters in geothermal systems. It represents the ability of a material to transport thermal energy (Dassargues, 2019; Dassargues & François, 2024).

TABLE 2.2: Example of thermal conductivity values (CSTC, 2016).

Lithology	**Thermal conductivity λ_b [W/(mK)]**	
	Effective value	**Recommended value**
Clay/silt, dry	0.40 – 1.00	0.50
Clay/silt, water-saturated	1.10 – 3.10	1.80
Sand, dry	0.30 – 0.90	0.40
Sand, wet	1.00 – 1.90	1.40
Sand, water-saturated	2.00 – 3.00	2.40
Sandstone	1.90 – 4.60	2.80
Schists	1.50 – 3.10	2.20
Limestone	2.00 – 3.90	2.70
Dolomite	3.00 – 5.00	3.50
Granite	2.10 – 4.10	3.20
Quartzite	5.00 – 6.00	5.50
Bentonite	0.50 – 0.80	0.60
Air	0.02	/
Water	0.59	/

2.4.2 Heat advection and convection

Heat can also be transported through the subsurface via groundwater flow. This is known as heat advection. This groundwater flow can result from a hydraulic head gradient (advection/forced convection) or from temperature-induced density differences (free or natural convection). The expression for the advective heat flux is given in EQUATION 2.6, with units in $[W/m^2]$:

$$\mathbf{Q}_{T,\text{advection}} = \rho_w c_w \, \mathbf{q} \, (T - T_{\text{ref}}) \tag{2.6}$$

with ρ_w the density of water $[kg/m^3]$, c_w the specific heat capacity of water $[J/(kgK)]$, and $\rho_w c_w$ the volumetric heat capacity of water $[J/(m^3K)]$. The vector $\mathbf{q}$ is the total water flux $[m/s]$ from Darcy's law: $\mathbf{q} = -\mathbf{k_w}\nabla(h_w)$, where $\mathbf{k_w}$ is the soil permeability $[m/s]$, and $\nabla(h_w)$ the hydraulic potential gradient $[-]$. T is the applied temperature $[K]$, and T_{ref} is the reference temperature $[K]$ (Dassargues, 2019; Dassargues & François, 2024).

2.4.3 Thermal dispersion

Thermal dispersion represents the heat transfer through pores and/or fissures of the medium, and through heterogeneities in the solid matrix. EQUATION 2.7 gives the expression for thermal dispersion heat flux (in $[W/m^2]$):

$$\mathbf{Q}_{T,\text{dispersion}} = -\rho_w c_w \, \mathbf{D} \cdot \nabla T \tag{2.7}$$

with ρ_w, c_w and ∇T as previously defined. The tensor $\mathbf{D}$ represents thermal dispersion and depends on the Darcy flux $\mathbf{q}$ and on the thermal dispersivity coefficients (longitudinal and transverse) (Constantz, 2008; Dassargues, 2019; Erol et al., 2015; Hopmans et al., 2002).

2.4.4 Heat conservation equation in saturated porous media

The heat conservation equation in saturated porous media can be written as:

$$\frac{\partial \rho_b c_b T}{\partial t} = -\nabla \cdot [\rho_w c_w \mathbf{q} T - (\lambda_b + \rho_w c_w \mathbf{D}) \nabla T] + Q_T \tag{2.8}$$

where Q_T is a heat source (if $Q_T > 0$) or a heat sink (if $Q_T < 0$). All terms in the EQUATION 2.8 are expressed in units of $[W/m^3]$. In most cases, the thermal dispersion term can be neglected compared to the thermal conduction term. The equation is written:

$$\frac{\partial \rho_b c_b T}{\partial t} = -\nabla \cdot [\rho_w c_w \mathbf{q} T - \lambda_b \nabla T] + Q_T \tag{2.9}$$

Dividing the equation by $\rho_b c_b$, with ρ_b the bulk density of the porous medium $[kg/m^3]$, c_b the bulk heat capacity $[J/(kgK)]$, and $\rho_b c_b$ the bulk volumetric heat capacity $[J/(m^3K)]$, it becomes:

$$\frac{\partial T}{\partial t} = -\nabla \cdot \left[\frac{\rho_w c_w}{\rho_b c_b} \mathbf{q} T - \frac{\lambda_b}{\rho_b c_b} \nabla T \right] + \frac{Q_T}{\rho_b c_b} \tag{2.10}$$

In this final form, EQUATION 2.10, the term $\frac{\lambda_b}{\rho_b c_b}$, commonly denoted by α, is known as *thermal diffusivity*, typically ranging from 10^{-7} to 10^{-6} $[m^2/s]$. The bulk volumetric heat capacity is also an important parameter in hydrothermal systems, as it represents the ability of the ground to store thermal energy (Dassargues, 2019).

.

2.5 Temperature modelling

It is difficult to model the temperature field precisely, as the temperature distribution inside and near the borehole is not symmetrical. In addition, it depends on the time and space scales chosen. As previously discussed, long-term use of BHEs can lead to numerous technical and environmental consequences, such as modification of soil temperature and influence on groundwater quality. It is therefore necessary to optimise BHEs whether they are individual or in field. Numerical and analytical models can be used to characterise and evaluate BHE-ground interactions. Generally, analytical or semi-analytical models are preferred because they are simpler and quicker. Although they were developed later, numerical models are increasingly used. They allow greater flexibility in the distribution of thermal properties in the soil, the modelling of an advection flow around the BHE, varied geometries and a short-term description of temperature variations (Cerfontaine et al., 2016).

The study by Philippe et al. (2009) compares the applicability of three analytical solutions depending on the simulation duration. These solutions are the Infinite Line Source (ILS), the Finite Line Source (FLS), and the Infinite Cylindrical Source (ICS). These models are used to determine the transient heat transfer near boreholes, which is important for sizing BHEs and determining the resulting fluid temperature.

In this study, only the heat transfer in the ground surrounding the borehole is investigated, heat transfer inside the borehole is not examined. A constant heat transfer rate per unit length at the borehole radius is assumed and corresponds to *q'*. It is assumed that heat is only transferred by conduction, advection is considered negligible, as well as the impact of geothermal heat flux. These models are based on an axially symmetric geometry around a single borehole (Philippe et al., 2009).

2.5.1 Infinite line source model

In this case, the model assumes that the heat transfer rate per unit length is applied to a BHE which is imaged by an infinite line. Heat transfer is assumed to occur in the radial direction (Philippe et al., 2009).

The results obtained in SECTION 2.4, and neglecting thermal diffusion, give the following equation:

$$\frac{\partial T}{\partial t} = \frac{-\nabla \cdot (\mathbf{Q}_{T,\text{conduction}} + \mathbf{Q}_{T,\text{advection}})}{\rho_b c_b} \tag{2.11}$$

Since advection is neglected in the resolution of this model and the expression for the conductive heat flux ($\mathbf{Q}_{T,\text{conduction}}$) is given by EQUATION 2.4. In cylindrical coordinates, EQUATION 2.11 becomes:

$$\frac{\partial \Delta T}{\partial t} = \alpha \left(\frac{\partial^2 \Delta T}{\partial r^2} + \frac{1}{r} \frac{\partial \Delta T}{\partial r} \right) \tag{2.12}$$

The heat transfer problem to be solved corresponds to the system of the following three equations:

$$\frac{\partial \Delta T}{\partial t} = \alpha \left(\frac{\partial^2 \Delta T}{\partial r^2} + \frac{1}{r} \frac{\partial \Delta T}{\partial r} \right) \tag{2.13}$$

$$\Delta T = T - T_0 \tag{2.14}$$

$$\alpha = \frac{\lambda_b}{\rho_b c_b} \tag{2.15}$$

With the initial conditions:

$$\Delta T(r, 0) = 0 \tag{2.16}$$

$$\Delta T(r \to \infty, t) = 0 \tag{2.17}$$

$$-\lambda_b \frac{\partial \Delta T}{\partial r} 2\pi r \bigg|_{r \to 0} = q' \tag{2.18}$$

A graphical illustration of the solution is shown in FIGURE 2.11, where the temperature is evaluated at different distances from the borehole. It represents the radial temperature profile over different time periods, based on the parameters listed in TABLE 2.3. Although it is mathematically valid, the temperature tends towards infinity for small radii (centre of the borehole), which is physically not possible (Philippe et al., 2009).

TABLE 2.3: Parameters for the resolution of the ILS model (Philippe et al., 2009).

Parameters	**Values**
BHE depth, H	100 m
Heat transfer rate per unit length , q'	50 W/m
Borehole radius, r_b	0.05 m
Initial ground temperature, T_0	8 °C
Thermal diffusivity, α	$0.53 \cdot 10^{-6}$ m^2/s
Thermal conductivity, λ_b	2 W/(mK)

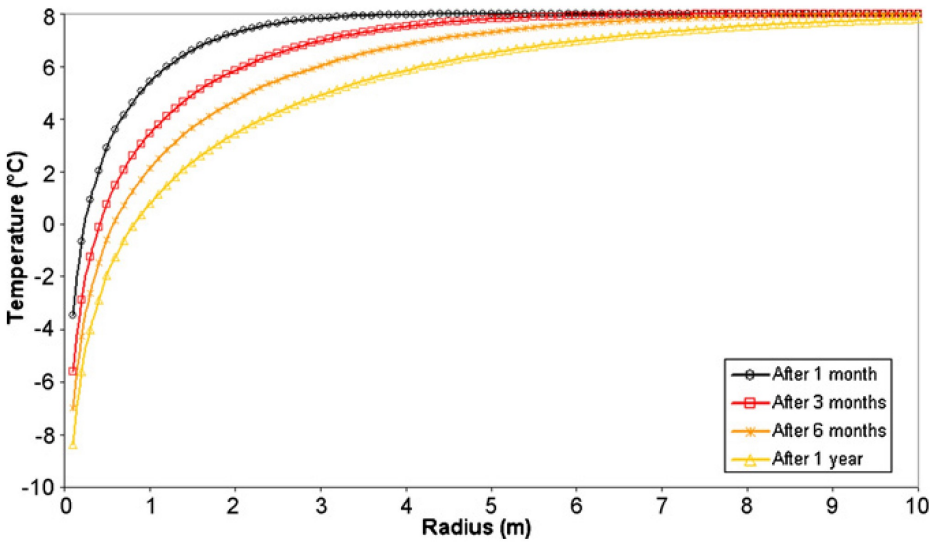

FIGURE 2.11: Temperature profile in the ground given by the ILS model (parameters are listed in TABLE 2.3) (Philippe et al., 2009).

2.5.2 Finite line source model

The finite line source model also allows for the calculation of ground temperature evolution at different distances from the borehole and at different times. The assumptions remain identical to those used in the infinite line source model, except that the BHE is now represented as a finite line. The system of equations

to be solved, as well as the initial conditions, also remain the same (Philippe et al., 2009).

An illustration of the results is given in FIGURE 2.12. It illustrates the evolution of temperature as a function of depth for different radii, using the parameters from TABLE 2.3. This result indicates that the FLS model can capture the axial conduction effects near the ends of the borehole (at 0 and 100 m in this case) (Philippe et al., 2009).

Furthermore, FIGURE 2.13 illustrates the steady-state solution using isotherms which represent the temperature difference measured at a given distance from the borehole as a function of depth. The steady-state results are valid as long as $\alpha t < H^2/90$. These results demonstrate that if another borehole is installed in the vicinity of this one, its performance will be affected. Indeed, at a distance of 20 m the difference in temperature compared with the initial ground temperature is already 10 °C. A temperature change is still observed up to 150 m away ($\Delta T = 0.5$ °C) (Philippe et al., 2009).

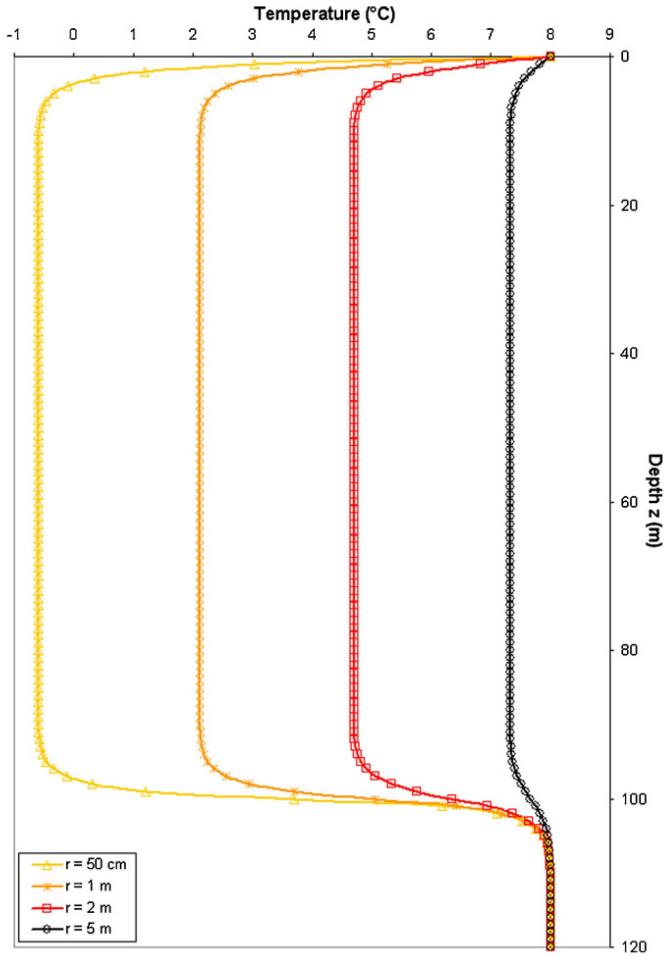

FIGURE 2.12: Temperature profile around the borehole (which extends from z = 0 to 100 m at r = 0) given by the FLS model at t = 6 months (Philippe et al., 2009).

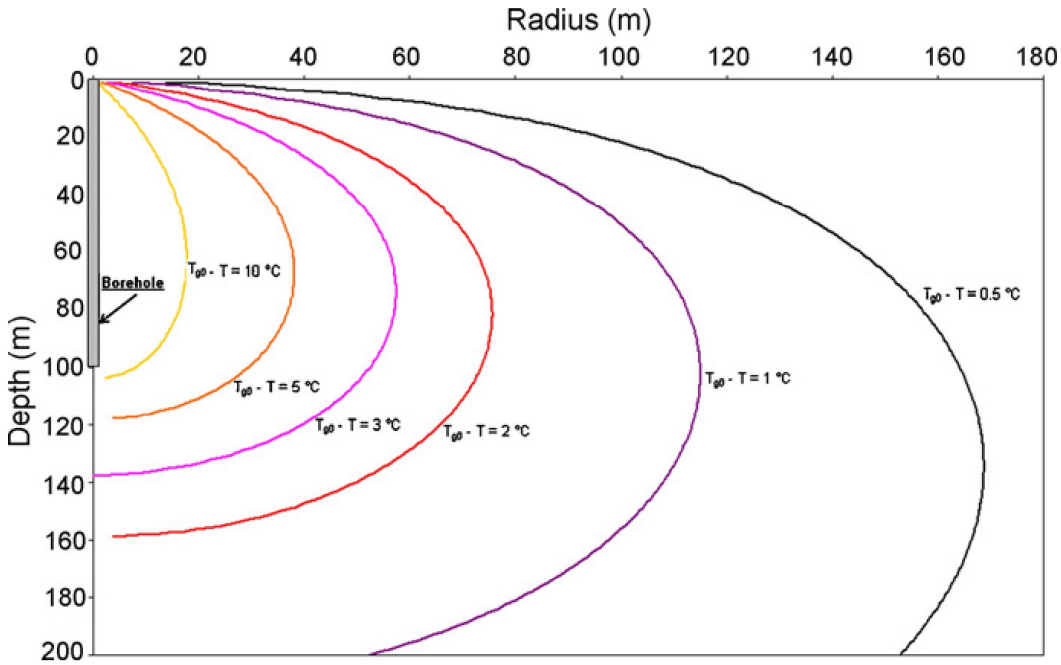

FIGURE 2.13: Isotherm curves in steady state for the FLS mode, representing the long-term temperature distribution once thermal equilibrium is reached.

2.5.3 Infinite cylindrical source model

The last model to be described is the infinite cylindrical source model. It differs from the first two models in that the BHE is replaced by an infinite cylinder. The constant heat transfer rate per unit length q' is imposed at the borehole radius ($r = r_b$). The system of equations to be solved is the same as before, except that it is now valid only if $r > r_b$. The initial conditions also remain unchanged except for EQUATION 2.18, which becomes:

$$-\lambda_b \frac{\partial \Delta T}{\partial r} 2\pi r \bigg|_{r=r_b} = q' \tag{2.19}$$

The resolution of the solution was difficult to evaluate numerically. However, solving the heat equation in Laplace space provided convincing results. These results, as well as those obtained by the FLS model, were compared with the numerical study carried out by Lee and Lam (2008), which helped validate the numerical solutions of the models (Philippe et al., 2009).

2.5.4 Conclusion

TABLE 2.4 concludes SECTION 2.5. It compares the different models to indicate which one is the most appropriate depending on the time scale at which a temperature solution is sought.

TABLE 2.4: Comparison of thermal models by applicability over time scales

Time scale	**Model**
Short term (several hours)	ICS
Long term (several months)	FLS
Medium term (several days)	ILS

Chapter 3

General context of the Relais des Ingénieurs site

The model to be calibrated in the next part of this study depends on a number of parameters. Some of these parameters depend directly on the site studied. Therefore, a general study is important to gain a good understanding of the situation at the Relais des Ingénieurs site and to adapt the model inputs accordingly. The geographic, geological, and hydrogeological context of the site will be described in this CHAPTER. These aspects will be discussed at both regional and local scales.

3.1 Geographical Context

The data used for this project come from a geothermal heat pump system used to supply heating and domestic hot water to the Relais des Ingénieurs building, a renovated farmhouse. This heat pump is connected to three BHEs located in the main courtyard of the building. The site is located in the province of Walloon Brabant in Belgium. More precisely, it is situated at Rue de Mèves 2, 1325 Chaumont-Gistoux, around ten minutes from the centre of Louvain-la-Neuve and about forty minutes from Brussels. The blue map segment in FIGURE 3.1 is an approximation of the RDI's location within Walloon Brabant. A more detailed view of the building and its surroundings in Chaumont-Gistoux is shown by the red outline in FIGURE 3.2.

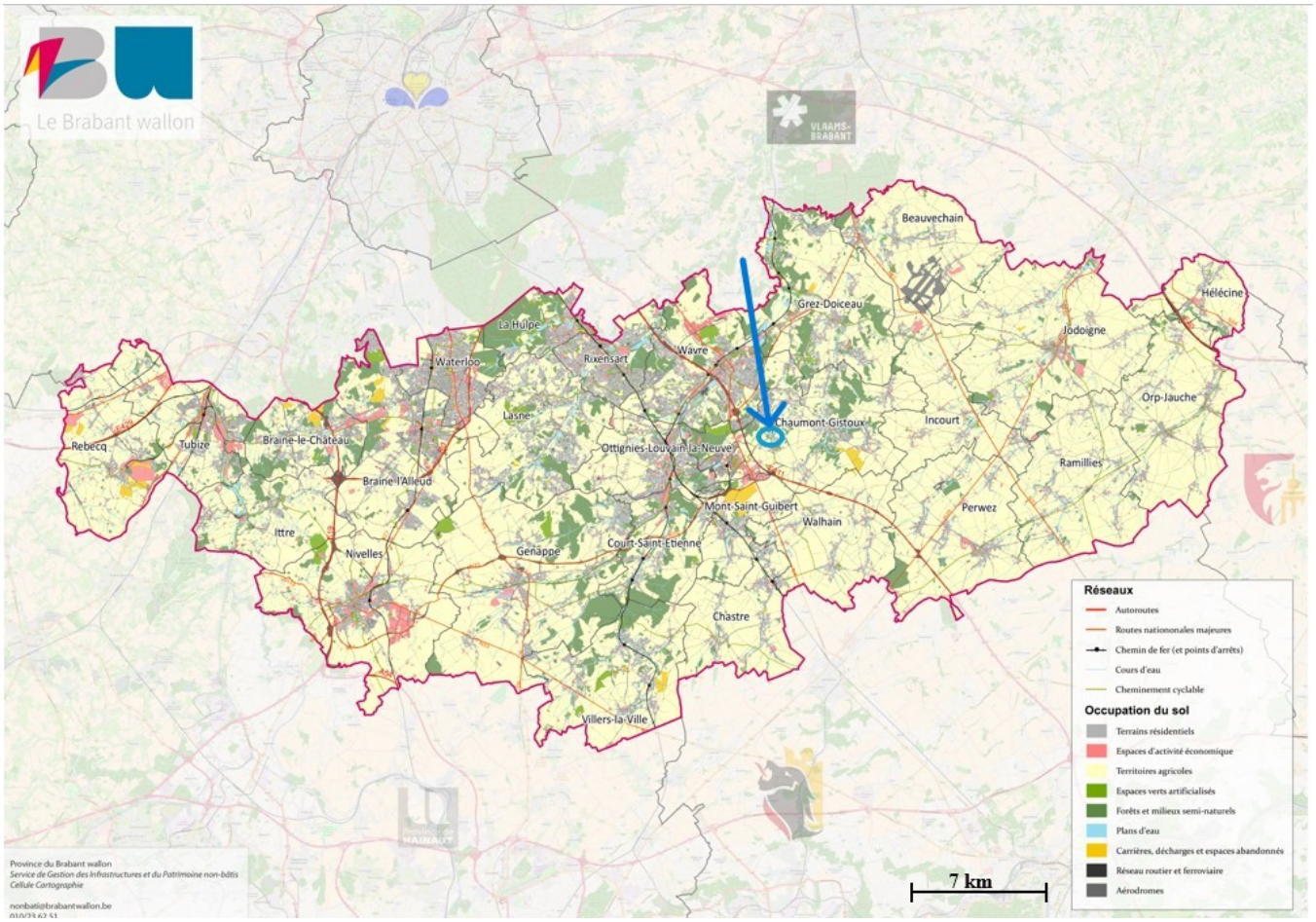

FIGURE 3.1: Location of the Relais des Ingénieurs in the Walloon Brabant region (modified from "Portail cartographique", 2024).

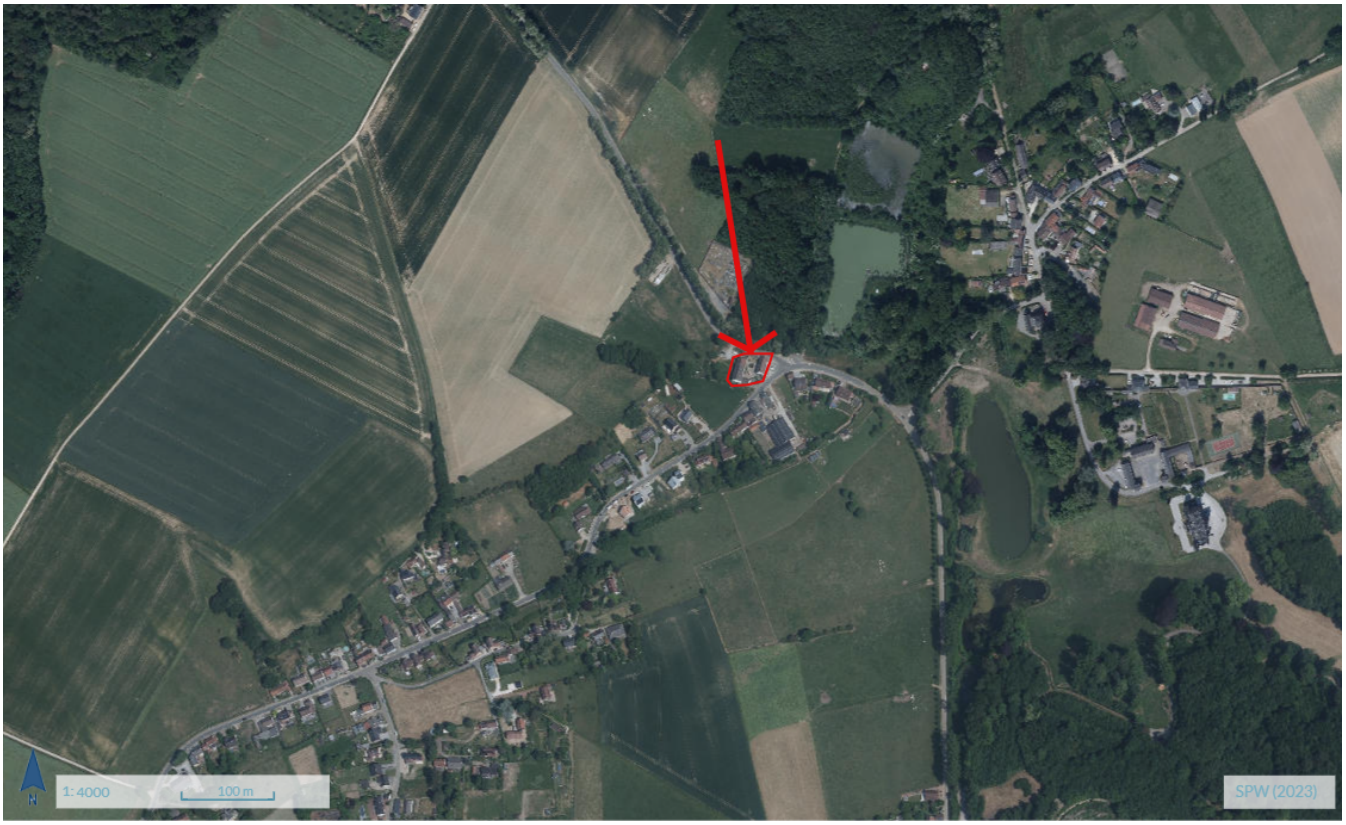

FIGURE 3.2: Location of the Relais des Ingénieurs in its neighbourhood (modified from "WalOnMap", 2025).

3.2 Geological context

The geological setting of the region of Chaumont-Gistoux consists of two distinct tectono-stratigraphic units:

1. A Cambro-Silurian basement: This unit is highly folded, faulted, and fractured due to the Caledonian orogeny, which also explains the presence of schistosity and slight metamorphism (Herbosch & Blockmans, 2012b).

2. A Meso-Cenozoic cover: This unit lies almost horizontally and unconformably over the basement. It consists of formations from the Cretaceous, Paleocene, and Eocene. The Upper Cretaceous deposits are essentially chalky marine deposits, followed by silty-carbonated, clayey, silty-clayey, sandy, and sandy-silty sediments from the Upper Paleocene and Eocene. Major variations in sea level are responsible for this lithological succession, which corresponds to a series of marine transgressions and regressions. The Paleocene and Eocene formations are often covered by Pleistocene loess and silty deposits (Herbosch & Blockmans, 2012b).

FIGURE 3.3 illustrates the geological formations found near the RDI site, on which it is represented by the part circled in red. Only formations from the Meso-Cenozoic cover outcrop on the surface. From oldest to youngest, these formations are described as follows:

1. **Hannut Formation (HAN)**: This formation consists mainly of very fine, glauconitic, clayey, silty or sandy, sometimes carbonated and more or less indurated sediments. It dates from the Upper

Paleocene and is between 10 and 40 m thick. In some places, three distinct facies can be identified. The first one, at the base of the formation, is a ten-centimetre layer of sandy plastic clay, highly glauconitic. Then alternating brownish-green sandy clays and silts with very fine sands. Finally, a homogeneous layer of fine, slightly glauconitic sands, sometimes clayey, with green to grey-green or yellow-green hues due to weathering (Herbosch & Blockmans, 2012b).

2. **Kortrijk Formation (KOR)**: This formation is composed of highly clayey sediments, these appear as slightly sandy or silty clays, often plastic, with irregular intercalations of sandy-silty lenses that are much less clayey. The colour is generally grey, often mottled with brownish-orange spots due to weathering. This unit dates from the Lower Eocene and has an average thickness of 10 m, but can reach up to 20 m in some areas (Herbosch & Blockmans, 2012b).

3. **Bruxelles Formation (BXL)**: This formation consists of alternating siliceous, sandy, or sandstone facies, more or less glauconitic, and carbonated facies. Ferruginous sandstones are frequently observed. The siliceous facies are homogeneously stratified and contain fine clayey layers. These sands are generally pure and coarse. Colours range from whitish to yellowish or green-grey depending on the glauconite content. These facies may also include sandstone lenses or concretions in the form of sandstone fistulas. The more carbonated facies contain finer sands and alternate between compacted carbonate sandstone or limestone beds and softer sandy levels. These facies are often decarbonated and turn reddish-brown. This formation dates from the Middle Eocene and its thickness is highly variable, typically between 20 and 50 m (Herbosch & Blockmans, 2012b).

4. **Sint-Huibrechts-Hern Formation (SHH)**: This formation is composed of very fine sands, more or less clayey, or sandy clays, sometimes glauconitic or micaceous, reddish-orange due to weathering. Gravel may be found at the base. This unit has a maximum thickness of a few meters and dates from the Upper Eocene (Herbosch & Blockmans, 2012b).

5. **Modern alluvium (AMO)**: Consisting of clays, silts, sands, gravels, and pebbles resulting from the erosion of local substratum. These alluvial deposits are formed by current fluvial activity and are sometimes peaty. They date from the Quaternary (Herbosch & Blockmans, 2012b).

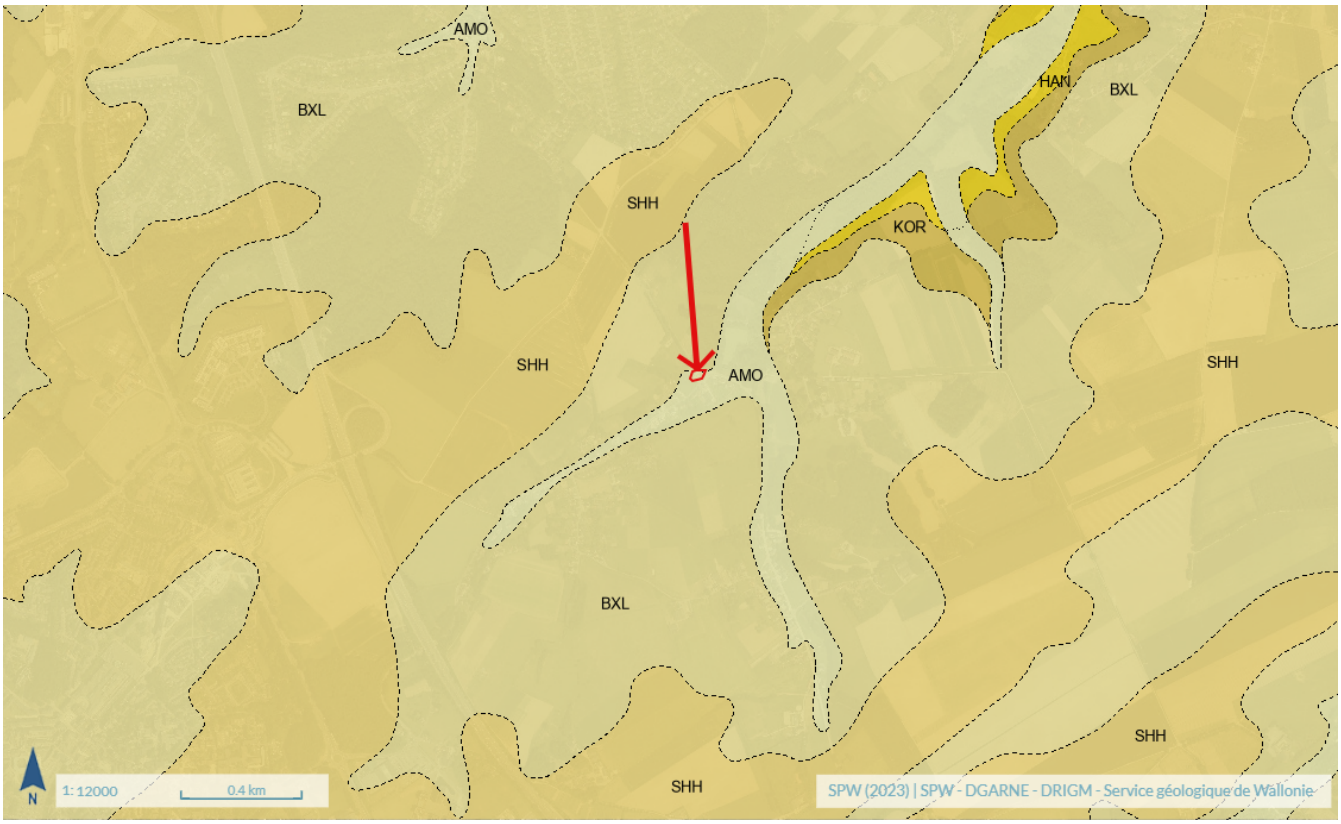

AMO **Modern alluvium** :
Loam, sand, gravel, boulders, with locally clay, peat and travertine (T).

SHH **Sint-Huibrechts-Hern Formation** :
very fine, clayey, glauconite-bearing, micaceous orange-coloured sands and very fine, yellowish-grey to orange-coloured sands, sometimes with a gravelly base,

BXL **Bruxelles Formation** :
Coarse, white, yellow, ochre, greyish-green (glauconite bearing) sands, with lenticular sandstone levels or concretions and numerous sandy fistulas.

KOR **Kortrijk Formation** :
Greyish to orange (weathered) sandy or silty clay with sandy-silty, locally glauconite-bearing, intercalations.

HAN **Hannut Formation** :
Green, greenish-grey to yellowish-green sand, clay and calcareous sandy silt or argillaceous sand, sometimes indurated (« tuffeau »), glauconite-bearing, locally with a gravelly base.

FIGURE 3.3: Geological context near the RDI site (modified from "WalOnMap", 2025).

More locally, the geothermal boreholes drilled by the company *EuroDrill* provided lithological information with depth. According to the drilling report (see APPENDIX A.2), the stratigraphy is as follows:

1. 0 - 1 m: Fill material.
2. 1 - 12 m: Silts and sands.
3. 12 - 24 m: Green sands.

4. 24 - 38 m: Grey sands and clays.
5. 38 - 48 m: Fractured basement (schists).
6. 48 - 100 m: Soft schists.

This allows the interface between the Meso-Cenozoic cover and the Cambro-Silurian basement to be identified, which is approximately 38 metres deep. The borehole data allow for the following interpretation of the lithological sequence with depth.

From the surface down to 12 meters, the formation encountered is likely the Bruxelles Formation, as it is the one that outcrops at the RDI site. If modern alluvium and the fill materials are not considered, it is expected not to encounter the Sint-Huibrechts-Hern Formation, which is geologically younger than the Bruxelles Formation. From 12 to 24 metres, the lithology is still characteristic of the Bruxelles Formation. This facies is slightly different from the one encountered at lower depths. Between 24 and 38 meters, the sequence could correspond to the Hannut Formation. Below this, the basement is reached. It is difficult to determine whether the basement belongs to the Blanmont or Tubize Formation. However, the lithology is closer to that of the Tubize Formation, which consists mainly of schists and siltstones, whereas the Blanmont Formation is characterized by quartzites and quartzitic sandstones.

The geological map, shown in APPENDIX A.1, illustrates the geological uncertainties in the vicinity of the site. First, concerning the Cambro-Silurian basement, there is some ambiguity. According to the geological map, cross-section b-b' (located approximately 2 km north-east of the site) and cross-section c-c' (around 1.7 km west of the site) both indicate that the Blanmont Formation should underlie the site. However, this remains a hypothesis, and the lithology observed during drilling is more similar to that of the Tubize Formation.

Another uncertainty concerns the presence of the Kortrijk Formation. It appears on the right bank of the nearby stream, and it would be unusual for this formation to disappear suddenly on the left bank, where the RDI is located. However, its strongly clayey and slightly sandy lithology does not seem to have been detected during drilling. At least, no distinct clayey facies between the Bruxelles and Hannut Formations are described in the drilling report. In cross-section c-c' (FIGURE A.3), this formation is absent even though it is not very far from the site. In contrast, cross-section b-b' (FIGURE A.2) includes it but its position is uncertain. Therefore, it is possible that some of the clays observed between 24 and 38 meters belong to the Kortrijk Formation, but without a clear transition between it and the Hannut Formation. Alternatively, the Kortrijk Formation may indeed be absent or extremely thin at the borehole site. Both hypotheses are plausible, given the geological uncertainties in the maps and cross-sections in APPENDIX A.1, as well as the limited precision and detail in the drilling report.

The approximate position of the RDI is marked by a red circle in FIGURE A.1. In FIGURES A.2 and A.3, the RDI is indicated by a red arrow, located approximately 2 km south-west of cross-section b-b' and 1.7 km east of cross-section c-c'. The site's elevation is 99 meters.

These lithological details will be important later in the study. For example, to estimate the thermal conductivity of the ground.

3.3 Hydrogeological context

The RDI is located within the Pisselet hydrographic basin, a tributary of the Dyle river. This stream flows approximately one hundred meters to the east of the building.

From a hydrogeological perspective, the units that may be encountered from the surface to depth (from youngest to oldest) are as follows:

1. The Eocene sand aquifer, within the Bruxelles Formation (Ruthy, 2017).
2. The Paleocene sand aquifer, within the Hannut Formation (Ruthy, 2017).
3. Either a Cambro-Silurian basement aquitard with local aquifer levels (if the basement is attributed to the Tubize Formation), or a Cambro-Silurian basement aquifer (if the basement is interpreted as the Blanmont Formation) (Ruthy, 2017). The latter is less likely, as the theoretical lithology of the Blanmont Formation does not match the borehole observations as closely as that of the Tubize Formation.

The cross-section shown in FIGURE 3.6 corresponds to the light green line on the hydrogeological map of Wavre-Chaumont-Gistoux presented in FIGURE 3.4. The approximate location of the RDI is indicated by the red arrow on the cross-section, bearing in mind that the site is located approximately 1.7 km east of the section line. This cross-section shows the hydrogeological units encountered with depth. As before, there is some uncertainty regarding the nature of the formation that constitutes the basement. The red dashed line represents a hypothetical trace of the piezometric surface, based on interpolated isopiestic lines. According to this interpretation, the Eocene sands aquifer is therefore partially saturated.

FIGURE 3.4 also presents these interpolated isopiestic lines for the Eocene sand aquifer, shown as a red dashed line. These allow for an estimate of the piezometric elevation within the sands. By interpolation, the piezometric level at the site should be between 93 and 95 meters. Unfortunately, because the piezometric level is not mentioned in the drilling report, a more precise estimate cannot be made. The blue arrows indicate the probable direction of groundwater flow in the Eocene sands. These flows are oriented towards the north-east, and due to the position of the boreholes, the flow direction is nearly parallel to the alignment of the boreholes. Based on the direction of groundwater flow, borehole 3 is located upstream, borehole 1 downstream, and borehole 2 approximately halfway between the two (see FIGURES A.7, A.5 and A.6 in APPENDIX A.2). Because the Pisselet stream is located very close to the site and acts as a drainage feature, it may influence the flow direction in the upper part of the soil, possibly within an unconfined aquifer in the alluvial deposits. Near the surface, the groundwater flow is therefore expected to have a stronger eastward component. Given that the geological basement underlying the Eocene sand aquifer is mainly composed of schist, groundwater flow at greater depths is expected to be limited due to the low hydraulic conductivity of this formation.

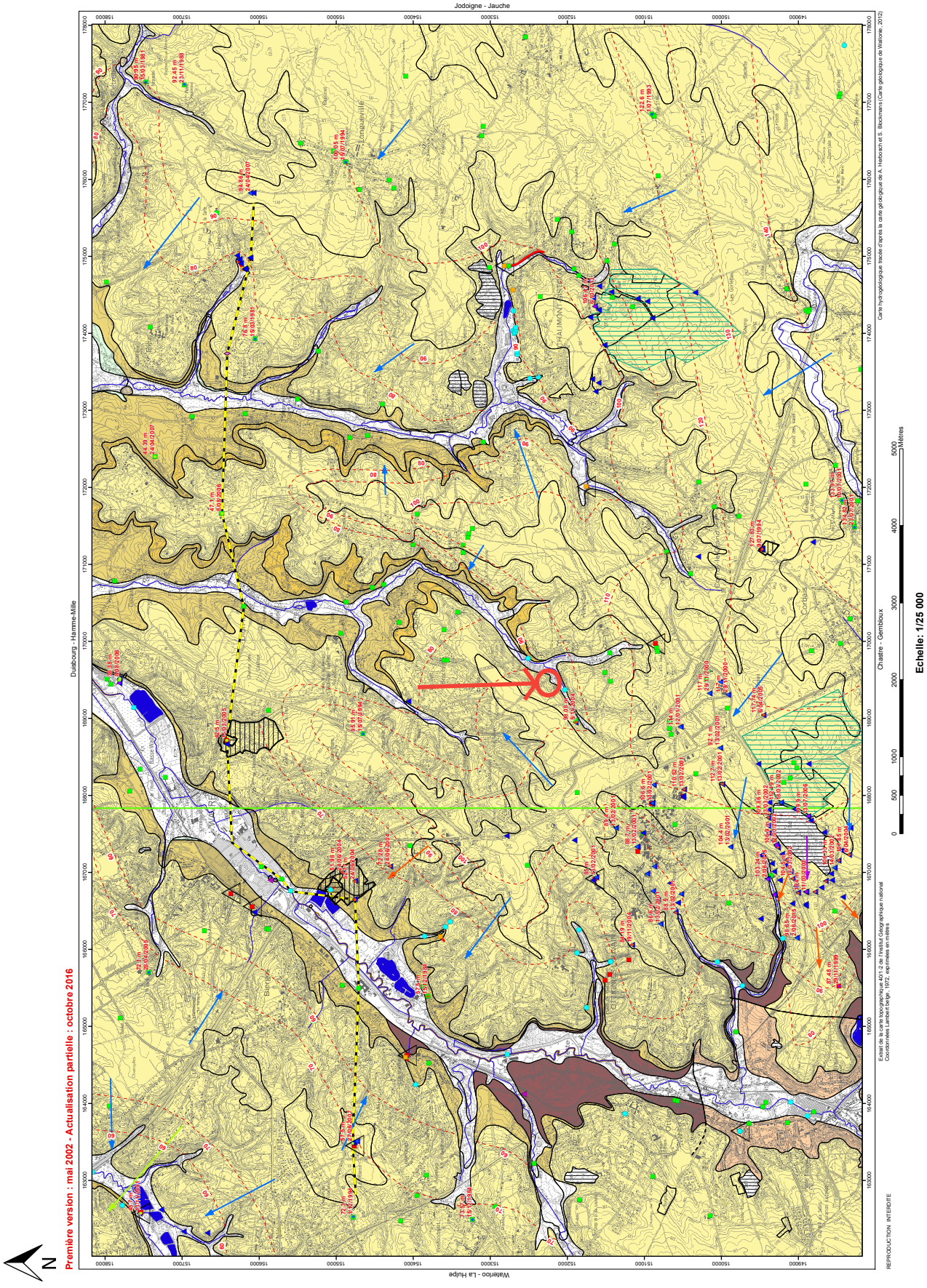

FIGURE 3.4: Regional hydrogeological map of Wavre-Chaumont-Gistoux (modified from Ruthy, 2017).

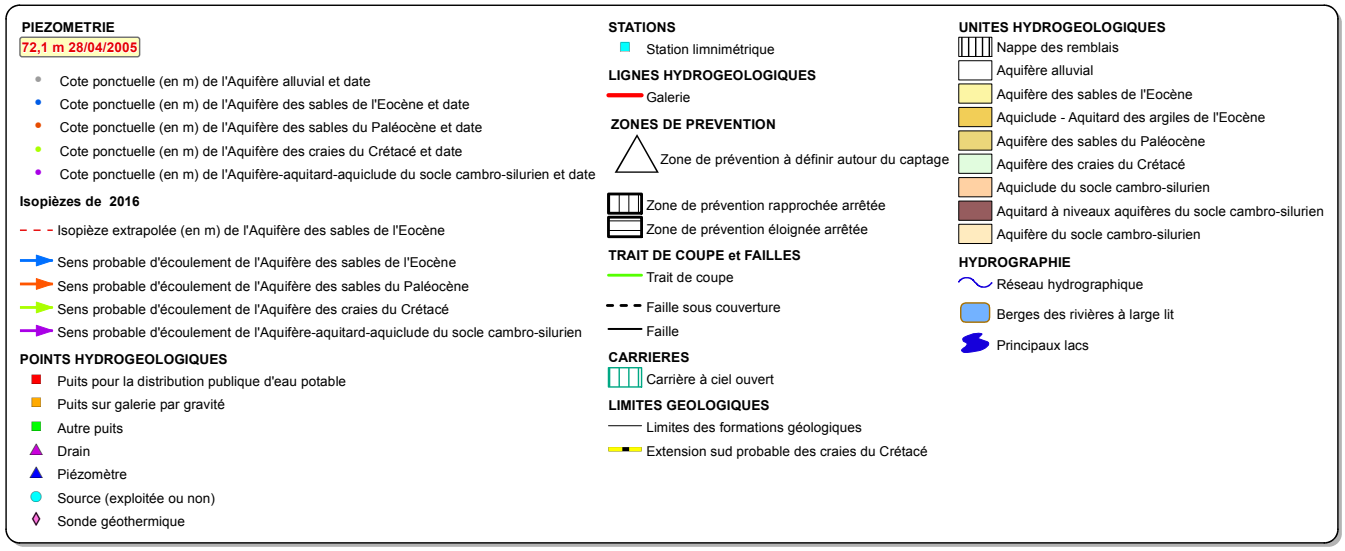

FIGURE 3.5: Legend for FIGURE 3.4 (Ruthy, 2017).

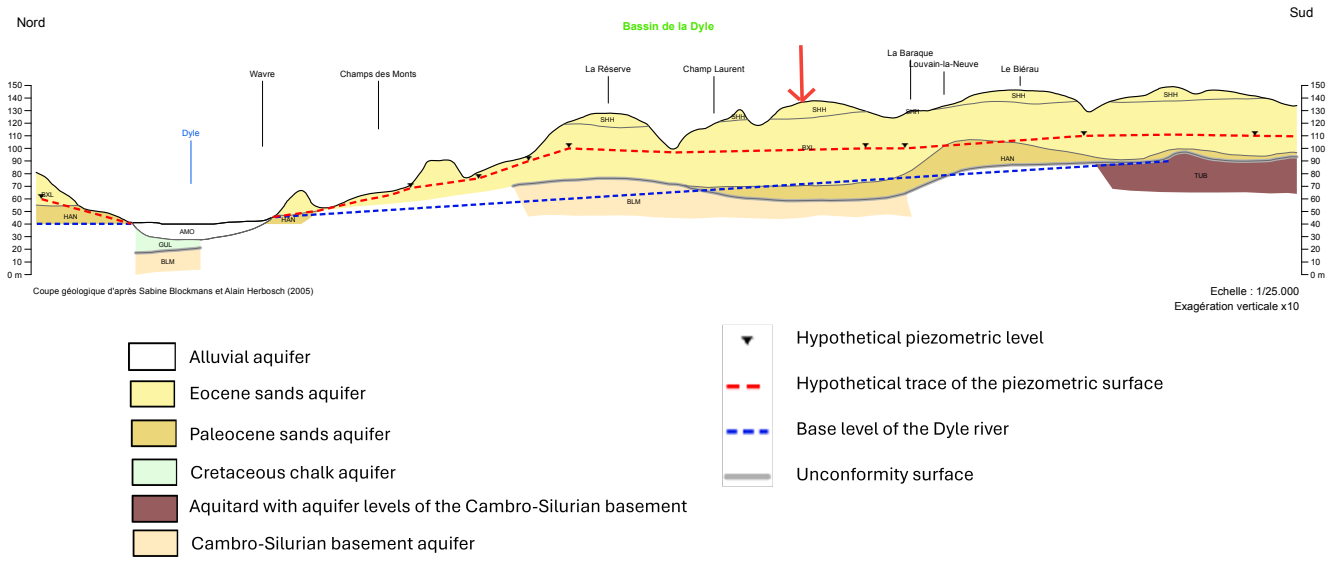

FIGURE 3.6: Cross-section from the hydrogeological map of Wavre-Chaumont-Gistoux (FIGURE 3.4) (modified from Ruthy, 2017).

Chapter 4

Analytical model

To evaluate subsurface temperatures based on the thermal power extracted from the ground, an analytical model developed by Erol et al. (2015) is used. This model attempts to estimate the ground temperature in the vicinity of the boreholes as reliably as possible. One of the advantages of this model is that it allows heterogeneous heat loads to be considered. This CHAPTER outlines the theoretical principles on which the model is based, then describes the parameters that must be defined and evaluates them.

4.1 Main equations

The analytical solution is a fast and flexible tool for studying the thermal response of the ground (Coen et al., 2021). In this model, the Green's function, which is the solution to the heat conduction/advection/dispersion equation in porous media, is convoluted to provide an analytical solution. This solution enables the evaluation of the temperature variations in the ground due to discontinuous heat extraction by BHEs. This solution showed results comparable to those obtained by numerical models, but with much faster computation times.

In order to obtain an analytical solution for ground temperature change, the analytical convolution is applied between the Green's function and a rectangular function or pulses, which have different period lengths and pulse heights. The Green's function represents the fundamental solution to the heat conduction/advection/dispersion equation in porous media.

By projecting the heat transfer equation (EQUATION 2.8) for a groundwater flow occurring in the x-direction, the following expression is obtained (Erol et al., 2015):

$$\rho_b c_b \frac{\partial T}{\partial t} = \left(\lambda_x \frac{\partial^2 T}{\partial x^2} + \lambda_y \frac{\partial^2 T}{\partial y^2} + \lambda_z \frac{\partial^2 T}{\partial z^2} \right) - u_x \rho_w c_w \frac{\partial T}{\partial x} + s \tag{4.1}$$

where u_x is Darcy's velocity in the x-direction $[m/s]$, and s is a volumetric heat source $[W/m^3]$. The volumetric heat capacity of the ground ($\rho_b c_b$) is calculated as the weighted arithmetic mean of the volumetric heat capacities of the solids $\rho_s c_s$ and the water $\rho_w c_w$, based on the porosity n $[-]$ (Erol et al., 2015):

$$\rho_b c_b = (1 - n)\rho_s c_s + n \rho_w c_w \tag{4.2}$$

The components of the effective longitudinal and transverse thermal conductivities in the three coordinate directions are computed as follows:

$$\lambda_x = \lambda_b + \alpha_l \rho_w c_w u_x \tag{4.3}$$

$$\lambda_y = \lambda_z = \lambda_b + \alpha_t \rho_w c_w u_x \tag{4.4}$$

where α_l and α_t are the longitudinal and transverse thermal dispersivities, respectively. λ_b is the bulk thermal conductivity of the porous medium in the absence of groundwater flow (Erol et al., 2015).

After solving the differential EQUATION 4.1 for heat transfer in porous media using the Green's function G of a pulse point source $Q_p\ [J]$, this solution is applied for the response of a constant line source of finite length H (based on the finite line source theory described in SECTION 2.5.2) in order to take into account both axial effect and groundwater flow. Following mathematical manipulations described in Erol et al. (2015), the analytical solution for a multit-BHEs configuration is obtained (Coen et al., 2021; Erol et al., 2015):

$$\Delta T(x,y,z,t) = Q_L \underbrace{\sum_{j=1}^{s} \frac{1}{8\pi\sqrt{\lambda_x \lambda_y}} \cdot \frac{1}{t} \exp\left(-\left[\frac{(x-x_j-v_T t)^2}{4\lambda_x t/(\rho_b c_b)} + \frac{(y-y_j)^2}{4\lambda_y t/(\rho_b c_b)}\right]\right)\left[\operatorname{erf}\left(\frac{z}{\sqrt{4\lambda_z t/(\rho_b c_b)}}\right) - \operatorname{erf}\left(\frac{z-H}{\sqrt{4\lambda_z t/(\rho_b c_b)}}\right)\right]}_{C(x,y,z,t)} \tag{4.5}$$

where Q_L is the pulse heat input per meter depth $[J/m]$, v_T is the thermal transport velocity $[m/s]$, H is the borehole length $[m]$, and s is the number of BHEs.

The sum $C(x,y,z,t)$ is convolved using the method described in Erol et al. (2015), leading to the final expression:

$$\Delta T(x,y,z,t) = \sum_{i=0}^{n-1} q_L(i\Delta t) \cdot C(x,y,z,t-i\Delta t) \cdot \Delta t \tag{4.6}$$

where $q_L(t)$ is a rectangular heat extraction function $[W/m]$, n denotes the time span, and $i\Delta t$ is the time delay associated with each unit impulse.

EQUATION 4.6 is the one solved in the Python code. The study by Erol et al., 2015 demonstrated that analytical results were similar to the numerical results, while requiring a much shorter calculation time. These results were validated both with and without groundwater flow.

At the borehole wall, the temperature T_b can be obtained from the temperature difference ΔT, given by EQUATION 4.6, and the initial ground temperature T_0:

$$T_b = T_0 + \Delta T \tag{4.7}$$

Based on this borehole wall temperature, it is possible to determine the mean temperature of the heat carrier fluid, $T_{fluid,mod}$ (Coen et al., 2021):

$$T_{fluid,mod} = T_b + R_b \cdot q_L \tag{4.8}$$

where T_b is the temperature at the borehole wall calculated with EQUATION 4.7 $[K]$, R_b is the fluid-to-ground thermal resistance $[(Km)/W]$, and q_L is the linear heat extraction rate $[W/m]$. EQUATION 4.8 is only valid under the assumption of a steady-state heat flux in the borehole, as R_b does not account for the borehole's heat capacity (Coen et al., 2021).

The fluid temperature $T_{fluid,mod}$ can also be expressed as:

$$T_{fluid,mod} = \frac{T_{fluid,mod_{in}} + T_{fluid,mod_{out}}}{2} \tag{4.9}$$

where $T_{fluid,mod_{in}}$ and $T_{fluid,mod_{out}}$ are the temperatures of the heat carrier fluid at the inlet and outlet of the geothermal loop, respectively.

4.2 Input parameters

The Python script used to solve the analytical model requires a set of input parameters and variables, which are briefly introduced and discussed below. These initial values are based on site-specific information and literature data, and serve as a starting point for initial modelling. This initial configuration allows for a preliminary evaluation of the model's behaviour. In a second step, the most influential and uncertain parameters will be refined through a calibration process, in order to improve the agreement between modelled and monitored temperatures.

1. **General parameter**

   - t_{span} is the total simulation time in days. It depends on the number of days being analysed. It was initially set to 427, which corresponds to the total number of days available in the dataset. Even this time span is later refined, and a shorter simulation period is selected, as detailed in SECTION 6.1.

2. **Subsurface parameters**

   - T_0 is the initial ground temperature in °C. A value of 10.2 °C is used, corresponding to the average annual temperature in Belgium measured between 1990 and 2020 ("Atlas climatique", 2020). Unfortunately, no Thermal Response Test (TRT) was carried out on the site, so it is not possible to have a better estimate of the temperature.
   - λ_b is the thermal conductivity of the ground in W/mK. Based on the geological information presented in SECTION 3.2 and the thermal conductivity values provided in TABLE 2.2, a value of 2.3 $W/(mK)$ was chosen to represent the ground, considering the proportions of sand, clay, and schist.
   - $\rho_b c_b$ is the volumetric heat capacity of the ground in J/m^3K. Based on the geology described in SECTION 3.2 and the values listed in (CSTC, 2016), a value of $2.4 \cdot 10^6$ $J/(m^3K)$ was selected.

3. **Groundwater parameters**

   - u_x is the specific discharge in the x-direction in m/s. Initially, given the generally low values of this velocity, it was set to zero. Nonetheless, a value was also calculated using Darcy's

law to assess the impact of groundwater flow on the model. Based on Darcy's law, specific discharge can be calculated using the following equation:

$$u_x = K\frac{\Delta h}{L} \tag{4.10}$$

where K is the hydraulic conductivity $[m/s]$, $\frac{\Delta h}{L}$ is the hydraulic gradient with Δh the head difference $[m]$, L is the distance between two points $[m]$. The specific discharge in the Eocene sand aquifer was calculated using a hydraulic conductivity of $6 \cdot 10^{-6}\ m/s$ (Collignon et al., 2023; Dassargues 2019; "Masse d'eau souterraine RWE051", 2006), and a hydraulic gradient of $\frac{10}{700}$ based on FIGURE 3.4, giving:

$$u_x = 6 \cdot 10^{-6}\frac{10}{700} \tag{4.11}$$

$$= 8.57 \cdot 10^{-8}\ m/s \tag{4.12}$$

- $\rho_w c_w$ is the volumetric heat capacity of water in $J/(m^3K)$, with a value of $4.2 \cdot 10^6\ J/(m^3K)$.
- α_l is the longitudinal thermal dispersivity coefficient in m. A value of 1 m was used (Gigot et al., 2023).

4. **Borehole parameters**

- $type\_of\_BHE$ represents the type of probe installed in the borehole, a double U-tube in this case.
- H is the length of the borehole in meters, here 100 m.
- r_b is the borehole radius in m. For the RDI geothermal system, it is 0.089 m.
- r_{po} is the outer radius of the U-pipe legs in m, which is 0.016 m.
- r_{pi} is the inner radius of the U-pipe legs in m, which is 0.013 m.
- k_b is the thermal conductivity of the grout (filling material) in $W/(mK)$. The boreholes were filled using two different materials by *EuroDrill*, a bentonite grout for approximately two-thirds of the total borehole depth, and silica gravel for the remaining third. A representative thermal conductivity of 1.5 $W/(mK)$, combining the conductivities of both materials, was selected for the model.
- k_p is the thermal conductivity of the U-pipe in $W/(mK)$. Since the installed probe is made of polyethylene, a thermal conductivity of 0.4 $W/(mK)$ was selected (Stober and Bucher, 2021).

5. **Fluid parameters inside the pipe**

- V_f is the fluid flow rate in m^3/s. Flow meters positioned after the collector provide the flow rate of the fluid circulating in each borehole. The sum of the three individual flow rates (19, 28.5, and 37 L/min) was converted to cubic metres per second and averaged to obtain the average flow rate per borehole, i.e., $\frac{0.0014083}{3}\ m^3/s$. These flow meters (shown in FIGURES A.8 to A.10 in APPENDIX A.3) provide a direct measurement of the volumetric flow rate for each borehole, which is essential for estimating the thermal power extracted from the ground using EQUATION 5.1, presented in CHAPTER 5. However, as illustrated in the FIGURES, these instruments lack precision, which may affect the accuracy of the calculated power values.

The fluid inside the pipe is a glycol-water mixture with a glycol concentration of approximately 20%. The values of the following properties were obtained by interpolating data for glycol concentrations of 50%, 40%, 30%, and 25%, since no values were available for 20%. These interpolated values are deemed acceptable due to consistent property trends in the property data. They are presented in APPENDIX A.4. Furthermore, these properties have limited influence on the model results, so interpolation is considered acceptable.

- k_f is the thermal conductivity of the fluid in $W/(mK)$, with a value of 0.52 $W/(mK)$.
- c_f is the heat capacity of the fluid in $J/(kgK)$, with a value of 3989.3 $J/(kgK)$.
- ρ_f is the fluid density in kg/m^3, with a value of 1011.7 kg/m^3.
- μ_f is the dynamic viscosity of the fluid in $kg/(ms)$, with a value of 0.00178 $kg/(ms)$.

Most of the parameters listed in points **4** and **5** are used to calculate the fluid-to-ground thermal resistance of the borehole. This resistance is computed within the Python script based on the borehole and fluid characteristics. In this initial case, the calculated value of R_b is 0.0865 $(Km)/W$.

Chapter 5

Datasets

In order to model the temperature evolution of the heat carrier fluid and the surrounding ground using the analytical model, and to compare it with the monitored temperatures at the site, two datasets were analysed. These datasets, collected from the geothermal installation at the Relais des Ingénieurs, include heat pump monitoring data and energy consumption records. This CHAPTER presents the content of these datasets, as well as the methodology used to process them. The objective is to quantify the thermal load extracted from the ground.

To provide a clearer understanding of the hydraulic configuration and the approximate locations of the temperature sensors discussed throughout this CHAPTER, the hydraulic layout of the RDI is included in FIGURE A.16 of APPENDIX A.5. Annotated elements indicate the main components and sensor positions relevant to the data analysis.

5.1 Dataset 1

5.1.1 Description

This first dataset is the main one used in the project. It contains measurements collected from 09/01/2024 to 10/03/2025. However, some periods are missing due to heat pump malfunctions. The important information to take from this dataset is firstly the timestamps indicating when each measurement was taken. Most of the time, measurements were taken every two minutes.

Secondly, data monitoring provides temperature measurements from the primary circuit, which corresponds to the geothermal loop, at both the inlet and outlet of the heat pump (corresponding to points 1 and 2, respectively, in FIGURE A.16). From these values, it is possible to estimate the ground temperature. Indeed, the inlet temperature of the heat pump corresponds to the outlet of the geothermal loop, so the measured fluid temperature can be considered representative of the ground temperature. Additionally, knowing both the fluid temperatures and the flow rate in the pipes allows for the calculation of the thermal power extracted from the ground, as expressed in EQUATION 5.1, which is detailed later in SECTION 5.1.2. In this study, the mean of the inlet and outlet temperatures is used as the monitored temperature of the heat carrier fluid.

The dataset also includes a heat pump operation indicator, which is useful for analysing data only when the heat pump is operating. Additional important information includes the inlet and outlet temperatures

of the secondary circuit, which corresponds to the building loop. These temperatures are measured at the inlet and outlet of the heat pump, on the building side. Another indicator specifies whether the secondary circuit is supplying Domestic Hot Water (DHW) or space heating for the RDI. In the layout shown in FIGURE A.16, the temperature sensors correspond to point 5 for the inlet of the heat pump (i.e., the return from the building loop), point 4 for the outlet of the heat pump when supplying surface heating, and point 3 when supplying DHW. It should be noted that during summer, the geothermal heat pump (labelled "G300 géo" in one of the red circles in FIGURE A.16) is switched off. An aerothermal heat pump (labelled "G200 aero" in the other red circle) is then used to meet the building's hot water and heating needs. This air-source system is activated when the average outdoor temperature is judged to be higher than the underground temperature. However, in practice, this switch is made arbitrarily, without direct measurement of the ground temperature. Based on the data, the switch appears to have occurred on 27/06/2024.

It could be interesting to measure the underground temperature. When it becomes too low, and therefore the geothermal heat pump is no longer efficient, the activation period for the aerothermal heat pump begins. Similarly, the shutdown of the aerothermal heat pump is also done arbitrarily when the outside temperature becomes lower, which happened on 22/11/2024. As with the switch to the aerothermal system, it could be advantageous to restart the geothermal system once the ground has had time to recover its temperature thanks to the effect of free cooling.

5.1.2 Analysis

An analysis of the dataset was carried out to better understand the evolution of the monitored values and their interactions. First, the raw temperature data at the outlet of the geothermal loop are shown in FIGURE 5.1. This FIGURE illustrates the large fluctuations in the inlet temperature of the heat pump. These variations are mainly caused by the inclusion of measurements taken when the geothermal heat pump was turned off. In such situations, the configuration of the hydraulic system, more specifically the position of the pipes for the circuits and the position of the temperature sensors, results in higher recorded temperatures in the primary circuit. This occurs because of the short distance between the primary and secondary circuits within the heat pump, which allows some heat transfer from the secondary to the primary circuit. Additionally, it is possible that the pipes of the primary circuit absorb heat from the room environment. These heat transfers will at least affect the first temperature measurement when the system is restarted, but this impact is considered negligible. FIGURE 5.1 shows gaps in the evolution of the ground temperature, indicated by the blue arrows. These interruptions correspond to periods when the geothermal heat pump "G300 géo" was turned off due to malfunctions. In total, five such events occurred. For instance, the second blue arrow highlights the absence of data between 12/03/2024 and 04/04/2024. In addition, the green arrow in FIGURE 5.1 illustrates the explanations provided in SECTION 5.1.1 concerning the shutdown of the geothermal heat pump and the switch to the aerothermal heat pump. The start of the green arrow (27/06/2024) marks the deactivation of "G300 géo", while its end (21/11/2024) corresponds to its reactivation, and inversely for "G200 aero", which was active during this period.

The first step in processing the data was to retain only the periods during which the geothermal heat pump was operating. Then, temperatures from the geothermal loop and the building loop were averaged on an hourly and daily basis, considering only the system's active periods. FIGURE 5.2 compares these two temporal resolutions for the underground temperature (i.e., the fluid temperature at the outlet of the geothermal loop, corresponding to the inlet of the heat pump). The graph shows that the significant fluctuations observed in the hourly data are smoothed when using daily averages. During the period when

the aerothermal heat pump was operating (i.e., from 27/06/2024 to 21/11/2024, indicated by the green arrow in FIGURE 5.2), the geothermal heat pump was completely switched off. Consequently, no valid temperature measurements from the geothermal loop should be available during this interval. However, the graph still displays temperature curves over this period: these values correspond to simple hourly or daily averages taken directly from the raw dataset, without applying any filtering based on the system's operational status. They are included solely to preserve the visual continuity of the graph and to show the differences in average temperatures from one hour/day to the next, but they do not represent meaningful or usable data. Additionally, FIGURE 5.2 shows a continuous decrease in underground temperature from early January to mid-February. Unfortunately, no data are available before 09/01/2024, which makes it difficult to determine why temperatures were initially high. The lowest recorded ground temperature is observed in late April 2024. Between 15/05/2024 and 26/06/2024, the ground temperature remains relatively stable.

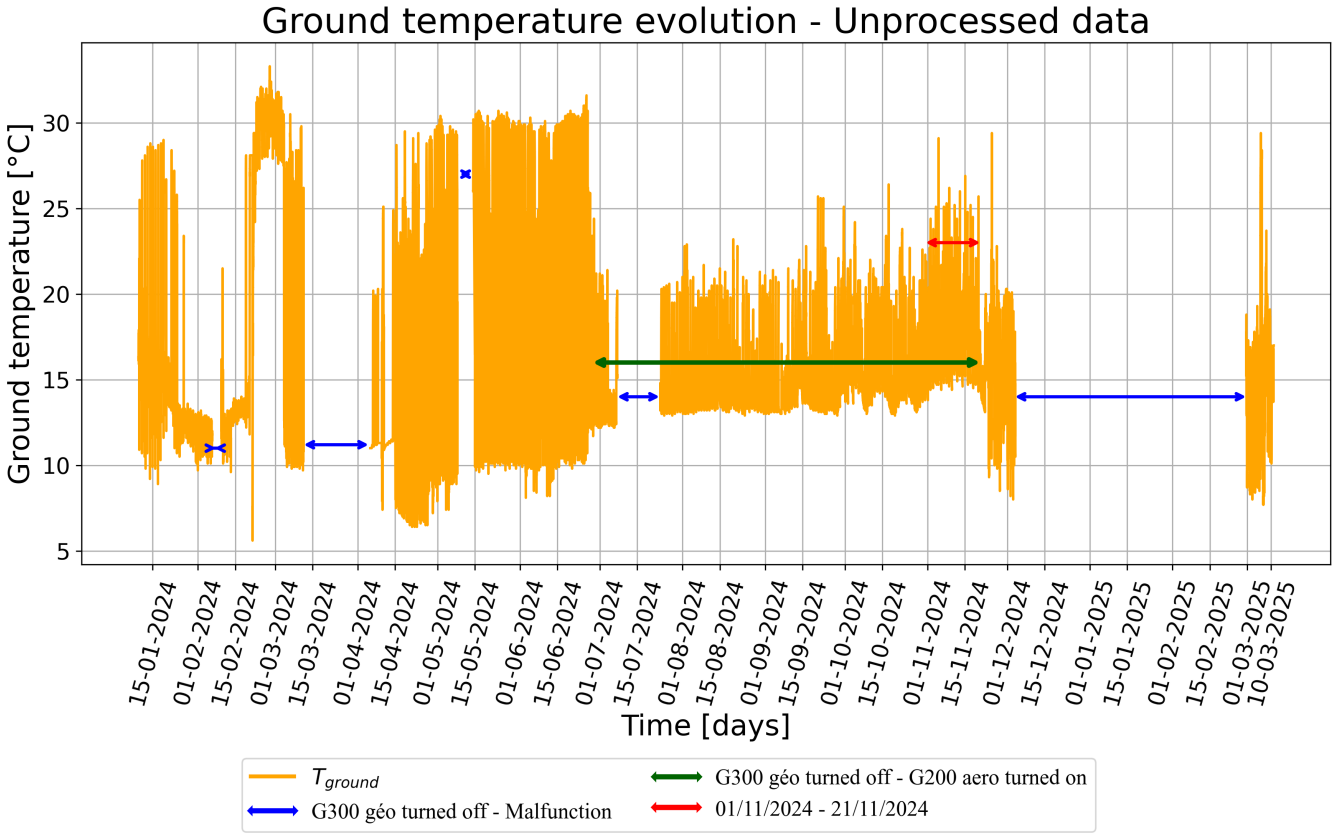

FIGURE 5.1: Evolution of ground temperature with raw data.

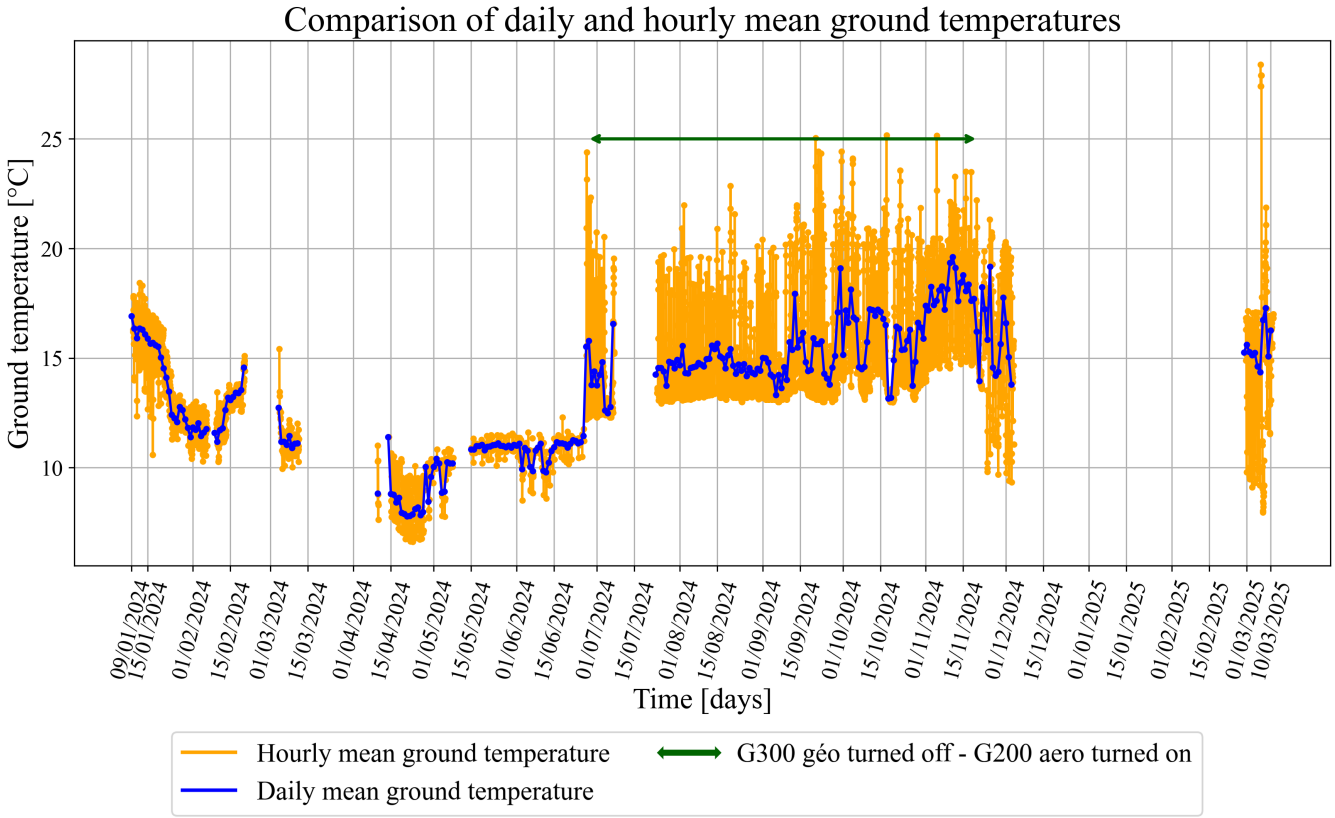

FIGURE 5.2: Hourly and daily mean ground temperatures, filtered to exclude inactive periods except during the summer shutdown (green arrow) for continuity.

In summer, although the heat pump compressor is completely off, as there is no heat supplied to the secondary circuit by the primary circuit directly via the heat pump, thermal exchange still occurs between these two circuits. A natural cooling exchanger (represented by the light blue rectangle in FIGURE A.16) passively transfers heat from the secondary circuit, more precisely from the surface heating loop, to the primary circuit. This component of the hydraulic system recovers heat from the building to provide cooling if needed. Unfortunately, this thermal exchange cannot be quantified. Firstly, the dataset does not include any indicator related to the activation of the building's cooling system, making it impossible to know when the circulation pumps for the borehole fluid are operating. Secondly, the temperature difference across the natural cooling exchanger cannot be measured, as there are no sensors installed at these specific locations on either the primary or secondary circuit. The only available temperature data come from sensors located within the heat pump, after the exchange has already occurred (sensors 1 and 2 in FIGURE A.16). Moreover, the ground temperature during the summer period cannot be inferred, as a temperature sensor would be needed upstream of the natural cooling exchanger to isolate the real temperature of the fluid returning from the borehole.

In addition to the inability to quantify the summer heat exchange and determine the ground temperature due to the lack of sensors, FIGURE 5.1 (green arrow period) shows very rapid fluctuations in the inlet temperature of the heat pump. These variations suggest that the temperature measured at the heat pump inlet does not correspond to the actual temperature of the heat carrier fluid within the borehole, just before it is reinjected into the ground. In principle, the fluid temperature at the inlet of the heat pump (sensor 1 in FIGURE A.16) should be close to the reinjection temperature into the ground since no heat

exchange is expected to occur within the heat exchanger of the heat pump when the system is off. These anomalies are likely caused by the same phenomenon observed during the periods when the geothermal heat pump is turned off: thermal interference from the secondary circuit on the primary circuit. Between 01/11/2024 and 21/11/2024, the red arrow on FIGURE 5.1 highlights a period during which the inlet temperatures are particularly high compared to the rest of the green arrow. The analysis is therefore focused on this interval. FIGURE A.17 (in APPENDIX A.6) shows the evolution of the domestic hot water tank temperature (represented by the purple rectangle in FIGURE A.16) and the inlet temperature of the heat pump on the primary side. To better identify the artefact, a shorter time window between 02/11/2024 and 05/11/2024 (corresponding to the green arrow in FIGURE A.17) is examined in FIGURE 5.3, which also displays the evolution of these two temperatures. FIGURE 5.3 suggests a link between the temperature peaks in the domestic hot water tank (and thus the circulation of hot fluid in the secondary circuit) and the sudden increases in the primary circuit inlet temperature. While this correlation is not always consistent or systematic, several events, particularly the first temperature peak of each day, indicate that the primary temperature rises shortly after the tank temperature increases. This remains a hypothesis, but it is considered plausible. Furthermore, the largest temperature jumps at the heat pump inlet appear to follow a periodic pattern, typically occurring early in the morning. This behaviour may be explained by daily variations in the operation of the hydraulic system. As a result, during the summer period, the inlet temperatures measured at the heat pump cannot be used to estimate the temperature of the heat carrier fluid returning to the borehole.

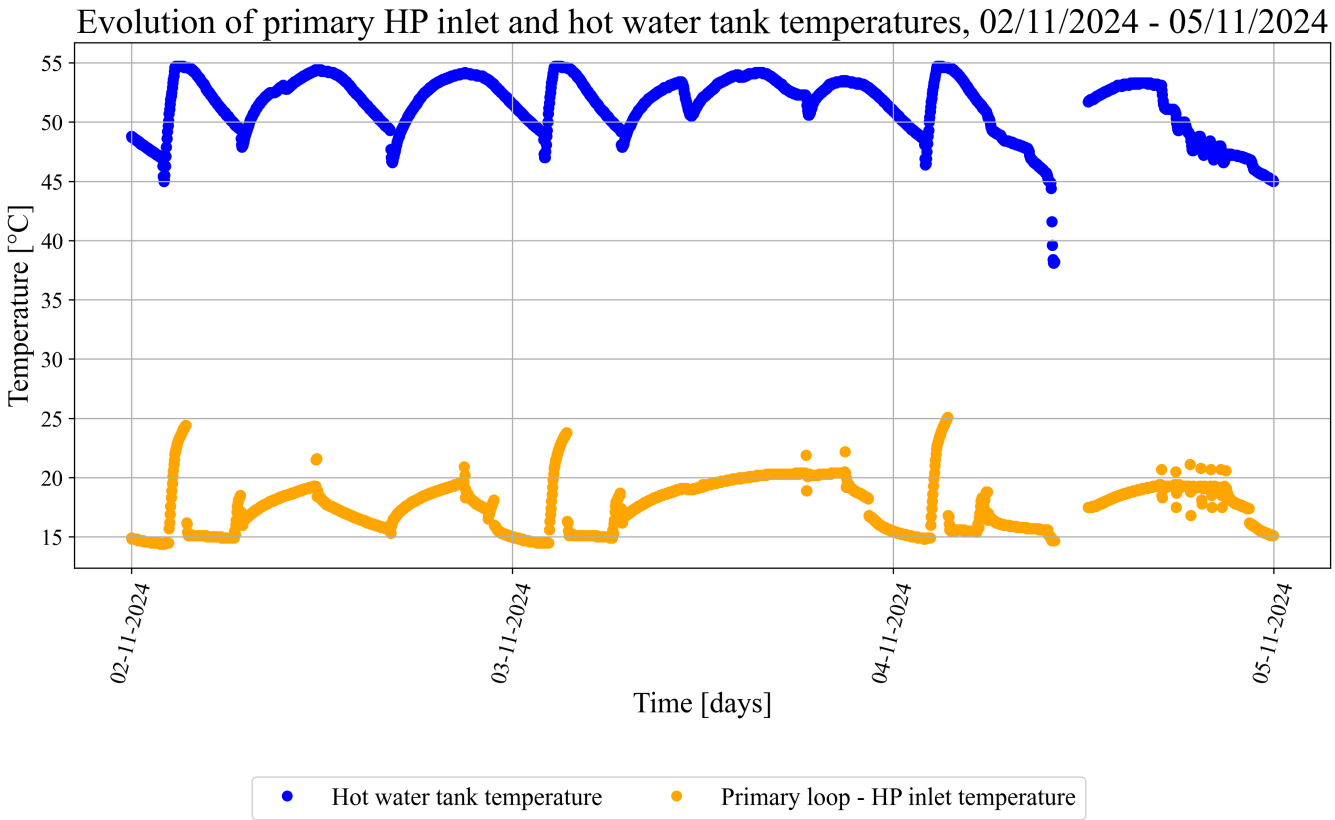

FIGURE 5.3: Temperature evolution in the domestic hot water tank and at the inlet of the Heat Pump (HP) on the primary circuit, from 02/11/2024 to 05/11/2024.

It is also interesting to represent, in a single graph, the evolution of the inlet and outlet temperatures for both the primary and secondary circuits of the heat pump. FIGURE 5.4 displays the daily average temperatures at the inlet and outlet of the heat pump for the primary circuit (i.e., the geothermal loop), as well as for the secondary circuit (i.e., the building loop). The temperatures shown in this FIGURE correspond to daily averages calculated only for the periods when the geothermal heat pump was operating. An exception is made for the period when the aerothermal heat pump was active (represented by the green arrow): during this time, the geothermal heat pump remained off, but the temperature averages for the primary circuit were still computed. This choice was made solely to avoid a visual discontinuity in the curve and to allow a visual comparison of the temperature evolution throughout the entire year. For the secondary circuit, four temperature curves are shown, as the inlet and outlet temperatures differ depending on whether the heat pump is supplying domestic hot water or space heating. Separate averages were therefore calculated for each inlet and outlet temperature in both operating modes. The FIGURE shows a relatively constant temperature difference between the inlet and outlet for both circuits, and the curves generally follow similar trends. During the period when the geothermal heat pump is off (27/06/2024 to 21/11/2024), a small temperature difference is still observed before and after the heat pump's exchanger. However, this difference is minimal and does not correspond to an active free cooling phase. It is likely due to sensor inaccuracies or minor internal heat transfer within the heat pump. As a reminder, the temperature of the primary circuit measured at the heat pump inlet cannot be used to estimate the ground temperature during summer, as it is taken after the natural cooling exchanger, which may influence the temperature reading, and the free cooling periods cannot be determined.

The changes in hourly temperatures follow the same trends as those in daily temperatures and are shown in FIGURE A.18 in APPENDIX A.7.

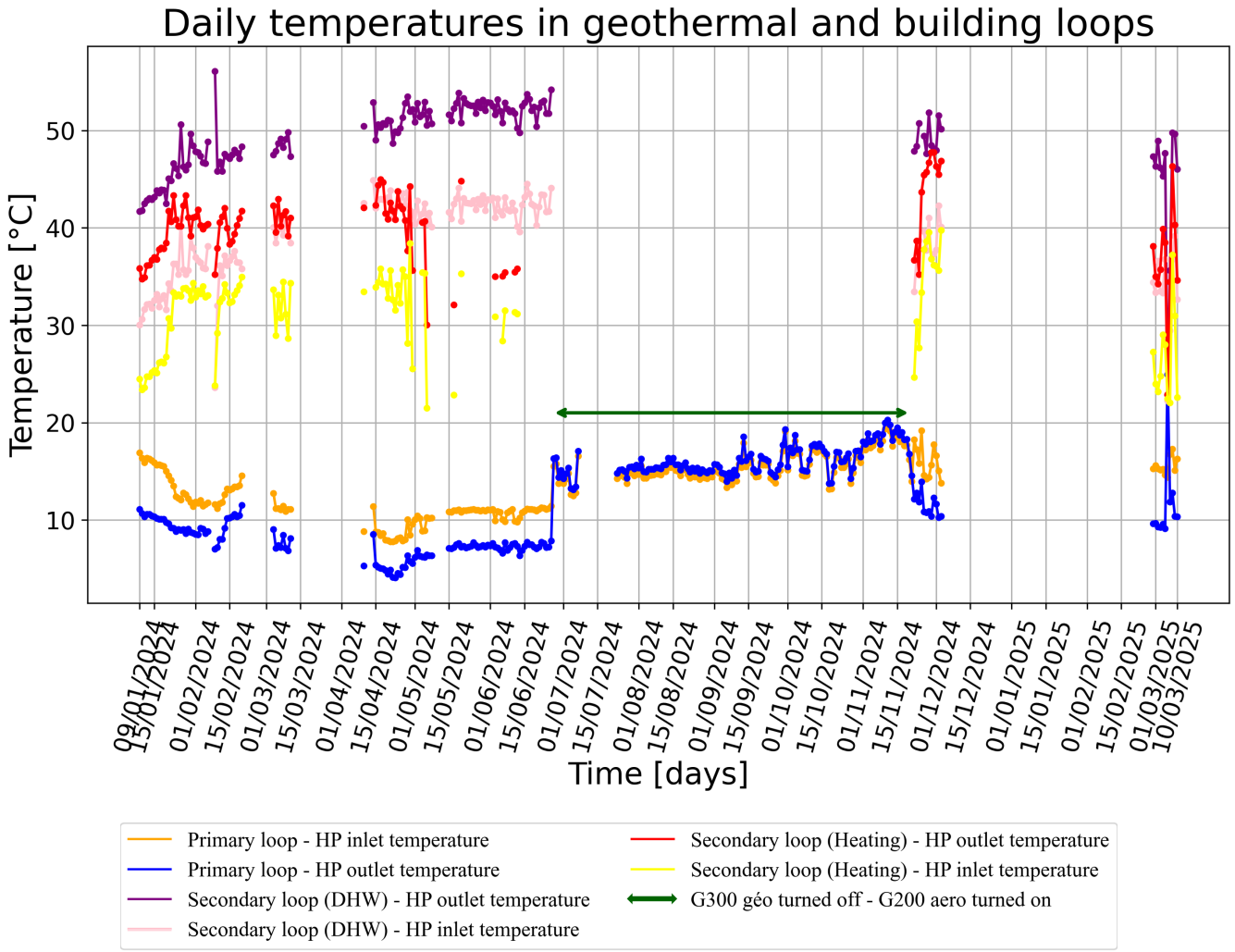

FIGURE 5.4: Daily evolution of heat pump inlet and outlet temperatures for the primary and secondary loops, distinguishing between domestic hot water and heating operation modes.

Calculating the power extracted from underground

Various analyses were conducted to estimate the thermal energy extracted from the ground. In general, the following EQUATIONS are used to calculate the extracted energy:

$$P_{ground} = \rho_f \cdot c_f \cdot \dot{m} \cdot \Delta T \tag{5.1}$$

$$E_{ground} = P_{ground} \cdot t \tag{5.2}$$

where P_{ground} is the extracted ground power in $[W]$, ρ_f is the density of the heat transfer fluid in the geothermal probes $[kg/m^3]$, c_f is the specific heat capacity of the fluid $[J/(kgK)]$, $\dot{m}$ is the volumetric flow rate in $[m^3/s]$, and ΔT is the temperature difference between the inlet and outlet of the heat pump on the primary circuit. In EQUATION 5.2, E_{ground} is the energy extracted from the ground $[Wh]$, and t is the operational time of the heat pump in $[h]$. It should also be noted that as there is also free cooling in summer, E_{ground} is not just the thermal energy extracted from the ground, but also the thermal energy supplied to the ground by the building in summer. Unfortunately, this latter value cannot be calculated due to the

absence of temperature sensors across the free cooling exchanger. By convention, energy extracted from the ground is considered negative, while energy injected into the ground is considered positive. However, in the initial phase of the study, it was not possible to apply EQUATION 5.1 because the flow rate $\dot{m}$ was unknown.

1. **Use of the nominal cooling power**

   Therefore, the first estimates of E_{ground} were obtained using the nominal cooling power of the heat pump. Since the heat pump model is a 300G BWC 301C16, its nominal capacity is 5.84 kW ("Viessmann BE", 2024). Clearly, this value does not represent the actual power extracted from the ground when the heat pump is running, as it is a theoretical value. However, it will give an initial idea.

   The operating time of the heat pump was calculated both hourly and daily. Therefore, E_{ground} was obtained by computing $P_{\text{ground}} \cdot t$. FIGURES 5.5 and 5.6 respectively show the evolution of E_{ground} calculated per hour and per day using the nominal power. These FIGURES clearly show that the extracted energy is limited to a maximum threshold per hour and per day, due to the use of the nominal power, which limits the energy at 5.84 kWh per hour and 140.16 kWh per day. In FIGURE 5.6, a significant drop in extracted energy is observed between 01/04/2024 and 26/06/2024, particularly from 15/04/2024 onwards (corresponding to the green arrow in FIGURE 5.6), compared to the rest of the year. This decrease is explained by the reduced operating time of the heat pump during this period. With rising outdoor temperatures and decreasing heating demand, the geothermal heat pump was used mainly to supply domestic hot water, resulting in much shorter daily runtimes compared to the colder months.

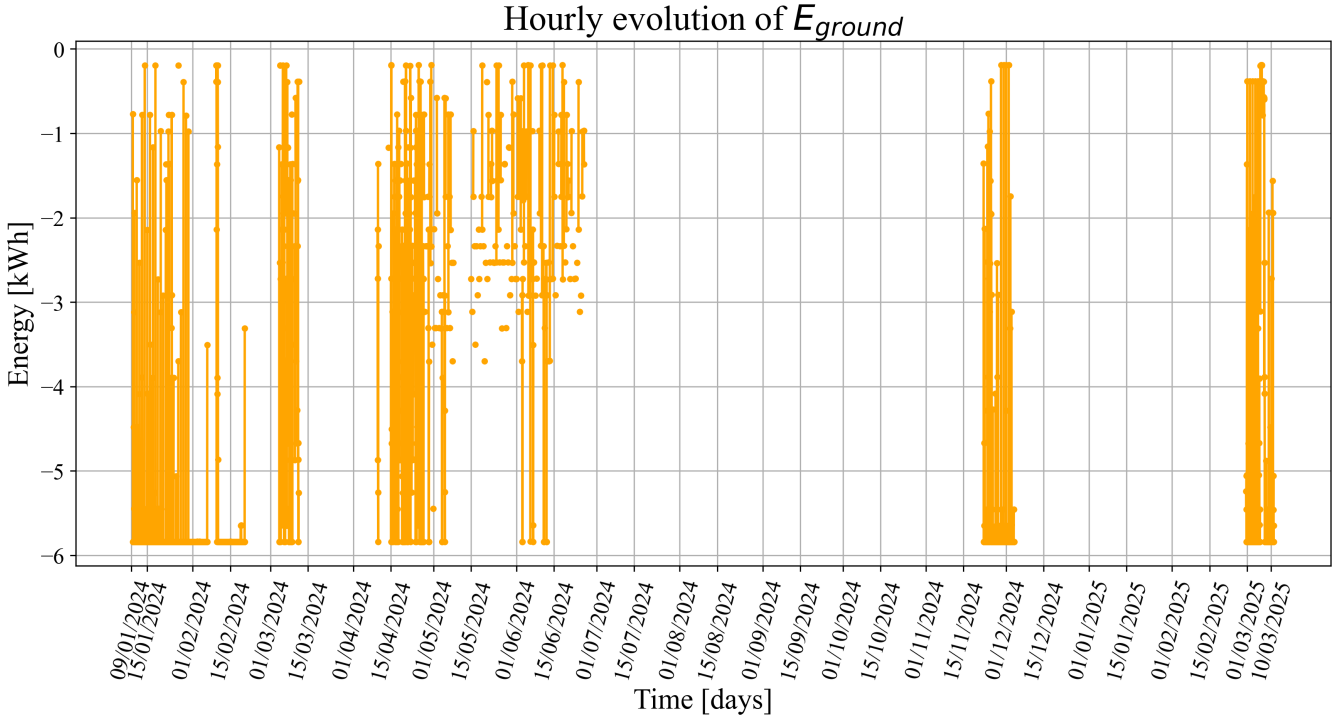

FIGURE 5.5: Hourly evolution of energy extracted from the ground using the nominal power.

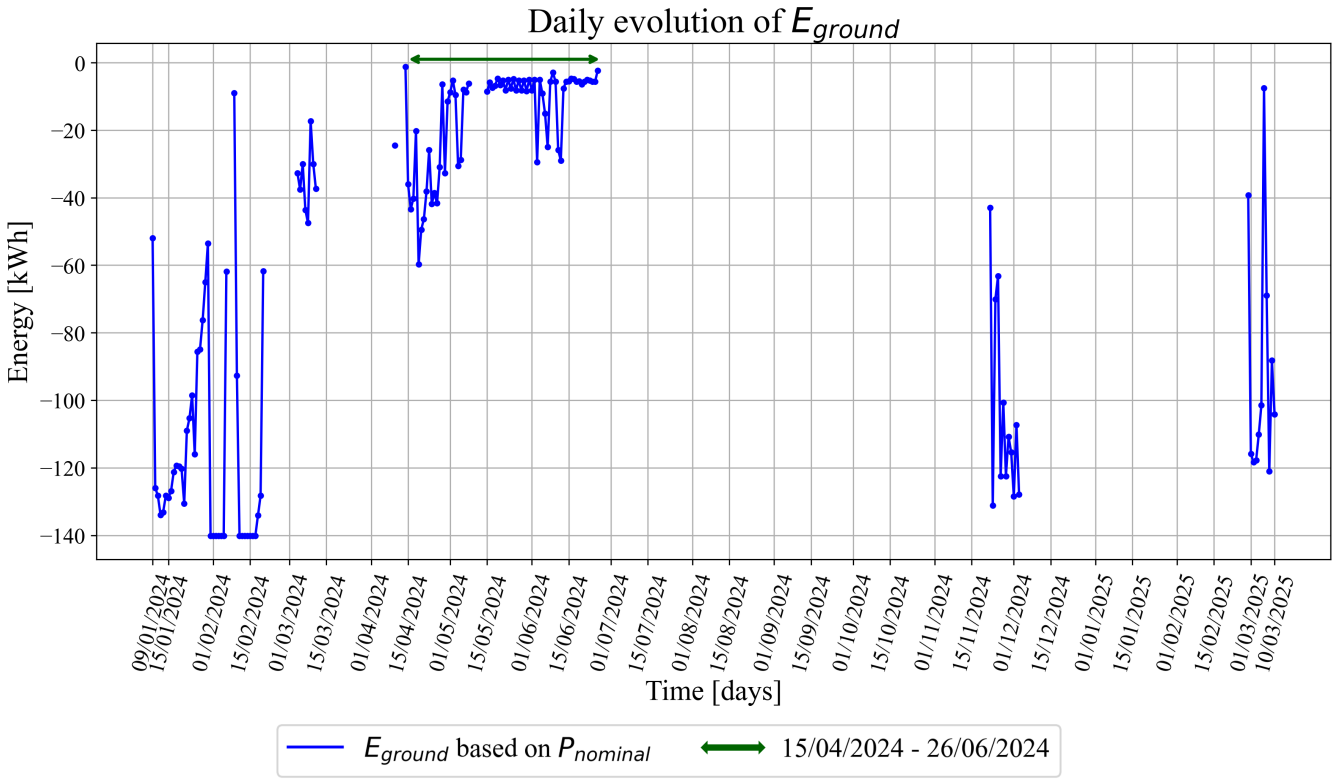

FIGURE 5.6: Daily evolution of energy extracted from the ground using the nominal power.

2. **Use of the EQUATION 5.1 to calculate the power**

   Once the flow rate of the heat transfer fluid in the probes was measured, specifically at the heat exchanger level in the heat pump, it became possible to use EQUATIONS 5.1 and 5.2 to better estimate the energy extracted, taking into account variations in building demand. The parameter values used are those discussed in SECTION 4.2.

   For comparison purposes, E_{ground} was calculated using two different methods:

   - In the first method, ΔT is based on the average hourly or daily temperature difference when the heat pump is on. This temperature difference is then multiplied by the relevant parameters (ρ_f, c_f, $\dot{m}$), and by the total heat pump operating time per hour or per day, depending on the desired output.
   - In the second method, energy is calculated for each individual time step. In other words, for every time step when the compressor is on, the instantaneous temperature difference is multiplied by the parameters and the time interval between two successive data points. The extracted energy is then summed hourly or daily.

FIGURE 5.7 compares the daily evolution of E_{ground} calculated using the three methods. As a reminder, the three methods compared here are: the use of the nominal power, the application of EQUATION 5.2 using the average daily temperature, and the application of the same equation at each time step. First, the

FIGURE shows that both methods based on EQUATION 5.2 provide almost identical results, meaning that the choice of temporal resolution has little impact on the final energy estimation. Secondly, the extracted energy is no longer limited by a fixed threshold as in the nominal method. However, the results obtained with the temperature-based methods reveal energy values that appear unrealistic, especially outside the period from 15/04/2024 to 26/06/2024. For example, values up to 600 kWh per day are reached, which would require a constant thermal power of 25 kW over 24 hours, more than four times the nominal capacity of the geothermal heat pump, which is 5.84 kW. While this nominal value is theoretical and may not reflect the exact operational maximum, such a discrepancy remains physically implausible. At this stage, no clear explanation has been identified to account for these overestimations. Further investigation would be necessary to verify the validity of the measurements.

Similar trends are observed in the hourly energy evolution presented in FIGURE A.19 in APPENDIX A.8.

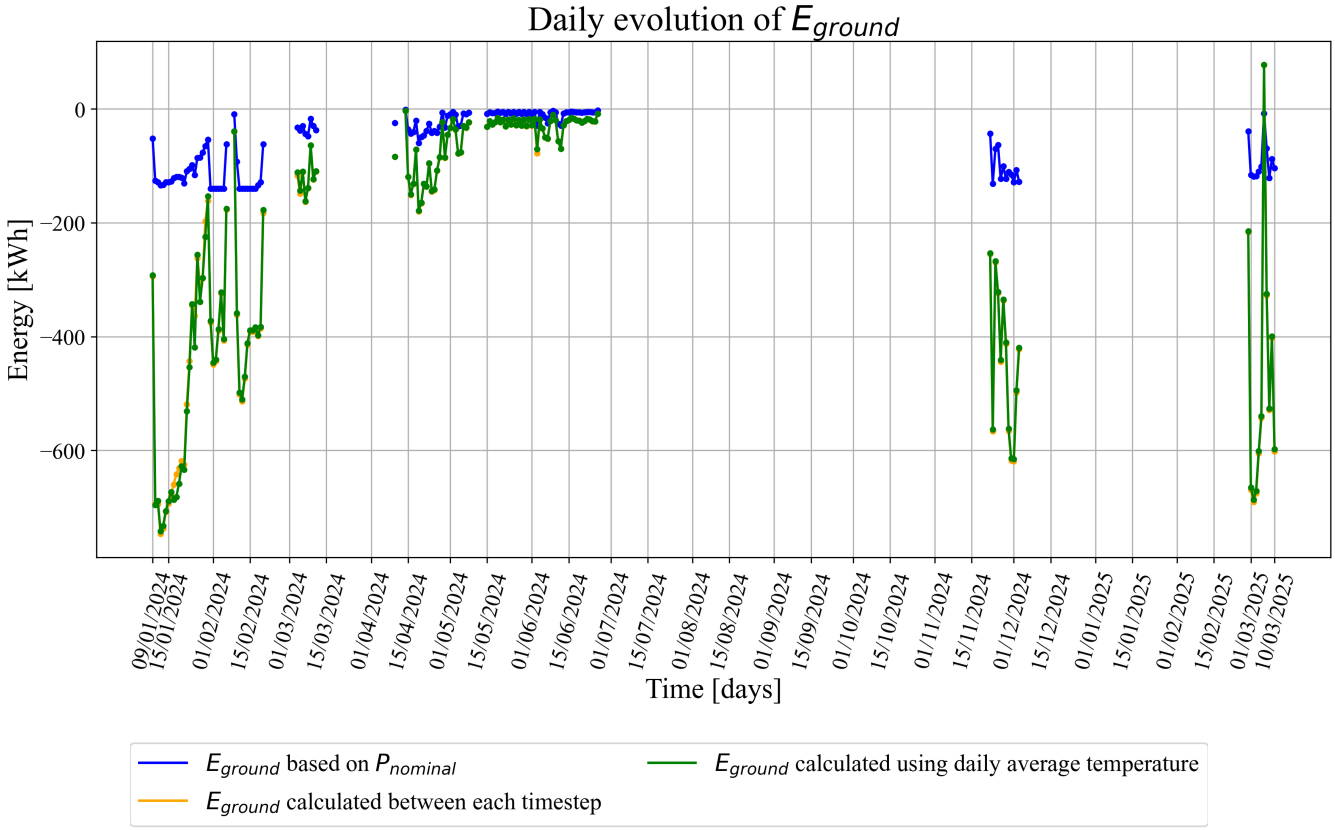

FIGURE 5.7: Comparison of daily extracted ground energy using three different calculation methods.

5.2 Dataset 2

5.2.1 Description

This dataset was hardly used and will therefore only be briefly described. It contains information from 13/08/2024 to 11/04/2025. However, some periods are missing, such as from 04/12/2024 to 28/02/2025. There are four interesting types of information in this dataset. First, the timestamps indicating when each measurement was taken, with data recorded every 15 minutes. Secondly, it includes the electrical power

consumed by the heat pump and the thermal power delivered to the secondary circuit. Finally, it also contains information on the volumetric flow rate in the secondary circuit.

5.2.2 Analysis

The power data are the most relevant and were first used. A heat pump does not generate energy, it transfers heat. According to the efficiency principle of a heat pump, as described by EQUATION 2.3, the following relation can be written:

$$P_{heating} = P_{ground} + P_{elec} \tag{5.3}$$

where $P_{heating}$ is the power delivered to the secondary circuit, and P_{elec} is the electrical power supplied to the heat pump.

However, internal losses, whether electrical, mechanical, or thermal, cause the equality in EQUATION 5.3 to be unequal. Therefore, a factor η is introduced to represent the internal efficiency of the heat pump, and the equation becomes:

$$P_{heating} = \eta \cdot (P_{ground} + P_{elec}) \tag{5.4}$$

$$\Leftrightarrow P_{ground} = \frac{P_{heating}}{\eta} - P_{elec} \tag{5.5}$$

This internal efficiency factor is quite high and is assumed here to be 0.95.

EQUATION 5.5 can also be expressed in terms of energy:

$$E_{\text{ground}} = \frac{E_{\text{heating}}}{\eta} - E_{\text{elec}} \tag{5.6}$$

The electrical and thermal power data from this dataset were thus used to compute the extracted ground power in an alternative way. However, since the datasets do not correspond to the same time period and until 21/11/2024 no power is extracted from the subsurface, due to the system operating in cooling mode, the calculation was only made from 22/11/2024 to 03/12/2024. FIGURE 5.8 presents a comparison of the extracted ground energy calculated using four different methods. It shows that when E_{ground} is calculated using EQUATION 5.6 (based on $E_{heating}$), the resulting daily extracted energy is lower than the one obtained with EQUATION 5.2, but it follows the same trend. However, it is higher than the energy calculated using the nominal power method and does not necessarily follow the same trend. This is the only result obtained from this second dataset.

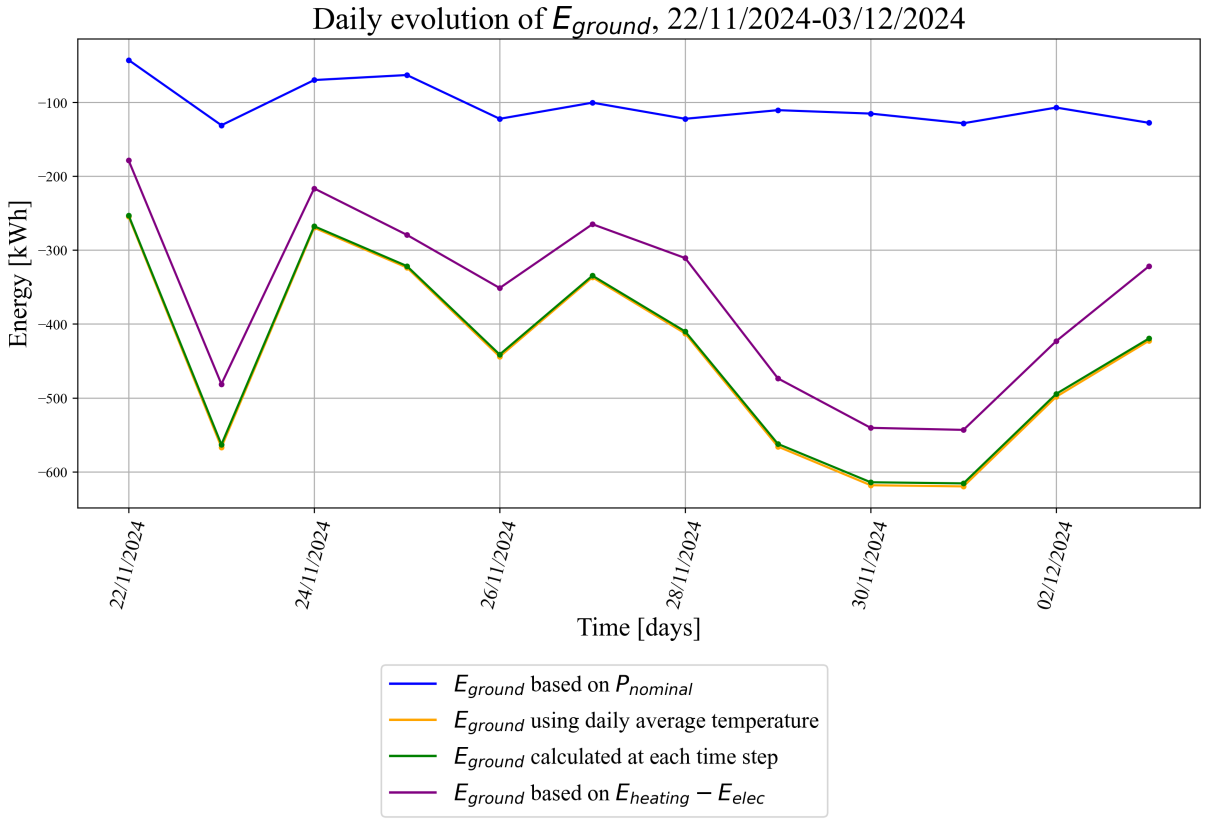

FIGURE 5.8: Comparison of daily ground energy extracted using four different calculation methods.

Chapter 6

Calibration

Following the analysis of the dataset and the determination of the thermal loads, it is possible to use the analytical model to compute the evolution of ground temperature based on these thermal loads and to compare it with the monitored data. The aim of this CHAPTER is to calibrate the various parameters that influence the model, so that the simulated temperatures closely match those observed in the monitoring data.

To ensure the comparison is as relevant as possible, the modelled temperature will primarily be observed at a single point, the centre of the central borehole (FIGURE 6.1). It is therefore the modelled fluid temperature (EQUATION 4.8) that will be compared to the monitored fluid temperature. In the monitoring data, this fluid temperature is not measured directly ($T_{fluid,mon}$). Instead, it is approximated by taking the mean of the temperatures monitored at the inlet and outlet of the heat pump on the geothermal side:

$$T_{fluid,mon} = \frac{T_{fluid,mon_{in}} + T_{fluid,mon_{out}}}{2}$$

This value will be used as the reference temperature for model calibration.

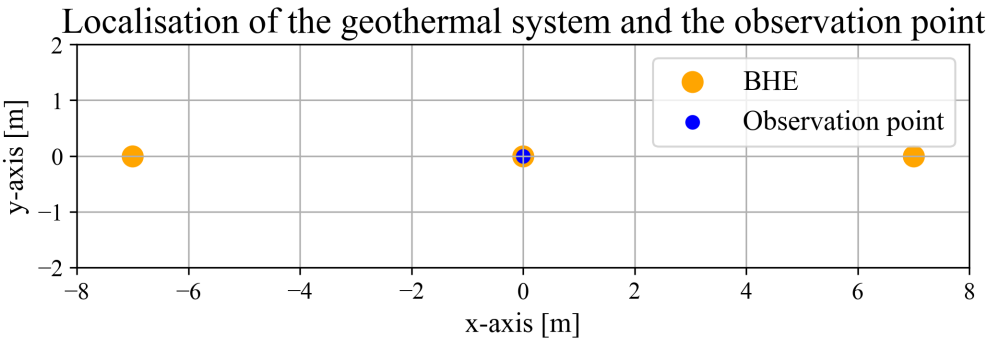

FIGURE 6.1: Localisation of the geothermal system and the observation point with an observation point at the centre of the central borehole, used for model-data comparison.

6.1 Thermal load

As explained in CHAPTER 5, the energy extracted from the ground (E_{ground}) was calculated using different methods. As a result, four thermal load scenarios were considered over the study period to model the evolution of the fluid temperature. The impact of the thermal load on the simulated temperature is illustrated

in FIGURE 6.2. At this stage, the model was run using the default (non-calibrated) input parameters presented in SECTION 4.2, with the daily values of E_{ground} as thermal load. These values were selected to provide a preliminary estimate of the model's response to the imposed thermal loads. The calibration of the model parameters is presented in the following SECTIONS.

Temperatures were calculated over the entire duration of the first dataset. A zero thermal load is imposed when no data was monitored or when the geothermal heat pump was turned off in favour of the aerothermal heat pump. As expected, the temperatures calculated by the model vary depending on the applied thermal load. Indeed, there is a correlation between FIGURE 5.7 and FIGURE 6.2, where a high extracted energy corresponds to a lower calculated fluid temperature, and vice versa.

The daily extracted energy calculated from the average ΔT and the energy computed at each time step are almost identical. As a result, the green and purple curves in FIGURE 6.2 are nearly indistinguishable (the difference is almost imperceptible to the naked eye, and the purple curve is almost entirely hidden under the red curve, as explained below). On the other hand, the results differ significantly between the blue curve (T_{fluid} modelled when E_{ground} is based on $P_{nominal}$), and the green and purple curves. This result is consistent with the difference between the blue curve and the green and orange curves of the FIGURE 5.7. The red curve on the FIGURE 6.2 is based on a combination of thermal loads. The thermal load used for the purple curve is applied from the beginning of the dataset until 21/11/2024, as it is considered the most accurate. From 22/11/2024 to 03/12/2024 (brown arrow in FIGURE 6.2), the thermal load is based on the energy delivered to the secondary circuit ($E_{heating}$). Finally, from 04/12/2024 to 10/03/2025, the thermal load from the purple curve is again used. The red curve therefore almost entirely overlaps the purple one and is almost identical to the green curve, except for the period marked by the brown arrow.

The model shows little correspondence with the monitored temperatures. Only a period of about seventy days starting around the 100th day appears to match the monitored data in the FIGURE 6.2 below. Using the nominal power to compute E_{ground} seems to be a good approach when initial parameters are applied, although this method remains more theoretical (blue curve). Indeed, it is the one that comes closest to the monitored temperatures (orange curve) over those 70 days.

For the other periods, the calculated temperatures deviate significantly from the monitored ones. In addition to not matching the values, even the overall trends are different. FIGURE 6.3 focuses on the first 63 days of the purple curve of FIGURE 6.2 to better illustrate the deviation in trend (corresponding to the dark blue arrow in FIGURE 6.2). This FIGURE 6.3 clearly shows that the trends are not the same, and the concavity of the curves even differs at certain points. Substantial discrepancies between calculated and monitored temperatures are also observed from 22/11/2024 to 03/12/2024 (brown arrow) and from 28/02/2025 to 10/03/2025 (end of the graph).

Using $P_{heating}$ and P_{elec} to estimate P_{ground} does not appear to improve the results either, as shown by the red curve on FIGURE 6.2, where the calculated temperatures remain far from the monitored ones and continue to follow different trends during the period indicated by the brown arrow.

For the rest of the study, the thermal load based on E_{ground} calculated at each time step was chosen, as it provides the most consistent and realistic estimates. It was decided to focus only on the data from 15/04/2024 to 26/06/2024 (corresponding to the dark purple arrow in FIGURE 6.2), as this period seemed to provide the most realistic results. Indeed, a change in system parameters likely occurred between the

beginning of the monitoring and a date around 15/04/2024. This change could be, for example, a variation in flow rate. Furthermore, as shown by the orange curve in FIGURE 5.2, this period contains fewer large hourly temperature variations, which are more plausible and could be explained by a reduced impact of secondary circuit temperature interference on the measurements.

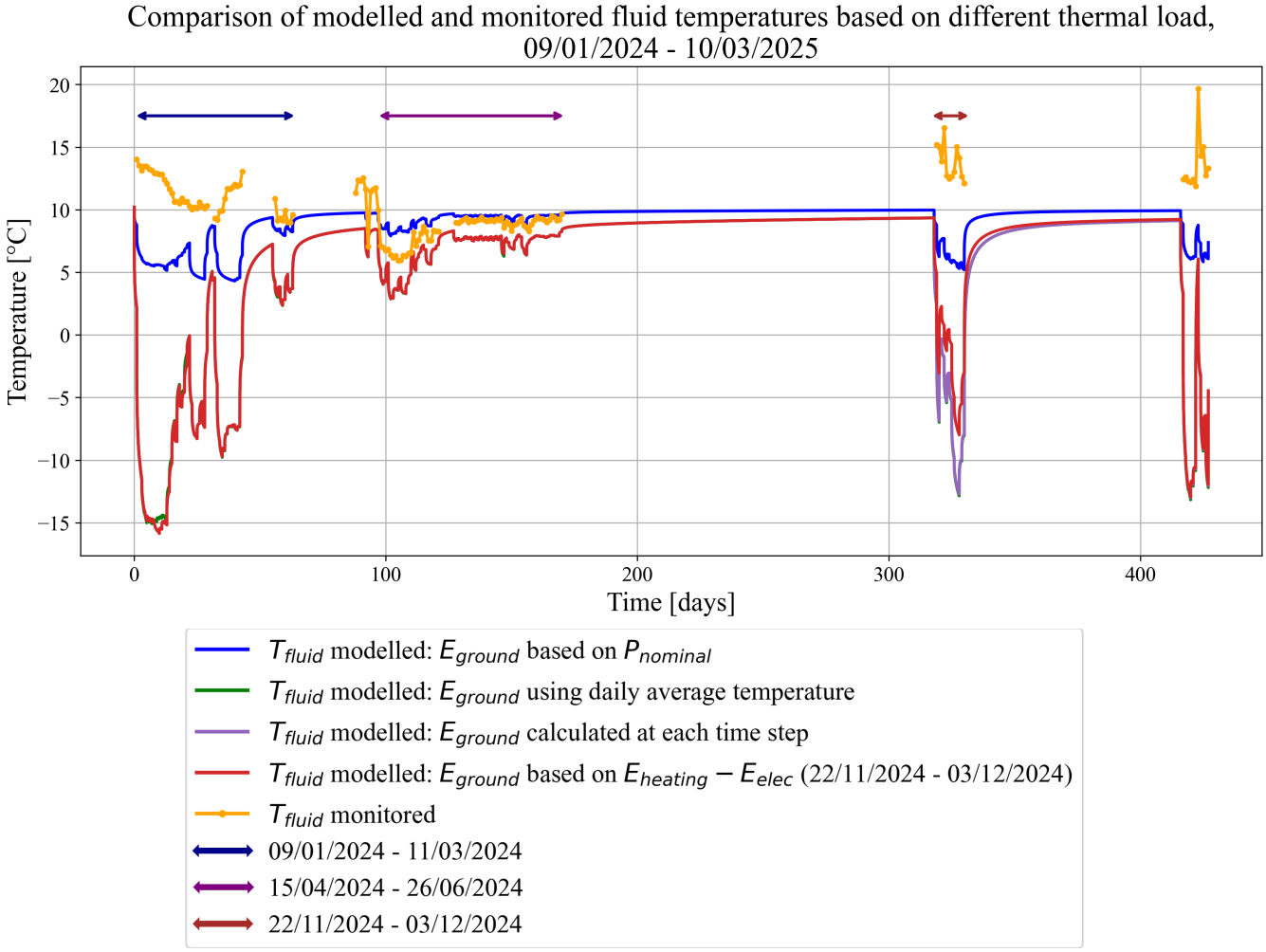

FIGURE 6.2: Comparison between the modelled and monitored fluid temperature evolution when E_{ground} is computed with the four different methods.

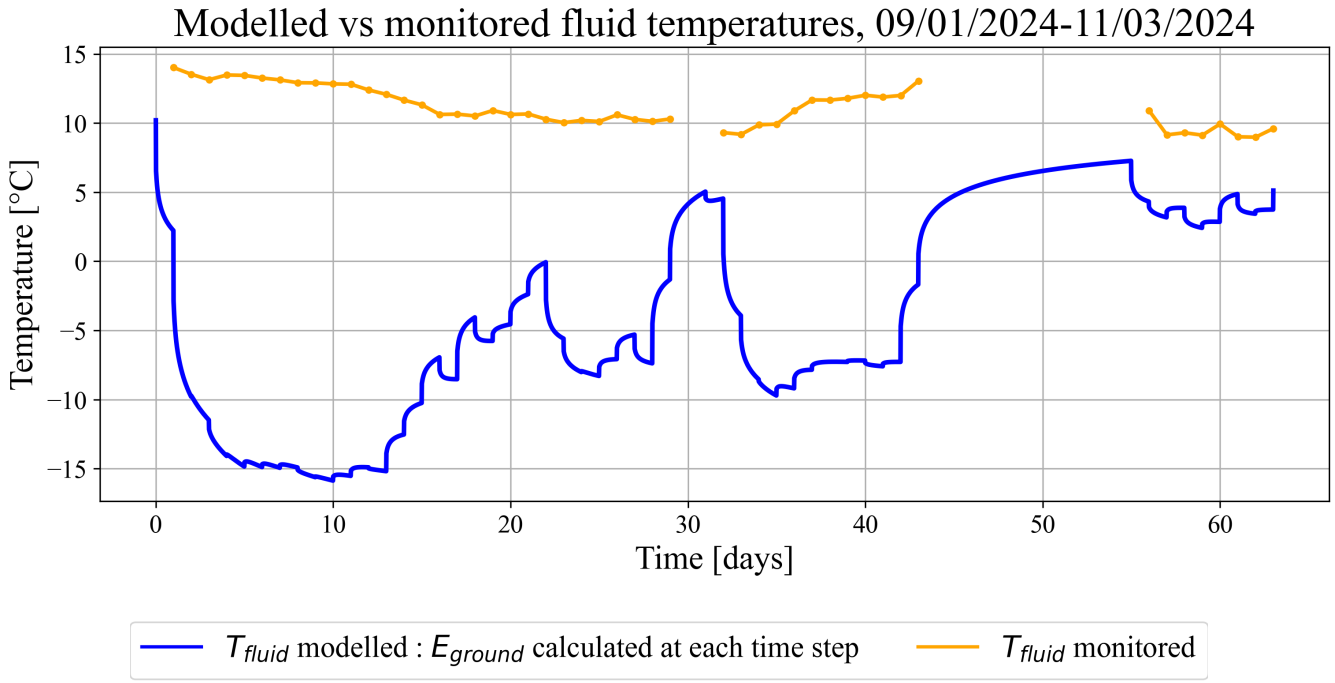

FIGURE 6.3: Comparison between the modelled and monitored fluid temperature evolution when E_{ground} is computed at each time step and summed daily, for the period from 09/01/2024 to 11/03/2024 (corresponding to the dark blue arrow in FIGURE 6.2).

6.2 Initial ground temperature

The ground temperature defined in SECTION 4.2 is unlikely to correspond to the actual initial ground temperature at the beginning of the calibration period. Indeed, since the analysed period starts on 15/04/2024, and not at the beginning of the geothermal system's operation, the ground has already been subjected to a certain thermal load, which has impacted its temperature. In addition, the initial temperature used previously was a theoretical estimate. A better approximation of the real ground temperature on 15/04/2024 is therefore determined in this SECTION 6.2. This temperature may be close to the real initial undisturbed ground temperature.

Naturally, starting the calibration process with the initial ground temperature will influence the calibration of the other parameters. However, as shown in FIGURE 6.2, the temperature evolution simulated by the model using ground energy extracted calculated at each time step tends to underestimate the monitored temperature. Therefore, it is acceptable to perform this calibration first in order to shift the curve upwards and obtain more realistic values for the other parameters. The ideal calibration process would involve varying all parameters simultaneously and performing a global sensitivity analysis to determine the best combination of values. Unfortunately, such an approach is out of the scope of this study.

6.2.1 Daily thermal loads

FIGURE 6.4 shows the evolution of the monitored and modelled fluid temperatures for different assumed values of the initial ground temperature. For each tested value of T_0, the Root Mean Square Error (RMSE) between the modelled and measured temperature evolutions was calculated. The results are summarized

in TABLE 6.1, which shows that an initial ground temperature of 10.5 °C provides the best overall fit, as it yields the lowest RMSE. This temperature is quite close to the temperature initially estimated.

TABLE 6.1 shows that other temperatures, such as 10.4 °C and 10.6 °C, also lead to relatively low RMSE values. This is confirmed visually in FIGURE 6.5, which shows that a value of $T_0 = 10.4$ °C provides a good match with the monitored temperature curve. In particular, the variations observed between day 30 and day 58 are well reproduced, the modelled peaks align closely with those observed in the monitoring data. Despite this good visual agreement, especially after day 30, the RMSE is slightly higher than for $T_0 = 10.5$ °C. This is due to larger differences between modelled and monitored temperatures during the early part of the simulation (mainly before day 10), which have a stronger impact on the RMSE, as this method gives more weight to large errors. Therefore, the higher RMSE associated with $T_0 = 10.4$ °C reflects early mismatches, even though the later temperature evolution is well reproduced. Given the relatively small difference in RMSE (0.013 °C) and the inherent uncertainty in the monitoring data, a 0.1 °C difference in initial temperature is not considered meaningful. Nevertheless, $T_0 = 10.5$ °C is retained as the optimal value.

FIGURE 6.4 shows that the initial ground temperature (T_0) affects the response of the model. Increasing T_0 results in a general upward shift of the simulated temperature curve. It is important to note that the amplitude of the temperature variations is not affected by the value of T_0. This parameter only shifts the baseline around which the thermal fluctuations occur. When $T_0 = 10.2$ °C, the simulated ground temperature is mainly underestimated compared to the monitored values. Conversely, higher temperatures lead to an overestimation. Although several values of T_0 were tested and their corresponding RMSEs are listed in TABLE 6.1, only the curves for the initial and calibrated values are shown in FIGURE 6.4 to avoid overloading the FIGURE and ensure visual clarity.

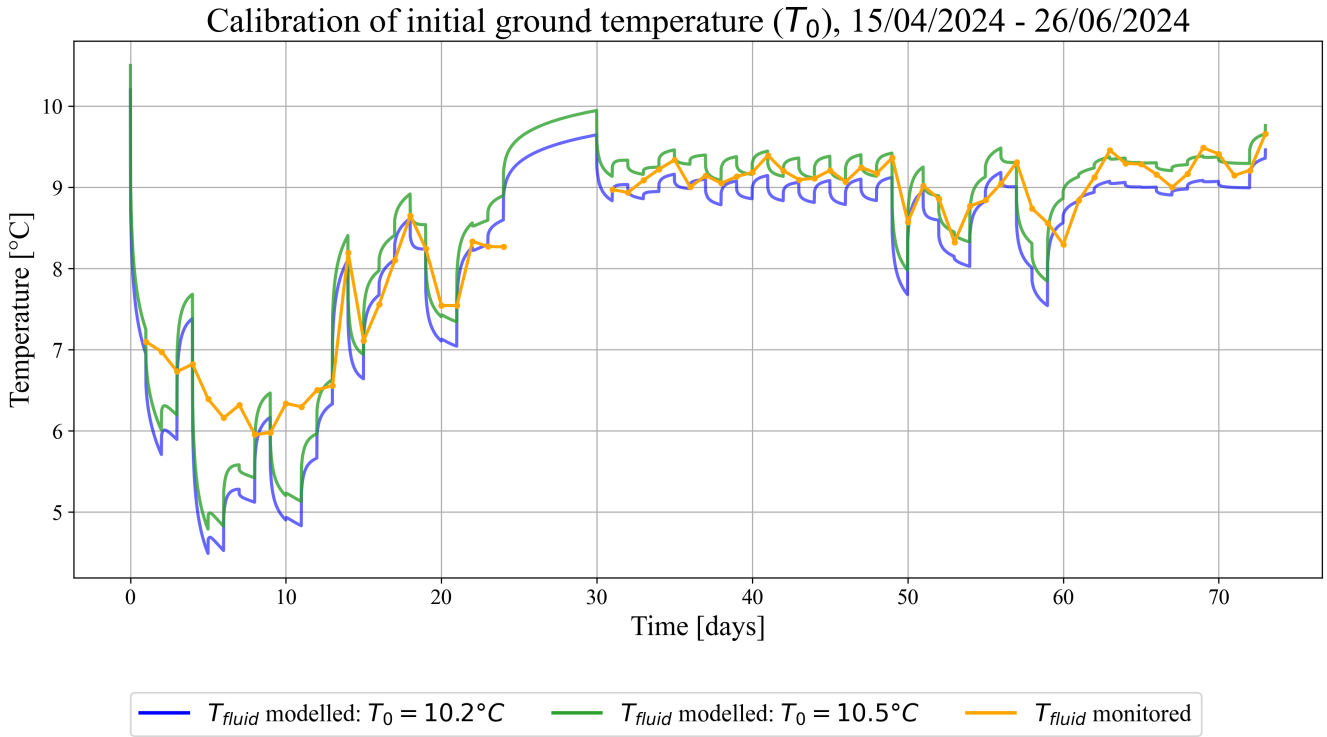

FIGURE 6.4: Comparison between modelled and monitored fluid temperature evolution for different values of the initial ground temperature T_0.

TABLE 6.1: RMSE between modelled and monitored fluid temperature for different initial ground temperatures T_0.

Initial ground temperature T_0 [°C]	**RMSE** [°C]
10.0	0.658
10.1	0.585
10.2	0.521
10.3	0.470
10.4	0.436
10.5	0.423
10.6	0.434
10.7	0.466

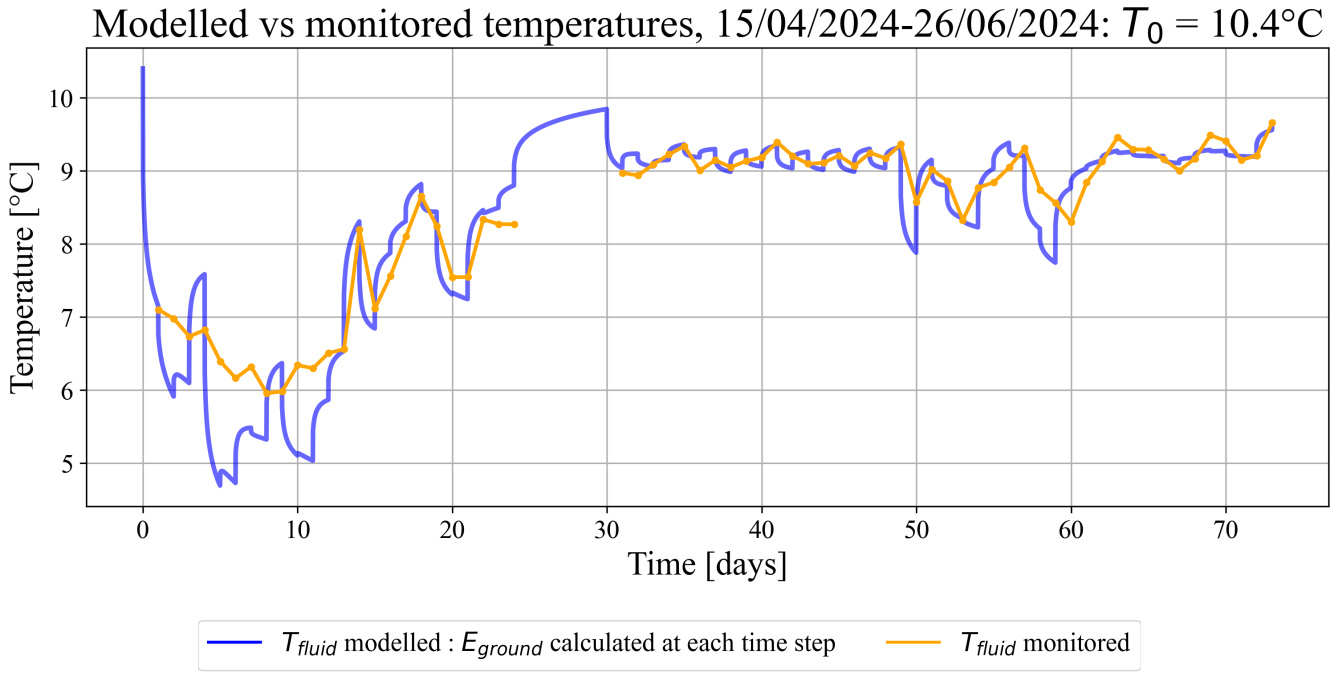

FIGURE 6.5: Comparison between the modelled and monitored fluid temperature evolution when the initial ground temperature T_0 is 10.4 °C.

6.2.2 Hourly thermal loads

When the hourly thermal loads are used in modelling, no detailed calibration of the initial ground temperature was carried out. The evolution of the ground temperature simulated using hourly thermal loads is based on the same parameters as those obtained from the calibration using daily thermal loads, i.e. an initial ground temperature of 10.5 °C. The objective here is simply to visualize the temperature response over time and to examine the associated RMSE.

FIGURE 6.6 shows that using hourly thermal loads in the model leads to greater fluctuations in the simulated fluid temperature compared to the results obtained with daily thermal loads. Moreover, these fluctuations are also more pronounced than those observed in the monitored fluid temperatures. The model

appears to reproduce upper temperature peaks more accurately than the lower ones, which tend to be underestimated. These large variations indicate that the modelled system has limited thermal inertia and struggles to replicate the short-term thermal dynamics observed in reality. This limitation arises from the way the borehole heat exchanger is represented in the model: the thermal behaviour of the probe is described by a single parameter, the fluid-to-ground thermal resistance R_b (see EQUATION 4.8), which assumes that a steady-state regime is established at the level of the probe. As a result, the model does not account for the transient thermal capacity of the borehole itself, such as the thermal inertia of the grout and pipes. This simplification prevents the model from accurately reproducing the short-term thermal response of the system, particularly in response to rapid load fluctuations, which can lead to an overestimation of temperature variations at short time scales.

The RMSE obtained in this case is higher, reflecting a greater difference between monitored and simulated values compared to the daily thermal load case. For an initial ground temperature of 10.5 °C, the RMSE is 2.613 °C. This value is particularly influenced by the first ten days (from 15/04/2024 to 25/04/2024), during which the temperature variations are more meaningful. It is also important to note that out of the 1752 hourly time steps in the calibration period, the heat pump was active during only 374 of them. This reduces the number of relevant data available to calculate the RMSE, and partially explains the degraded performance of the model in this configuration.

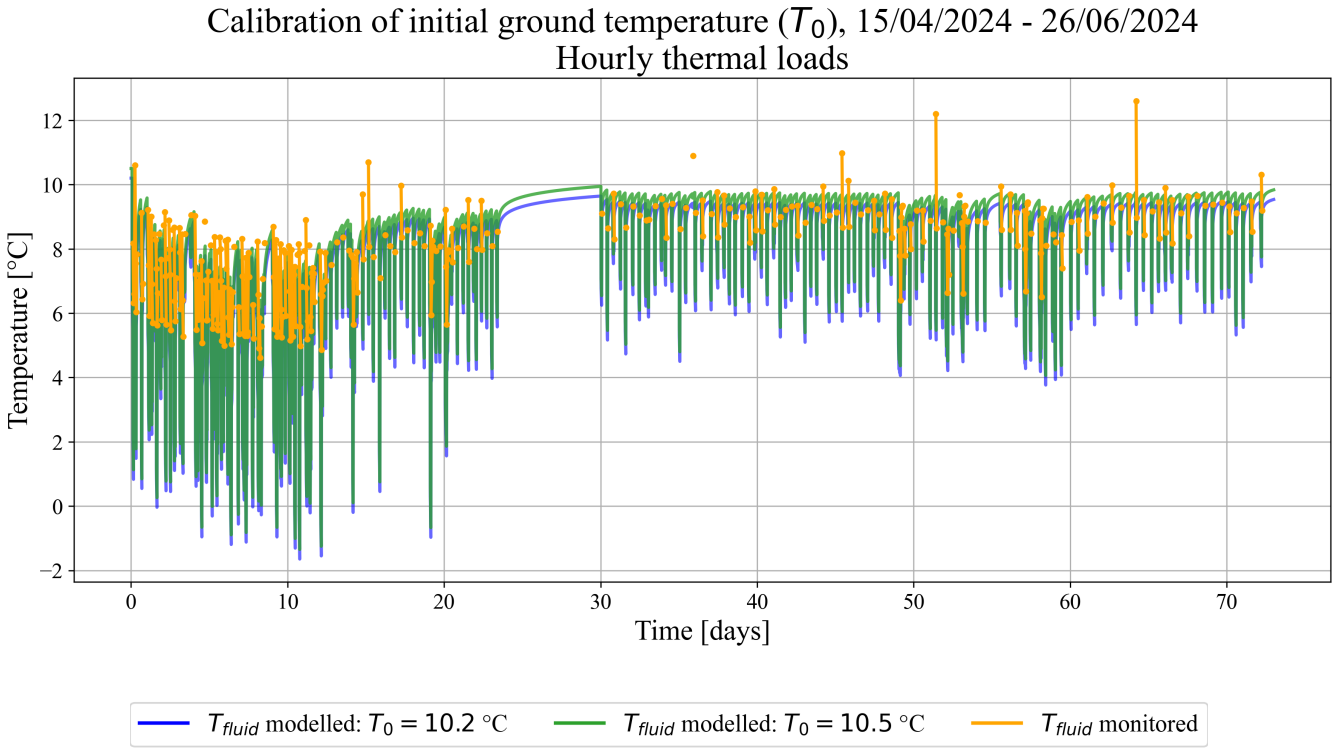

FIGURE 6.6: Comparison between modelled and monitored fluid temperature evolution for different values of the initial ground temperature T_0, using hourly thermal loads.

6.3 Thermal conductivity

As explained in SECTION 2.4.1, thermal conductivity is an important parameter in the heat transfer equation within the subsurface, and therefore influences the evolution of temperature around the boreholes. As

mentioned in SECTION 4.2, an initial conductivity value of 2.3 W/(mK) was chosen to reflect the lithologies encountered, based in particular on the drilling report data. However, this thermal conductivity is only an estimate, and the actual value may deviate considerably from it. Several conductivity values will thus be tested to identify the one that provides the best fit between the modelled and monitored temperatures over the period from 15/04/2024 to 26/06/2024. This calibration is carried out assuming the calibrated initial ground temperature of 10.5 °C.

6.3.1 Daily thermal loads

FIGURE 6.7 and TABLE 6.2 show that the initial estimate of 2.3 W/(mK) was relatively close to the thermal conductivity value that best matches the underground behaviour. Indeed, thermal conductivities of 2.4 W/(mK) and 2.5 W/(mK) are equal and yield the lowest RMSE values. The conductivity of 2.4 W/(mK) is selected as it is closer to the initially imposed value. Moreover, the visual results are again very similar, and the simulation with a conductivity of 2.4 W/(mK) shows a better match with the monitoring data after day 10 than with 2.5 W/(mK), which tends to reduce the large differences observed at the beginning but at the expense of a less accurate fit after day 10. It is important to note that this value represents the average thermal conductivity of the ground. The model does not allow for variations in conductivity with depth based on the different lithologies encountered. Therefore, the value of 2.4 W/(mK) is considered to be the representative thermal conductivity of the underground at the RDI site. This remains a reasonable estimate given the range of values presented in TABLE 2.2.

In FIGURE 6.7, the blue curve corresponds to the most optimized model from SECTION 6.2, that is, with the initial parameters and the calibrated initial ground temperature. The model provides a temperature evolution that is generally close to the monitored temperature. From day 10 onwards (i.e., 25/04/2024), the model follows the same general trend as the monitored fluid temperatures, although the simulated values remain slightly offset. The best correspondence is observed from day 60 onwards. Between days 23 and 30, the model simulates a sharp rise in fluid temperature. This corresponds to a period when the heat pump was turned off, so no measurements are available to validate the model at that time. Nevertheless, this moment would have been interesting to assess how the model performs during periods without thermal load. In fact, the model suggests that the fluid temperature tends to return toward the initial ground temperature value when the system is inactive. An increase of the thermal conductivity will slightly decrease the amplitude of the variations and shift the curve.

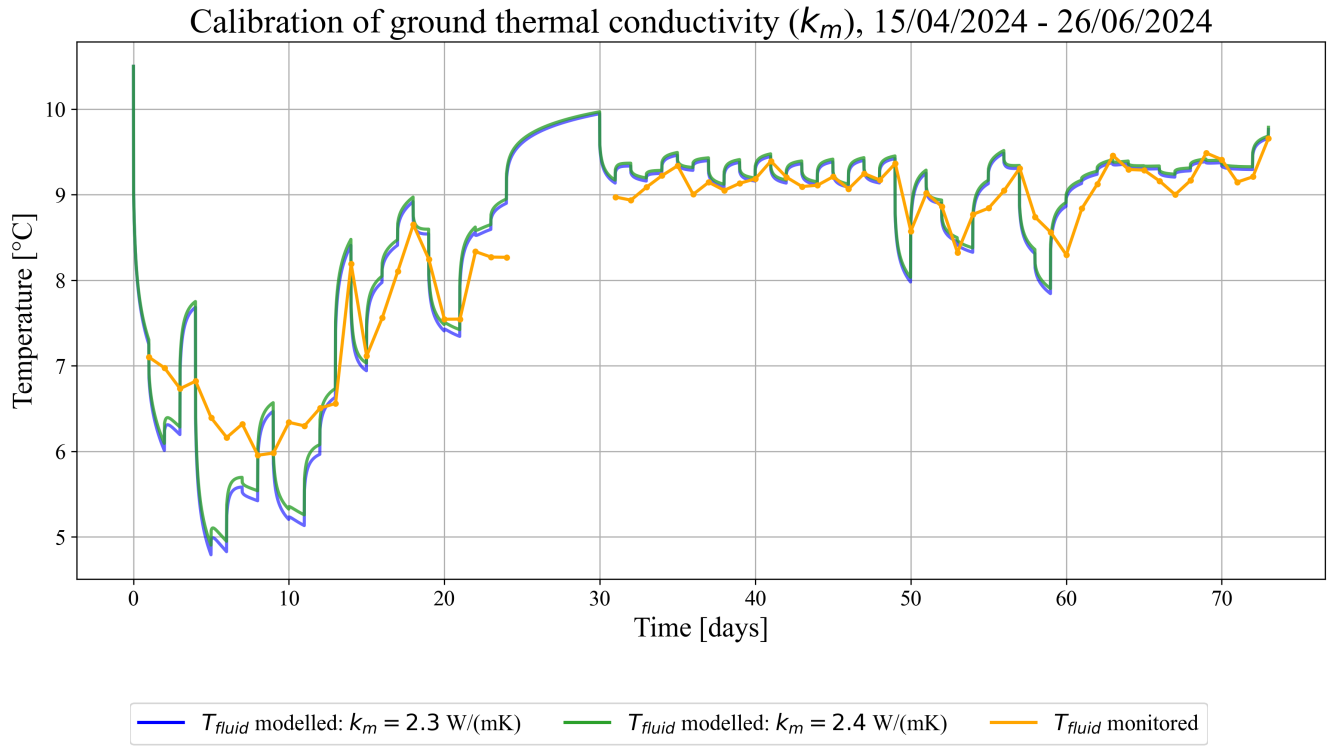

FIGURE 6.7: Comparison between modelled and monitored ground temperature evolution for different values of the thermal conductivity k_m.

TABLE 6.2: RMSE between modelled and monitored ground temperature for different values of ground thermal conductivity k_m.

Ground thermal conductivity k_m [W/mK]	**RMSE** [°C]
2.0	0.516
2.1	0.473
2.2	0.443
2.3	0.423
2.4	0.415
2.5	0.415
2.6	0.420
2.7	0.429
2.8	0.445

6.3.2 Hourly thermal loads

FIGURE 6.8 shows the evolution of the modelled fluid temperature between 15/04/2024 and 26/06/2024, using hourly thermal loads. Two thermal conductivity values are tested, one corresponding to the initial parameter set, and the other one to the optimised thermal conductivity identified in SECTION 6.3.1. As observed previously in FIGURE 6.7, the model responses for both thermal conductivities are very similar. The RMSE decreases only from 2.613 °C to 2.576 °C, when the optimised value is used.

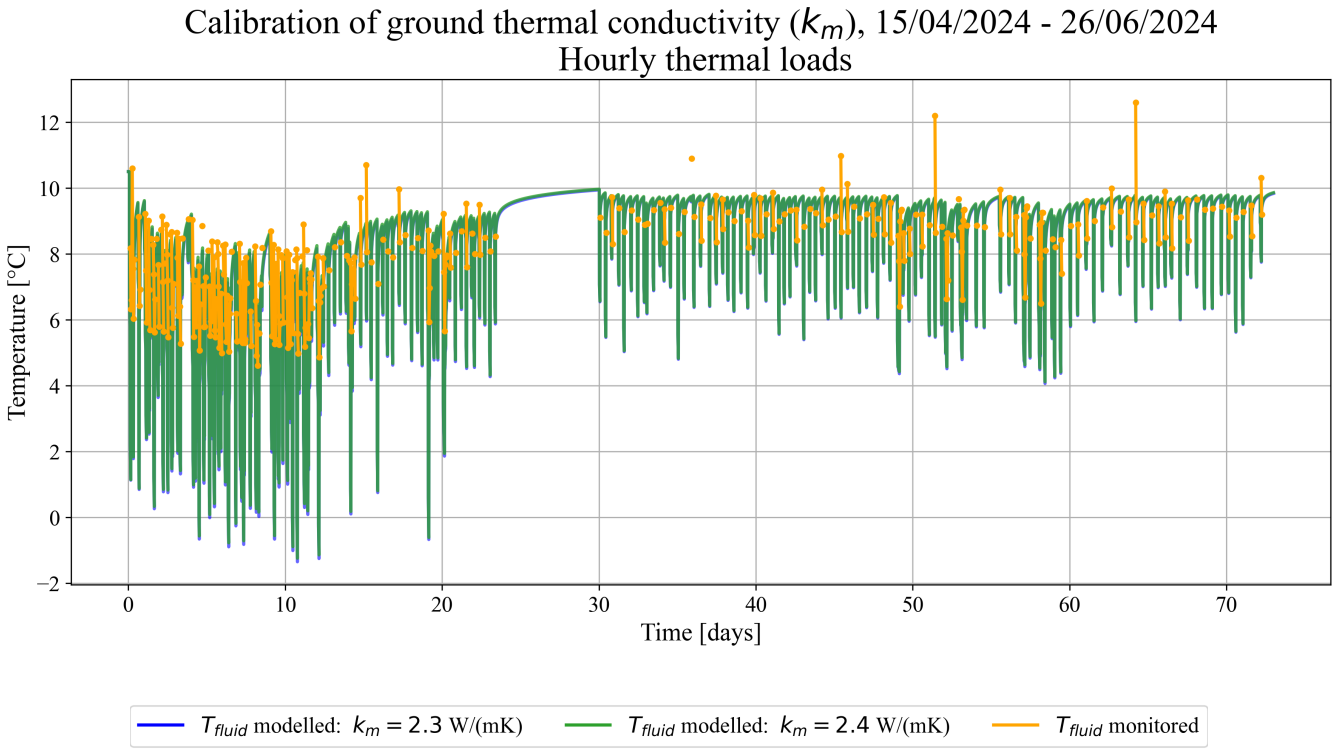

FIGURE 6.8: Comparison between modelled and monitored fluid temperature evolution for different values of the thermal conductivity k_m, using hourly thermal loads.

6.4 Volumetric heat capacity

Another important parameter in subsurface heat transfer is the volumetric heat capacity (SECTION 2.4.4). Based on the encountered lithology, this parameter was initially estimated at 2.4 MJ/(m^{3}K). As with thermal conductivity, the model is simulated using different volumetric heat capacity values to determine which one provides the best fit with the evolution of the monitored ground temperature.

6.4.1 Daily thermal loads

As shown in TABLE 6.3, the modelled fluid temperature evolution was compared to the monitored fluid temperature evolution for different values of volumetric heat capacity. Initially, the RMSE was computed to quantify the error between the two temperature curves. However, this method showed certain limitations. Indeed, the lowest RMSE was obtained for a volumetric heat capacity of 3.3 MJ/(m^{3}K), which seems much too high for characterising the subsurface at the RDI site, according to the values reported in CSTC (2016). Once again, this is due to the greater weight given to large errors when using RMSE. Therefore, a method was needed to calculate the error without allowing the mismatch observed during the first ten days to have too much influence on the result. For this reason, the Mean Absolute Error (MAE) was also calculated for the different volumetric heat capacity values. MAE is less sensitive to outliers than RMSE, as it does not square the errors. It is defined as:

$$\text{MAE} = \frac{1}{n}\sum_{i=1}^{n}|y_i - \hat{y}_i| \tag{6.1}$$

Whereas RMSE is defined as:

$$\text{RMSE} = \sqrt{\frac{1}{n}\sum_{i=1}^{n}(y_i - \hat{y}_i)^2} \tag{6.2}$$

where y_i represents the monitored fluid temperature, $\hat{y}_i$ the modelled fluid temperature, and n the number of compared points.

Regardless of whether RMSE or MAE is used, the values show that volumetric heat capacity has a relatively small impact on the model solution, given the low differences between errors. The selected calibration value should be chosen as a compromise between RMSE and MAE. These two methods produce inversely correlated error trends, so the ideal choice is a value that produces low errors for both, has a small difference between them, and remains physically plausible. The selected value of 2.5 MJ/(m^{3}K) meets these criteria. It is also close to the initially estimated value. FIGURE 6.9 shows that the temperature evolutions obtained for $\rho_b c_b$ values of 2.4 and 2.5 MJ/(m^{3}K) are nearly indistinguishable. The distinction between the two curves is only visible at a few specific points: for most of the period, the green curve entirely overlaps the blue one. The blue curve corresponds to the optimised model from the SECTION 6.3.1, while the green curve represents the temperature evolution for the selected value of $\rho_b c_b = 2.5$ MJ/(m^{3}K). Volumetric heat capacity affects the fluctuations of the model response. Although the difference is difficult to distinguish on FIGURE 6.9 due to the narrow range of $\rho_b c_b$ values, a higher volumetric heat capacity allows the ground to store more heat without undergoing rapid temperature changes.

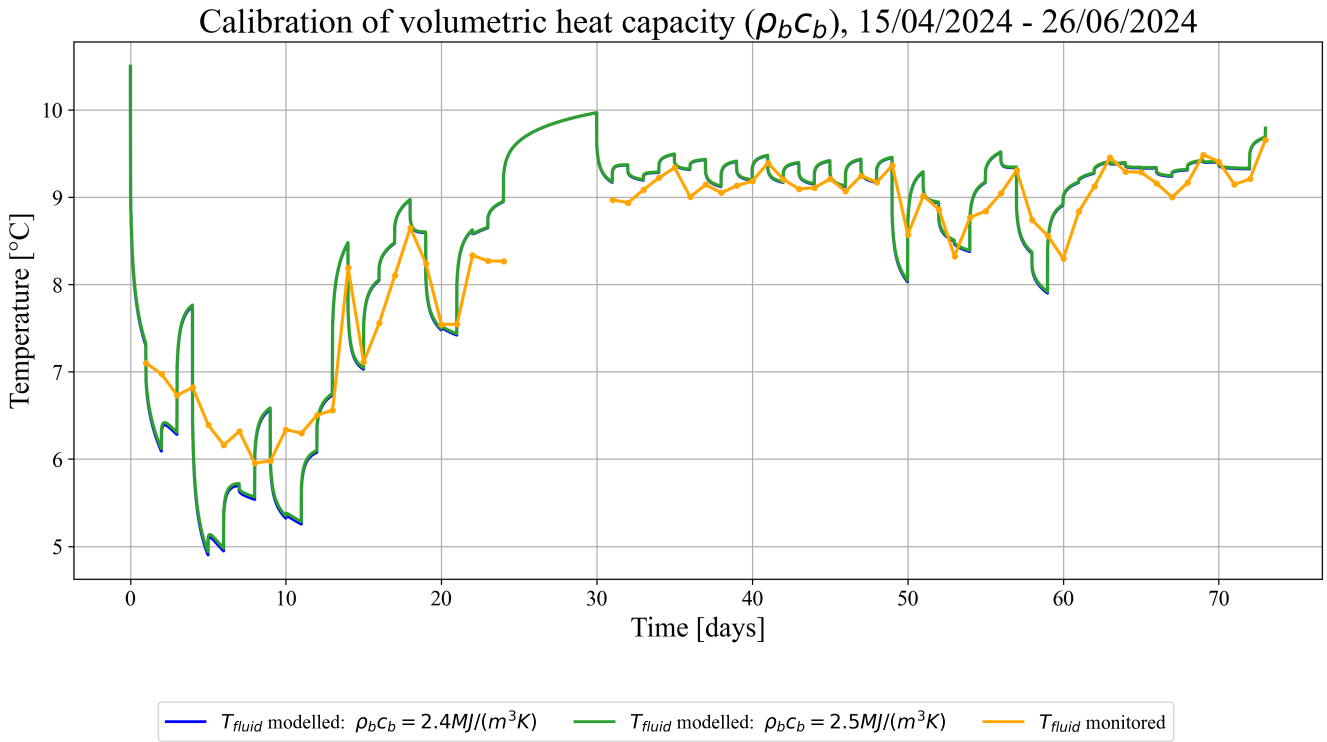

FIGURE 6.9: Comparison between modelled and monitored fluid temperature evolution for different values of the volumetric heat capacity $\rho_b c_b$.

TABLE 6.3: RMSE and MAE between modelled and monitored ground temperature for different values of volumetric heat capacity $\rho_b c_b$.

Volumetric heat capacity $\rho_b c_b$ [MJ/(m^{3}K)]	**RMSE** [°C]	**MAE** [°C]
2.0	0.429	0.308
2.1	0.424	0.307
2.2	0.422	0.310
2.3	0.418	0.310
2.4	0.415	0.310
2.5	0.411	0.310
2.6	0.410	0.311
2.7	0.408	0.311
2.8	0.406	0.312
2.9	0.406	0.314
3.0	0.405	0.314
3.1	0.404	0.314
3.2	0.403	0.315
3.3	0.402	0.316
3.4	0.405	0.320

6.4.2 Hourly thermal loads

As with the other results obtained using hourly thermal loads, the simulated ground temperature shows high fluctuations (FIGURE 6.10). The impact of volumetric heat capacity on the model response remains minimal. The RMSE decreases only from 2.576 °C to 2.555 °C. The two curves corresponding to different values of volumetric heat capacity are therefore almost the same, the difference is barely noticeable to the naked eye. This confirms the observation already made during the daily calibration. In the range tested, the volumetric heat capacity has a small effect on the model's performance.

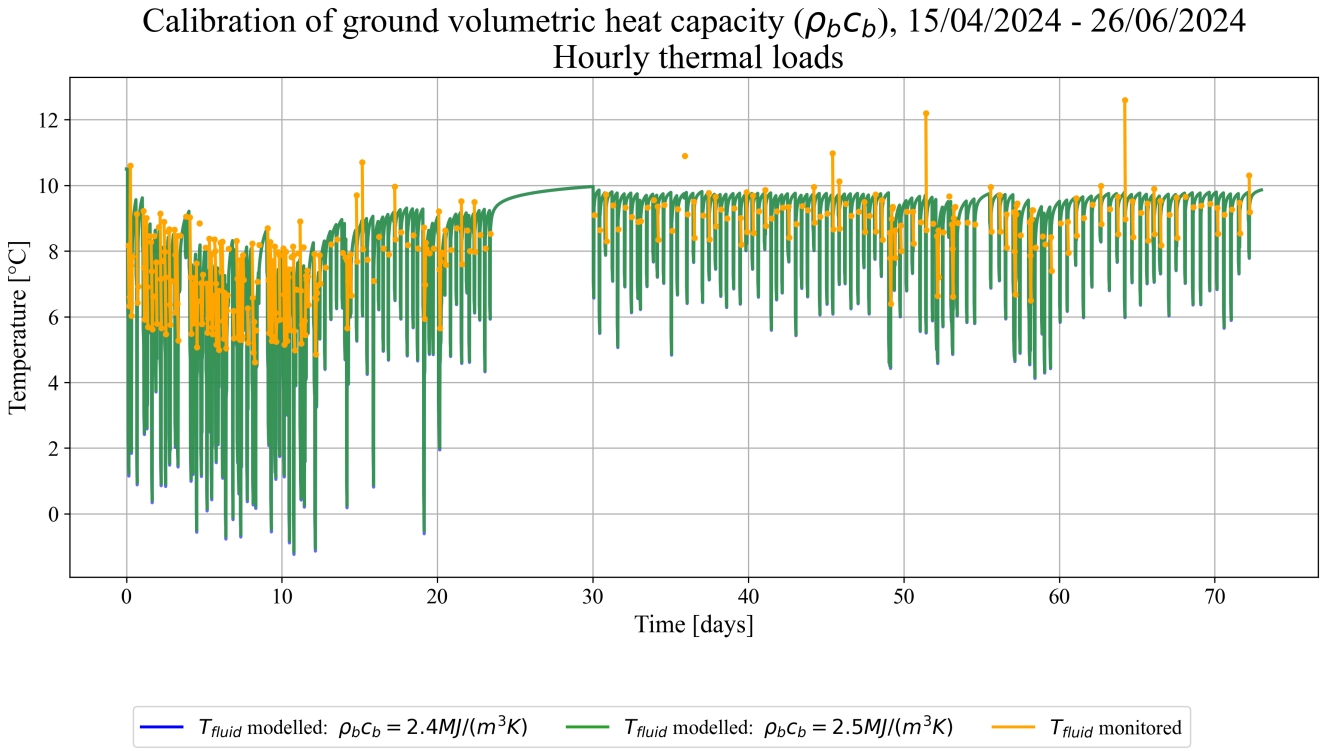

FIGURE 6.10: Comparison between modelled and monitored fluid temperature evolution for different values of the volumetric heat capacity $\rho_b c_b$, using hourly thermal loads.

6.5 Borehole thermal resistance

Another parameter that influences heat transfer and therefore the underground temperature is the borehole thermal resistance (R_b, EQUATION 4.8). This resistance depends mainly on two factors, the thermal conductivity of the grout material and the thermal conductivity of the probe material. Both determine how efficiently heat is transferred from the heat-transfer fluid to the surrounding ground.

6.5.1 Grout thermal conductivity

The first parameter calibrated is the grout thermal conductivity. It is more likely that this parameter differs from the initially estimated value than the probe's conductivity, since the depth distribution and composition of the grout material are a greater uncertainty than the probe properties.

Daily thermal loads

In continuity with SECTION 6.4, both the RMSE and MAE were calculated to calibrate the thermal conductivity of the grout material (k_b). FIGURE 6.11 and TABLE 6.4 confirm that this parameter influences the modelled fluid temperature. More precisely, k_b directly affects the borehole thermal resistance R_b (also listed in the table), which in turn governs the fluid temperature through EQUATION 4.8. The thermal conductivity of the grout is highly dependent on its composition (Mahmoud et al., 2021). Based on RMSE values, the best fit between the modelled and monitored temperatures is obtained for k_b values of 2.1 or 2.2 W/(mK). As these are relatively high, the lower value of 2.1 W/(mK) is retained, especially since it also

corresponds to the lowest MAE. The initial estimate of grout thermal conductivity was therefore underestimated. This discrepancy is likely due to the presence of silica gravel, whose higher thermal conductivity compared to bentonite had not been sufficiently accounted for. The second column of TABLE 6.4 shows that, as expected, R_b decreases with increasing k_b. The range of R_b values highlights the sensitivity of the thermal resistance to changes in grout conductivity. The selected value of $k_b = 2.1$ W/(mK) corresponds to a thermal resistance of $R_b = 0.0693$ (mK)/W. From day 10 onwards, the model calibrated with this value yields a temperature evolution that better matches the monitored data, although some discrepancies persist.

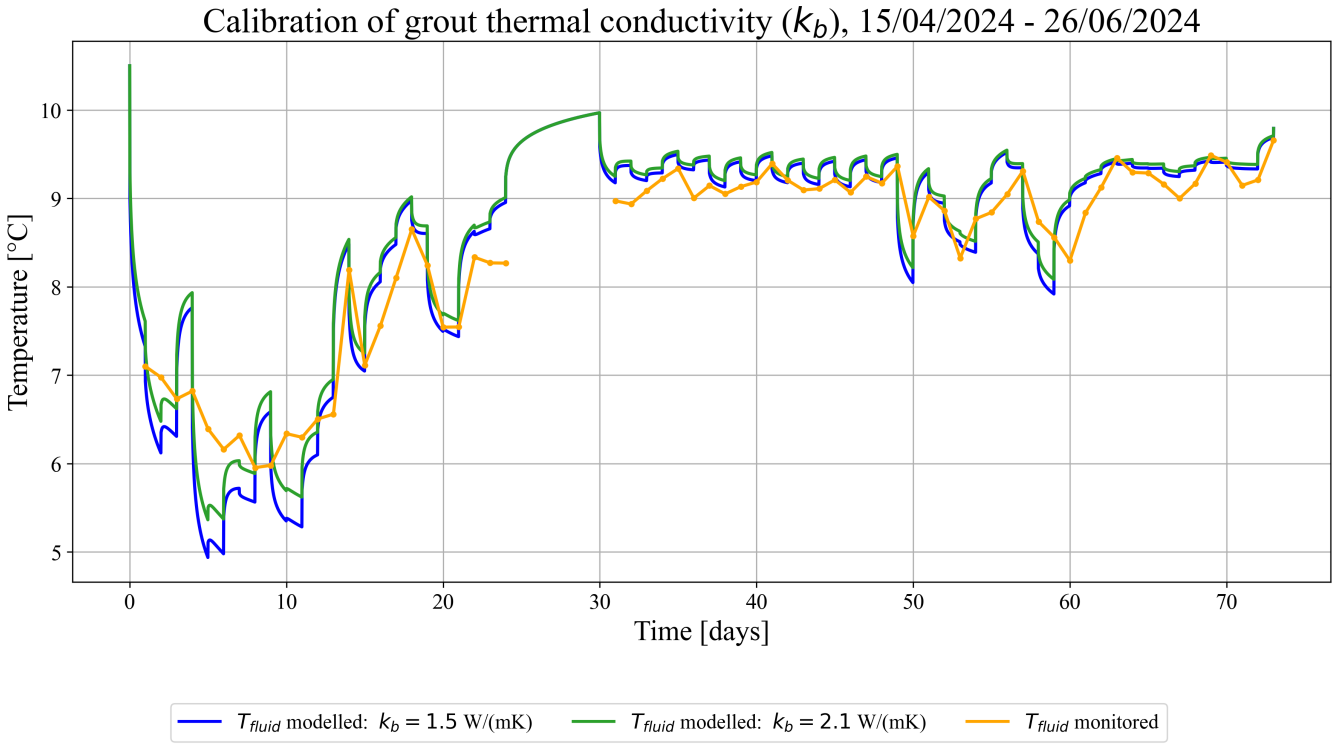

FIGURE 6.11: Comparison between modelled and monitored fluid temperature evolution for different values of the thermal conductivity of the grout k_b.

TABLE 6.4: RMSE and MAE between modelled and monitored fluid temperature, and corresponding borehole thermal resistance R_b for different values of the grout thermal conductivity k_b.

Grout thermal conductivity k_b [W/(mK)]	R_b [(Km)/W]	**RMSE** [°C]	**MAE** [°C]
1.3	0.0956	0.449	0.326
1.4	0.0907	0.427	0.317
1.5	0.0865	0.411	0.310
1.6	0.0827	0.400	0.306
1.7	0.0794	0.391	0.303
1.8	0.0765	0.386	0.302
1.9	0.0739	0.382	0.302
2	0.0715	0.380	0.303
2.1	0.0693	0.379	0.304
2.2	0.0673	0.379	0.307
2.3	0.0655	0.380	0.310

Hourly thermal loads

FIGURE 6.12 shows how increasing the grout thermal conductivity leads to a reduction in the amplitude of simulated temperature fluctuations. Indeed, a higher grout thermal conductivity allows the model to transfer heat more efficiently between the fluid and the ground, which directly reduces the borehole thermal resistance. As described by EQUATION 4.8, the fluid temperature within the borehole is influenced by the product of the extracted heat flux and the borehole thermal resistance ($q \cdot R_b$). In the short term, the ground temperature at the borehole wall can be assumed constant due to its higher thermal inertia. Therefore, variations in the fluid temperature primarily reflect changes in the heat extraction rate modulated by R_b. Lowering R_b reduces the amplitude of these fluctuations, making the modelled response more consistent with the real behaviour, where the thermal inertia of the borehole would dampen rapid changes. As a result, the model performance improved, with the RMSE decreasing from 2.555 to 2.109 °C.

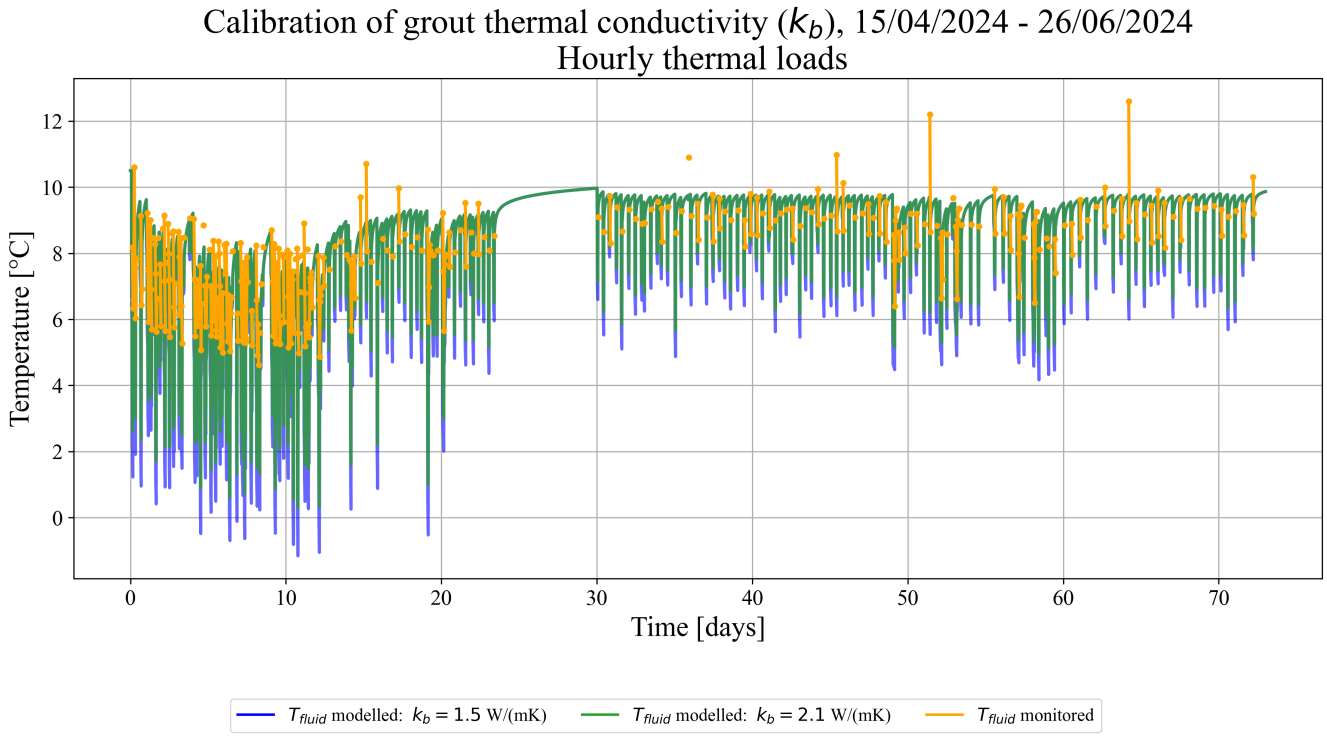

FIGURE 6.12: Comparison between modelled and monitored fluid temperature evolution for different values of the thermal conductivity of the filling material k_b, using hourly thermal loads.

6.5.2 Probe thermal conductivity

Daily thermal loads

TABLE 6.5 shows that varying the thermal conductivity of the probe k_p has a negligible effect on the modelled fluid temperature when daily thermal loads are applied. The maximum difference in RMSE across the tested range is only 0.001 °C, and similar stability is observed for MAE values. This very limited sensitivity is explained by the fact that the thermal conductivity of the probe has only a minor influence on the overall borehole thermal resistance, which varies by only $5 \cdot 10^{-3}$ (mK)/W across the tested range. Since R_b is the parameter directly used in the analytical model to calculate the fluid temperature, variations in k_p have a minimal impact on the results. Therefore, the initial value of 0.4 W/(mK), corresponding to the thermal conductivity of polyethylene, was retained for the calibrated model. The temperature evolution simulated with this configuration corresponds to the green curve shown previously in FIGURE 6.11.

TABLE 6.5: RMSE and MAE between modelled and monitored fluid temperature, and corresponding borehole thermal resistance R_b for different values of the thermal conductivity of the probe k_p.

Probe thermal conductivity k_p [W/(mK)]	R_b [(Km)/W]	**RMSE** [°C]	**MAE** [°C]
0.37	0.0712	0.380	0.303
0.38	0.0705	0.379	0.303
0.39	0.0699	0.379	0.303
0.40	0.0693	0.379	0.304
0.41	0.0687	0.379	0.305
0.42	0.0682	0.379	0.306
0.43	0.0677	0.379	0.306
0.44	0.0672	0.379	0.307
0.45	0.0667	0.379	0.308
0.46	0.0663	0.379	0.309
0.47	0.0658	0.380	0.309
0.48	0.0654	0.380	0.310

Hourly thermal loads

Since no calibration is performed when using hourly thermal loads, the influence of the probe thermal conductivity is also considered negligible under this scenario. Therefore, the simulated ground temperature evolution remains identical to the green curve shown in FIGURE 6.12.

6.6 Groundwater specific discharge

The last major parameter influencing the model's results is the presence of groundwater flow. Up to this point, all simulations were performed assuming a zero specific discharge. Under this assumption, the simulated fluid temperatures, particularly when using daily thermal loads, showed good agreement with the monitored data. The lowest RMSE achieved was 0.379 °C.

So far, model calibration has been based on the fluid temperature at the centre of the central borehole (FIGURE 6.1). This choice was made for simplicity, as in the absence of groundwater flow, the fluid temperatures in the three boreholes are nearly identical, an assumption that is verified in SECTION 6.6.1. As a result, comparing the modelled fluid temperature at the centre of the central borehole with the monitored temperature is a reasonable approximation. Indeed, the measured temperature, derived from the inlet and outlet sensors of the heat pump, reflects a combination of the fluid temperatures from all three boreholes, which are nearly identical in the absence of groundwater flow.

However, when groundwater flow is introduced, thermal interactions between the boreholes increase, and the downstream boreholes may be affected by the thermal plume from those upstream. In this case, the fluid temperatures in the three boreholes may diverge, and computing the average temperature across the three boreholes becomes more representative of the monitored temperature at the heat pump. The first part of this SECTION 6.6 therefore investigates the influence of a non-zero specific discharge on the evolution of this averaged modelled fluid temperature.

Next, the second part of the analysis compares the modelled temperatures at the centre of each borehole. This serves to confirm that, in the absence of groundwater flow, the fluid temperatures are nearly identical in all boreholes. Conversely, when groundwater flow is present, temperature differences appear, showing that the boreholes interact with one another and reinforcing the relevance of averaging.

Finally, the spatial influence of groundwater flow is explored by evaluating temperature variations at multiple observation points located outside the boreholes. This last case provides a broader understanding of the subsurface thermal behaviour under advective heat transport conditions.

6.6.1 Daily thermal loads

Average modelled temperature of the boreholes

Up to this point, the model parameters have been calibrated one after the other, meaning that the value chosen for one parameter conditions the values of the others. As a result, the entire model was calibrated under the assumption of no groundwater flow. Nonetheless, evaluating the impact of introducing groundwater flow remains essential, even if it results in a less accurate match with the monitored data.

FIGURE 6.13 is therefore presented primarily to illustrate the effect of introducing a non-zero specific discharge, rather than to identify its optimal value. As shown in TABLE 6.6, the RMSE increases with increasing specific discharge. This is expected, as all other parameters were calibrated under the assumption of no groundwater flow.

FIGURE 6.13 shows the evolution of the average modelled fluid temperature at the centre of the three boreholes for four different values of specific discharge. A specific discharge of $8.57 \cdot 10^{-10}$ m/s is equivalent to zero flow, while $8.57 \cdot 10^{-8}$ m/s corresponds to the initial estimate provided in SECTION 4.2, with groundwater flow assumed to occur along the x-axis, i.e., parallel to the borehole alignment direction. The other two values, $8.57 \cdot 10^{-7}$ and $8.57 \cdot 10^{-6}$ m/s, are plausible in the Eocene sand aquifer if higher hydraulic conductivities are considered.

Introducing groundwater flow reduces the amplitude of temperature fluctuations, as illustrated by the purple curve, which shows more attenuated variations than the blue and green curves. Additionally, groundwater flow causes a faster return of the fluid temperature towards the initial ground temperature. This explains the upward shift of the temperature curves, as heat is more rapidly replenished through advection. As expected, this parameter does not affect the general trend of the curves, which remain similar to the monitored temperature trend.

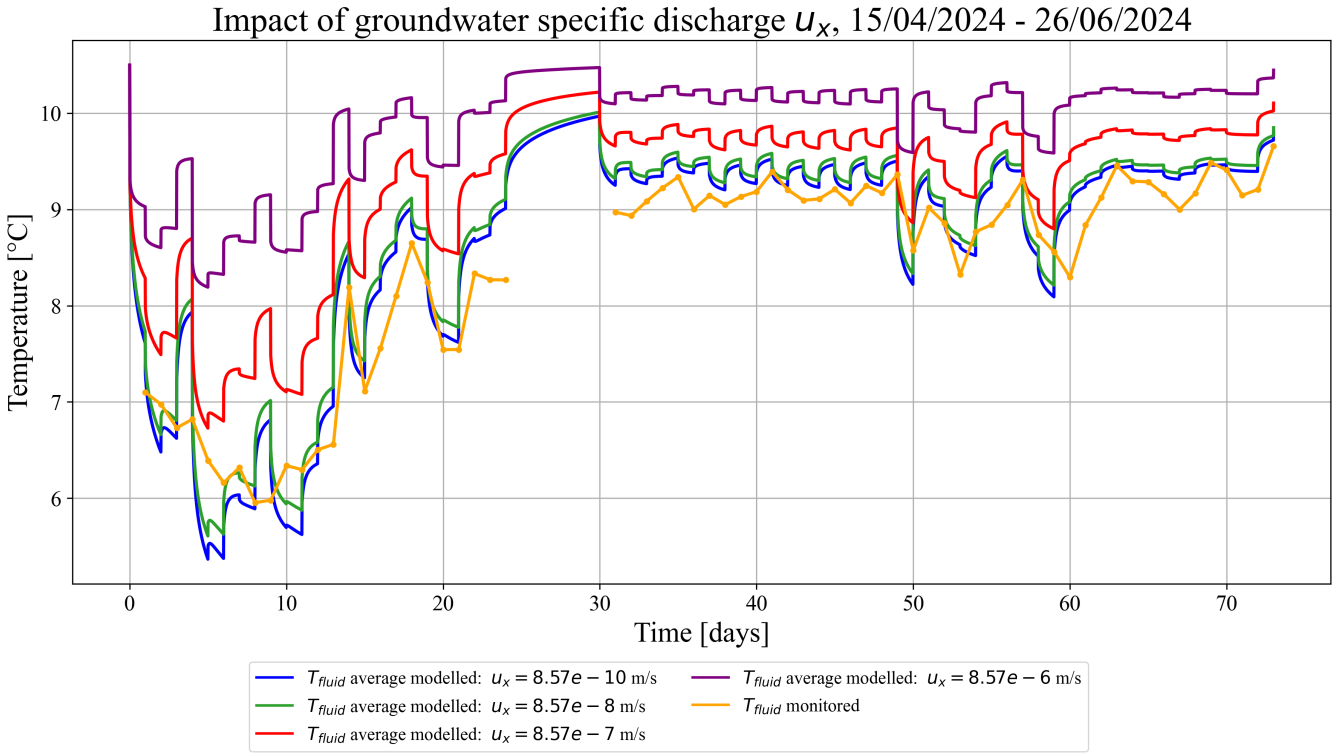

FIGURE 6.13: Comparison between the average modelled fluid temperature evolution at the centre of each borehole, and the monitored fluid temperature evolution for different values of groundwater specific discharge u_x.

TABLE 6.6: RMSE between the monitored fluid temperature and the average modelled fluid temperature at the centre of the three boreholes, for different values of groundwater specific discharge u_x.

Groundwater specific discharge u_x [m/s]	**RMSE** [°C]
0	0.379
$8.57 \cdot 10^{-10}$	0.381
$8.57 \cdot 10^{-9}$	0.384
$8.57 \cdot 10^{-8}$	0.432
$8.57 \cdot 10^{-7}$	0.895
$8.57 \cdot 10^{-6}$	1.599

Observation points at the centre of the three boreholes

This SECTION aims to evaluate the influence of groundwater flow on the fluid temperature measured at the centre of the three boreholes. To do so, three modelled temperature evolutions are compared, based on the positioning of one observation point at the centre of each borehole, as illustrated in FIGURE 6.16.

First, FIGURE 6.14 shows that in the absence of groundwater flow, the fluid temperature at the centre of the three boreholes is nearly identical. The differences are imperceptible to the naked eye, as the three curves overlap almost perfectly. Moreover, when the model is run without groundwater flow and without averaging, the best RMSE obtained is 0.379 °C (see SECTION 6.5.2). This value remains unchanged when

using the average of the three modelled borehole temperatures (see TABLE 6.6), confirming that the temperature is practically the same in all three boreholes when there is no groundwater flow. This observation supports the validity of using the central borehole as a reference point for calibration in the zero-flow case.

Then, FIGURE 6.15 demonstrates that introducing a non-zero specific discharge leads to differences in the fluid temperature between the three boreholes. To make these differences more visible, a plausible specific discharge of $8.57 \cdot 10^{-7}$ m/s is used. The boreholes are positioned at (-7, 0), (0, 0), and (7, 0), corresponding respectively to borehole 3, borehole 2, and borehole 1 (see APPENDIX A.2). The groundwater flow is assumed to occur along the x-axis, i.e. parallel to the boreholes, in accordance with the direction identified in SECTION 3.3. The FIGURE 6.15 shows that the fluid temperature in the borehole located at $(-7, 0)$ is slightly higher than in the other two boreholes (located at $(0, 0)$ and $(7, 0)$), with the latter two displaying very similar temperature evolutions. This spatial effect becomes noticeable from approximately day 20 onwards for the given specific discharge. This confirms that averaging the modelled fluid temperatures across the three boreholes is necessary to match the nature of the monitored data, which integrates the return fluid temperatures from all three boreholes, as done in SECTION 6.6.1.

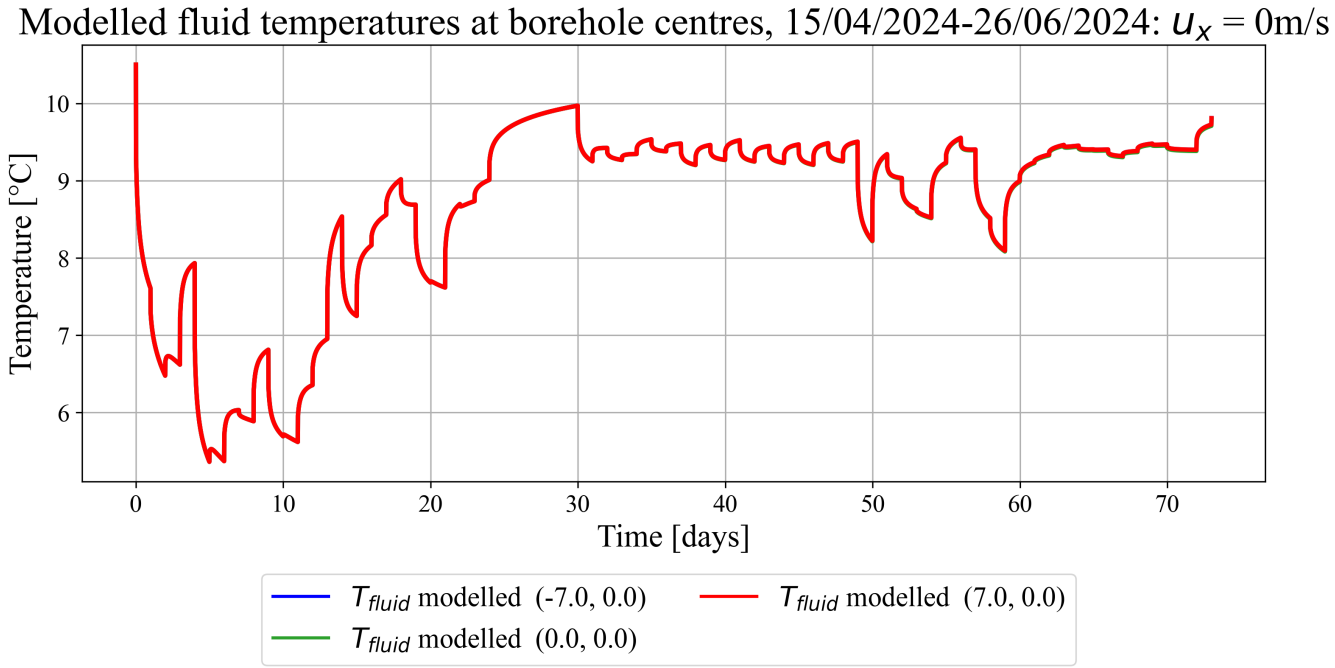

FIGURE 6.14: Modelled fluid temperature evolution at the centre of each borehole in the absence of groundwater flow ($u_x = 0$ m/s).

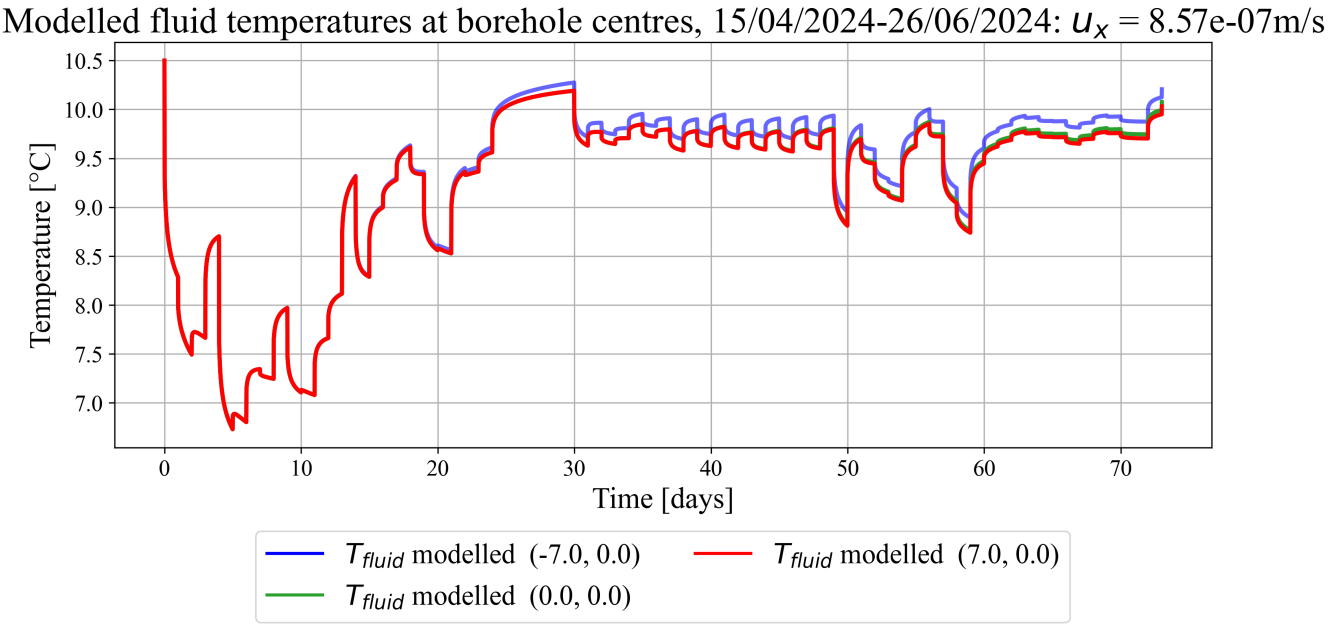

FIGURE 6.15: Modelled fluid temperature evolution at the centre of each borehole with a groundwater specific discharge of $u_x = 8.57 \cdot 10^{-7}$ m/s.

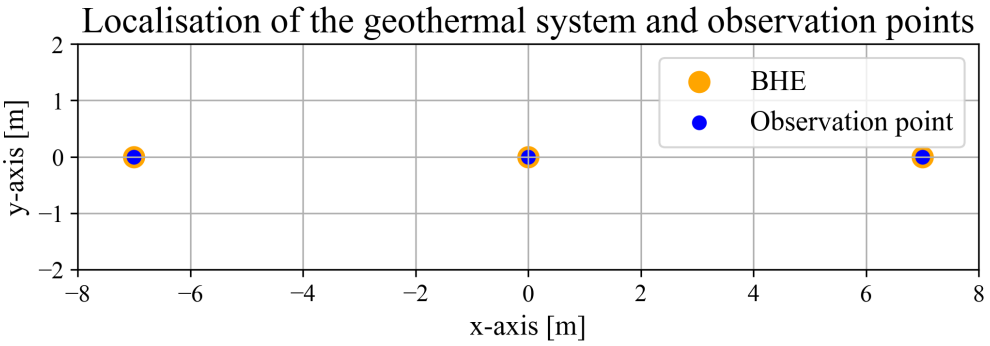

FIGURE 6.16: Configuration of the observation points located at the centre of each borehole, used to assess the spatial variability of the modelled fluid temperature under groundwater flow occurring along the x-axis.

Observation points outside the boreholes

The objective of this SECTION, and more specifically of FIGURE 6.17, is to illustrate the influence of a non-zero specific discharge at different locations. More precisely, it focuses on the modelled temperature evolution at observation points located outside the boreholes, which were not considered in previous analyses. Unlike earlier simulations that focused on the temperature at the centre of a borehole, representing the fluid temperature, this approach gives an indication of the thermal behaviour of the surrounding ground, which is essential for understanding the more general thermal response of the underground system.

FIGURE 6.17 presents the modelled temperature evolution at several observation points. Their coordinates are listed in the FIGURE legend, and their spatial distribution relative to the boreholes is shown in FIGURE 6.18. A groundwater specific discharge of $8.57 \cdot 10^{-7}$ m/s was selected to visualise the impact of

groundwater flow while remaining within a plausible range for the Eocene aquifer. The monitored fluid temperature is also shown for visual purposes. However, it cannot be directly compared to the modelled temperatures.

A first observation is that, at external observation points, temperature fluctuations are much smaller than those observed within the boreholes, this is true with or without groundwater flow. Furthermore, in the absence of groundwater flow, all external observation points exhibit the same temperature evolution, as shown in FIGURE A.20 in APPENDIX A.9. The ground temperature remains much closer to the initial ground temperature and deviates from the fluid temperature observed inside the boreholes.

Another expected result is that the upstream ground temperature (at coordinate $(-7.5, 0)$) is consistently higher than the downstream temperature (at $(7.5, 0)$), highlighting the advective heat transfer through the system. A temperature difference is also observed on both sides of a geothermal borehole: the green and red curves in FIGURE 6.17, corresponding to observation points at $(-0.5, 0)$ and $(0.5, 0)$, respectively, illustrate this local temperature gradient.

To better observe the differences between external points only, FIGURE A.21 in APPENDIX A.9 shows the temperature evolution exclusively at the external observation points.

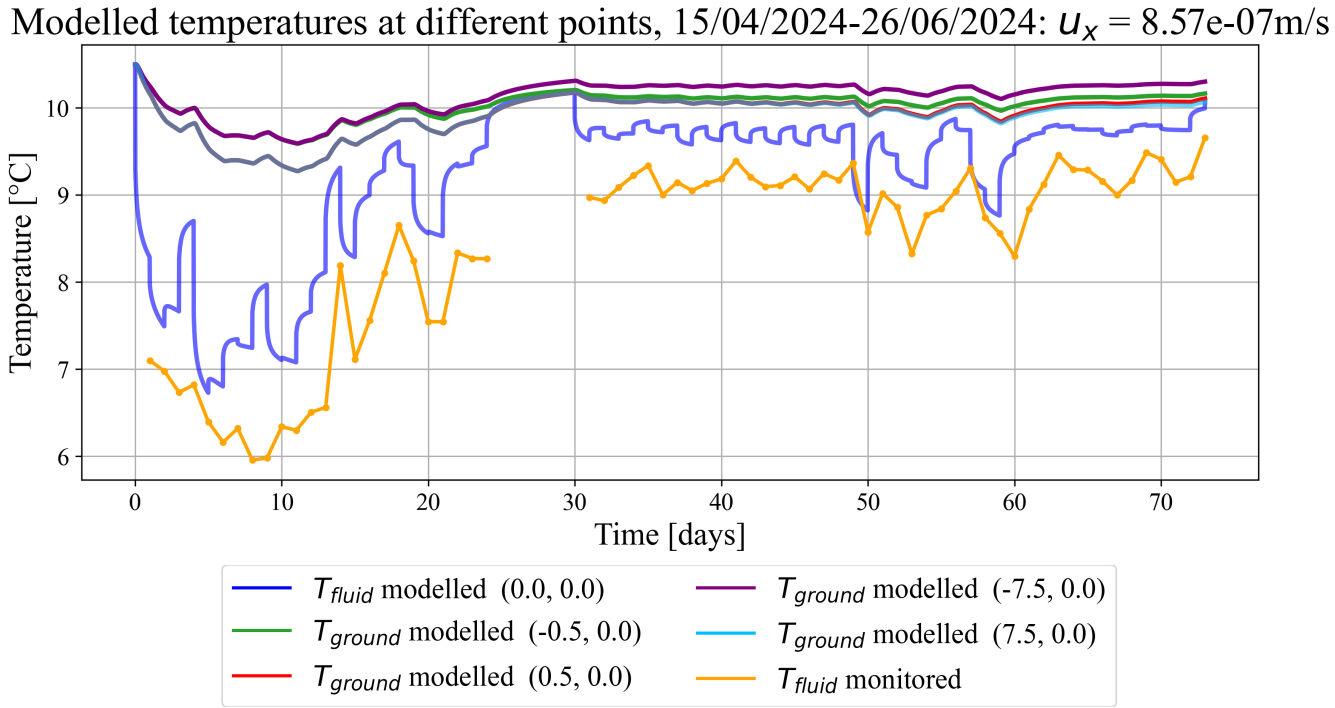

FIGURE 6.17: Modelled temperature evolutions at multiple observation points located inside and outside the boreholes, and the monitored fluid temperature evolution, for a groundwater specific discharge of $8.57 \cdot 10^{-7}$ m/s.

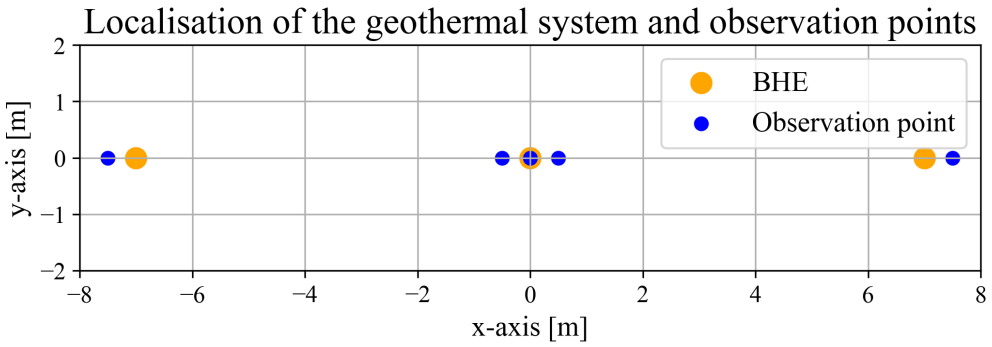

FIGURE 6.18: Localisation of the geothermal system and observation points with an observation point at the centre of the central borehole and observation points outside the boreholes.

6.6.2 Hourly thermal loads

Average modelled temperature of the boreholes

When daily thermal loads are used, an attenuation of temperature fluctuations is observed. In contrast, the results from the previous SECTIONS using hourly thermal loads showed large fluctuations in the simulated fluid temperature at the centre of the borehole. Therefore, this SECTION aims to examine whether the introduction of a specific discharge can attenuate these fluctuations when using hourly thermal loads.

FIGURE 6.19 shows the evolution of the average modelled fluid temperature, computed at the centre of each of the three boreholes, for two cases: without groundwater flow and with a specific discharge of $8.57 \cdot 10^{-7}$ m/s. Although the two curves appear largely superimposed, a slight reduction in the amplitude of fluctuations can be observed when groundwater flow is introduced. Nevertheless, the attenuation effect remains limited, short-term fluctuations persist and the simulated temperature continues to differ from the monitored values. The introduction of groundwater flow slightly increases both the minimum and maximum modelled temperatures.

While the expected improvement is not fully achieved, the results still show some enhancements, particularly through the reduced amplitude of temperature fluctuations. This observation raises the question of whether an even closer match with the monitored data could be reached. Both SECTION 6.5.1 and the present SECTION 6.6.2 have shown that the thermal conductivity of the grout and the specific discharge influence the amplitude of the model's temperature response.

To explore this further, alternative values for these parameters were tested. FIGURE 6.20 presents a comparison between the average modelled fluid temperature using the calibrated parameters with a specific discharge of $8.57 \cdot 10^{-7}$ m/s (green curve in FIGURE 6.19), and the average modelled fluid temperature obtained by increasing the grout thermal conductivity to 3 W/(mK), which corresponds to a reduced borehole thermal resistance of $R_b = 0.0562$ (mK)/W, combined with a specific discharge of $9 \cdot 10^{-7}$ m/s. These parameter values are considered optimal for attenuating the amplitude of fluctuations while remaining within a physically realistic range. Further decreasing R_b by increasing k_b would lead to even more pronounced improvements, but at the expense of departing too far from plausible material properties. FIGURE 6.20 shows a clear attenuation of the temperature fluctuations in this latter case. A more detailed and continuous monitoring dataset would have allowed for a more accurate comparison. Reducing R_b limits fluid temperature variations by bringing it closer to T_b (EQUATION 4.8). At the same time, a faster groundwater

flow enhances heat renewal, allowing the ground temperature to recover more rapidly towards its initial state.

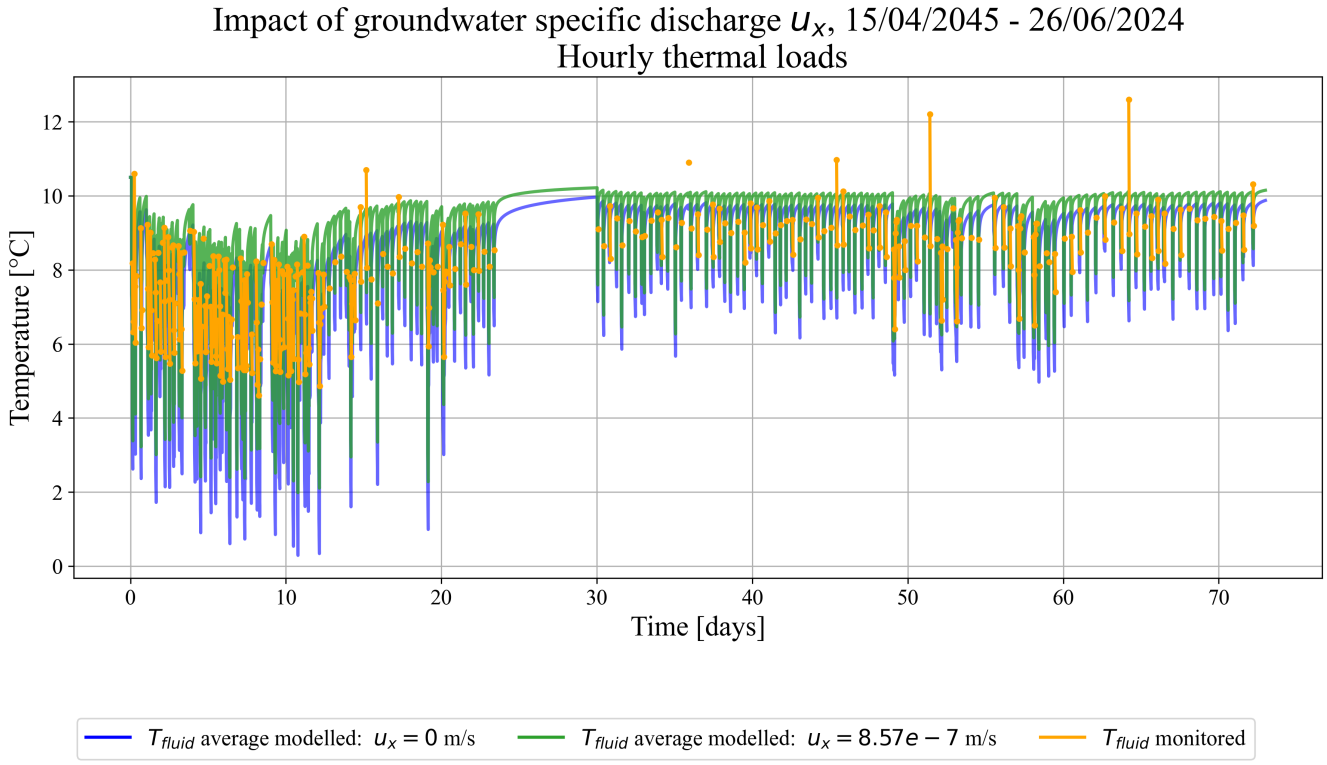

FIGURE 6.19: Comparison between the average modelled fluid temperature at the centre of each borehole and the monitored fluid temperature for different values of groundwater specific discharge u_x, using hourly thermal loads.

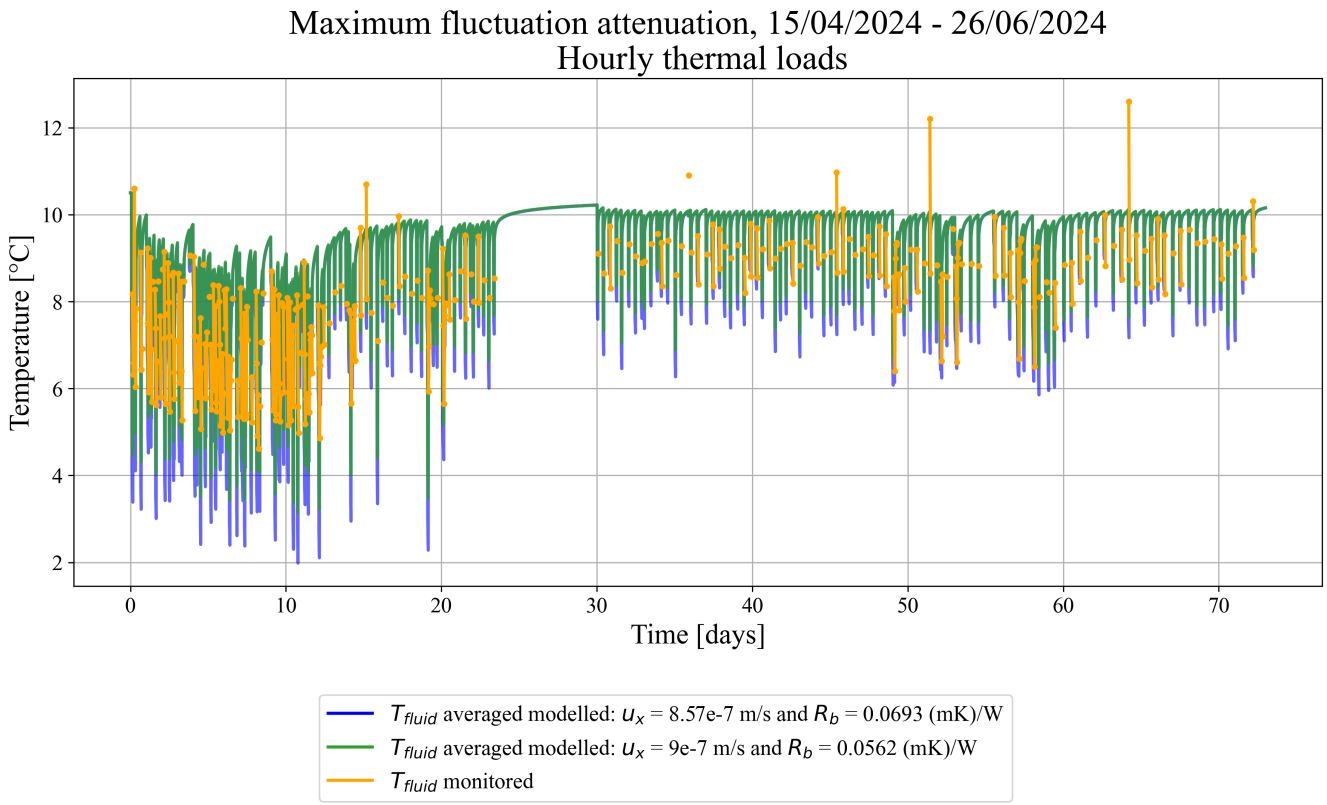

FIGURE 6.20: Comparison of average modelled fluid temperatures using hourly thermal loads for two configurations, showing reduced fluctuations with higher grout conductivity and specific discharge.

Observation points at the centre of the three boreholes

An analysis similar to that presented in SECTION 6.6.1 is carried out in this SECTION, but using hourly thermal loads. As before, when no groundwater flow is considered, the modelled fluid temperatures at the centre of the three boreholes are almost identical. This confirms that the modelled fluid temperature at the centre of the central borehole can reasonably be compared to the monitored fluid temperature, even when hourly thermal loads are used.

Furthermore, when a non-zero specific discharge is introduced, the upstream borehole exhibits a higher fluid temperature than the other two ones, which remain very close to each other.

These results are consistent with those obtained using daily thermal loads and do not provide additional insights. Therefore, the corresponding FIGURES are not included here but are presented in the APPENDIX A.9, respectively as FIGURES A.23 and A.24.

Observation points outside the boreholes

When hourly thermal loads are considered, a comparison of temperature evolution at various observation points is also carried out and presented in FIGURE 6.21. For reasons of visibility, the observation point at (0, 0) has been omitted. Overall, the results show very similar behaviour to what was observed in FIGURE 6.17 (daily thermal loads). Underground temperature fluctuations are reduced, and the temperature values between the two FIGURES are also very close. This suggests that, outside the borehole, the

thermal behaviour is very similar whatever the thermal loads used.

FIGURE A.22 in APPENDIX A.9 shows the temperature evolution exclusively at the external observation points, in order to have a better comparison of the results.

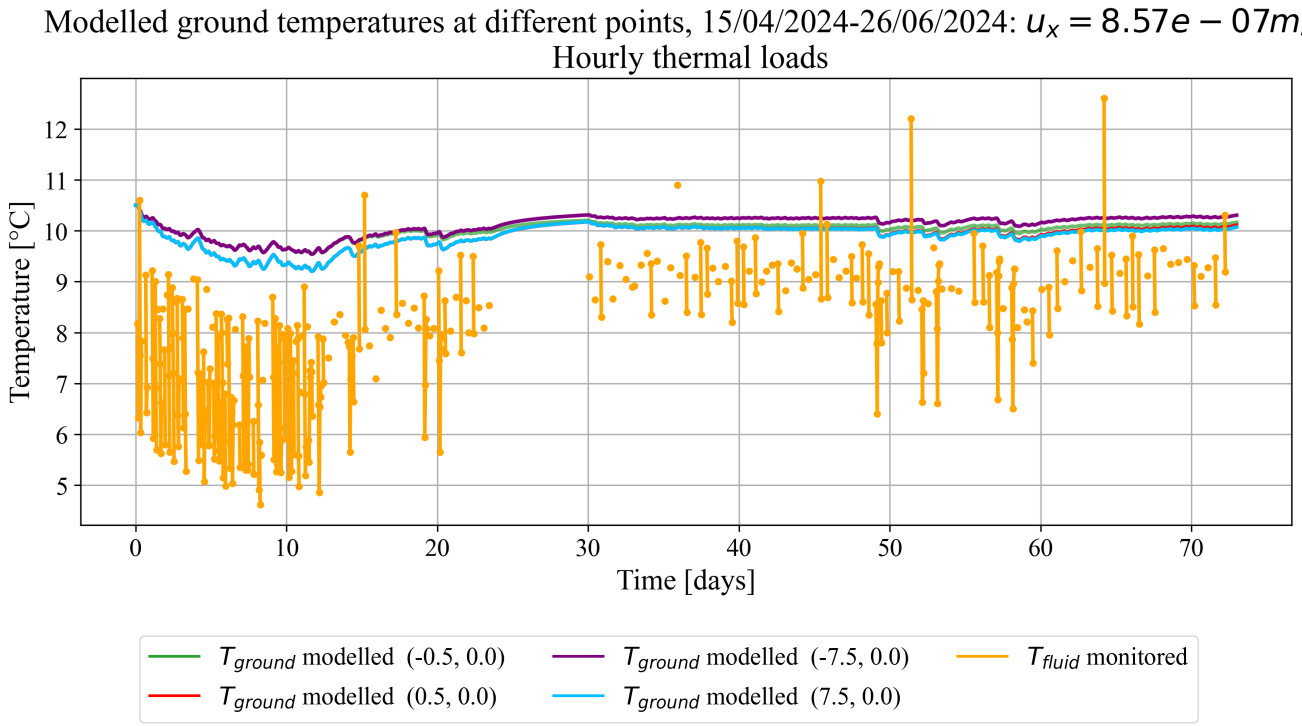

FIGURE 6.21: Modelled temperature evolution at multiple observation points located outside the boreholes, and the monitored fluid temperature evolution, for a groundwater specific discharge of $8.57 \cdot 10^{-7}$ m/s, using hourly thermal loads.

6.7 Adaptation of the geothermal system

FIGURES 6.17 et 6.21 showed, like all the others from this CHAPTER, that the monitored fluid temperature never dropped below the regulatory threshold of 2 °C. When daily thermal loads are used, the minimum temperature is around 6 °C, and about 4.5 °C when hourly thermal loads are considered. More importantly, these FIGURES highlight that, even at a short distance from the borehole, and whether or not a specific discharge is present (FIGUREA.20), the ground temperature does not undergo large variations and tends to return relatively quickly to its initial value. This suggests that the geothermal system could be resized without compromising the long-term thermal balance. Therefore, an adjustment of the specific thermal load (i.e. thermal load per metre, see EQUATION 6.3) is proposed to bring the system closer to the critical temperature limit, which would correspond to a better-optimised design. To achieve this, the specific thermal load is modified by adjusting the borehole depth.

Better sizing of the system and therefore of the depth of the geothermal probes would reduce the costs of the geothermal installation, a major factor that could influence the choice of whether or not to install a geothermal system. FIGURE 6.22 shows the modelled temperature evolution at the centre of the borehole and at an observation point located 50 cm away from it, for a configuration where all three boreholes are

61 m deep. This is the minimum depth that allows the fluid temperature to approach the critical limit, because the minimum temperature reached in this case is 2.08 °C. This means that 61% of the total depth of the boreholes is sufficient to extract energy from the ground efficiently over the studied period. Of course, as with the other parameters, this result is highly dependent on the duration of the simulated period and the thermal loads assigned during it. In addition, FIGURE 6.22 shows that the modelled temperature at the borehole centre only approaches 2 °C at two points (days 5 and 6), and earlier calibrations had already shown a fairly large difference between modelled and monitored temperatures during this phase. For the rest of the period, the temperature oscillates between 7 and 9 °C. At the observation point located at (0.5, 0), the modelled temperature remains relatively constant, especially after day 20, stabilising around 9.5 °C.

It should be noted that a single 183 m borehole presents very similar temperature evolutions at the studied observation points compared to the configuration with three 61 m boreholes.

Reducing the total borehole length by 39% implies that for the same energy demand (i.e., same E_{ground}), the specific heat extraction will be 1.64 times as high, because of the following relation:

$$\text{Specific heat extraction} = \frac{E_{ground} \cdot 1000}{24 \cdot H \cdot n} \tag{6.3}$$

where E_{ground} is the extracted energy in kWh/day, H is the borehole depth in m, and n is the number of boreholes. Therefore, operating the system with a total length of 183 m would impose the same thermal load per metre as increasing E_{ground} by a factor of 1.64 using the full 300 m length. This means that the RDI residents could extract 64% more energy from the ground than initially, without going beyond the critical temperature.

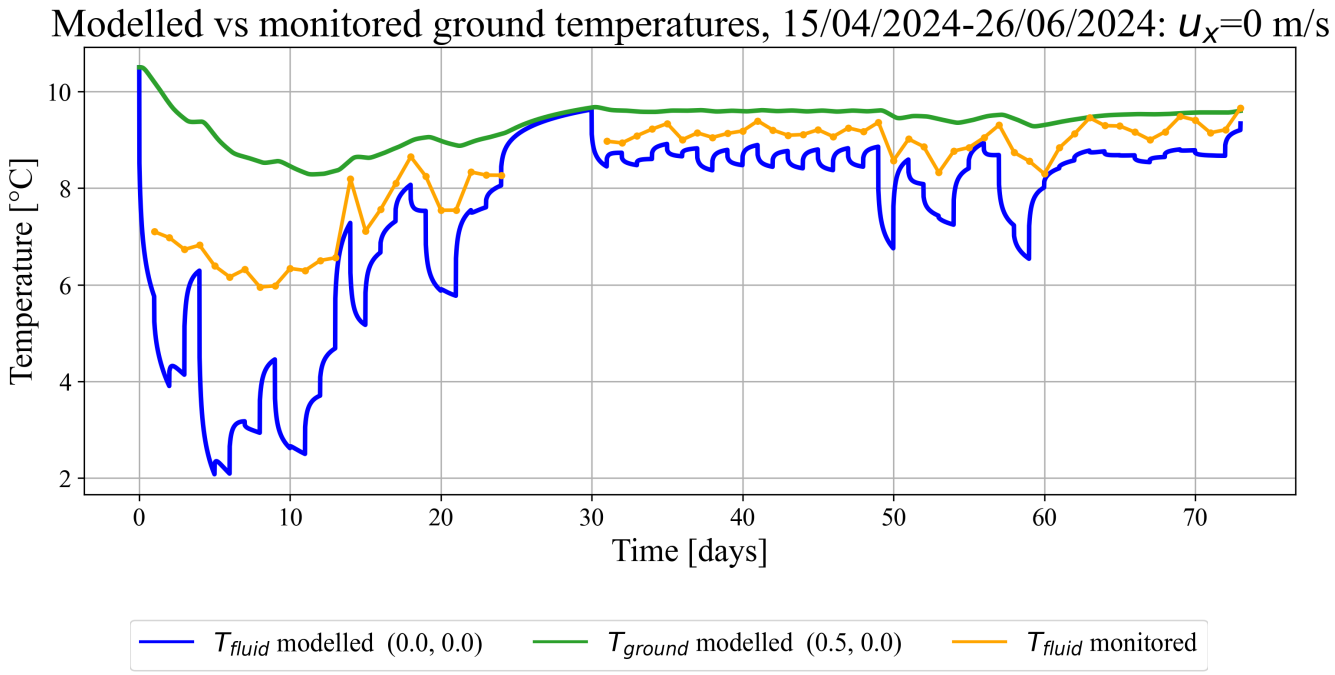

FIGURE 6.22: Comparison of modelled ground temperature evolution at the borehole centre and at 0.5 m distance, for a borehole depth of 61 m.

Chapter 7

Conclusions and perspectives

Climate change and challenges associated with decarbonising energy systems become increasingly central to public discourse. In this context, geothermal energy represents a promising low-carbon solution for heating and domestic hot water production in buildings. However, to ensure the long-term efficiency and sustainability of these systems, it is necessary to carefully plan and optimally design the borehole heat exchanger fields. Among the tools available for this purpose, the analytical model developed by Erol et al. (2015) can be highlighted. The model predicts subsurface temperature evolution based on site-specific parameters and applied thermal loads.

This thesis aimed to calibrate the model developed by Erol et al. (2015) using monitoring data collected from the geothermal system of the Relais des Ingénieurs residence in Louvain-la-Neuve. The objective was to assess the ability of the model to represent the thermal response of both the heat carrier fluid and the surrounding ground of BHEs subject to heterogeneous and intermittent loads, and to demonstrate how monitoring data, often underutilised, can enhance predictive modelling in geothermal applications.

Data filtering and preprocessing were necessary to extract meaningful information from the raw dataset. Temperatures from both primary (geothermal) and secondary (building) circuits were analysed to estimate the thermal load extracted from the ground using different methods. Unfortunately, many data points were missing, notably due to occasional interruptions of the geothermal system or the monitoring data acquisition, interference between the primary and secondary circuits, and the absence of sensors for relevant parameters, such as those needed to quantify free cooling. As a result, the analysis was limited to a short period of around seventy days, between 15 April 2024 and 26 June 2024. The selected thermal load was computed based on the temperature difference at each time step, multiplied by the flow rate and the volumetric heat capacity of the heat carrier fluid.

The parameter-by-parameter calibration showed that the initial estimates were reasonably close to the optimised values. The process began by calibrating the initial ground temperature, which had to be adjusted to 10.5 °C in order to directly align the model with the monitored data. Naturally, this had an impact on the values of the other parameters. The calibration also confirmed that some parameters have a greater influence on the outputs of the model than others. For example, the thermal conductivity of the ground had more impact than its volumetric heat capacity. Regarding the borehole thermal resistance, the calibration showed that the thermal conductivity of the grout had a greater influence on R_b than the thermal conductivity of the probe. This result is logical, given the difference in thickness between these two materials in the model. A lower R_b value led to better results, which is explained by its direct link to the fluid temperature. Starting with the calibration of one parameter not only influenced the values of the others,

but the order in which the parameters were calibrated also had an effect, changing the calibration sequence could lead to different optimal values. While the calibrated values may not fully reflect the physical reality, they still offer a good approximation of the actual site conditions. The results demonstrated that the accuracy of the model improved after calibration, especially when using daily thermal loads, most notably after the 10^{th} day of modelling, as confirmed by the RMSE and MAE indicators. Introducing a specific discharge helped further stabilise the simulated temperatures, particularly the ground temperature, highlighting the influence of groundwater flow. A decrease in R_b combined with a specific discharge, when using hourly thermal loads, resulted in a noticeable attenuation of the simulated fluctuations and brought the modelled temperatures closer to the monitored ones. More extensive monitoring data would have been helpful to confirm this result. The final calibrated model showed good agreement with the measured data and suggested that the geothermal system may be oversized relative to the actual thermal demand during the monitoring period. The study showed that 61% of the total borehole length would have been sufficient to meet the energy needs of the RDI occupants during the analysed period, although this period likely does not reflect general consumption patterns.

Despite the relatively short monitoring duration and limitations in sensor placement and precision, the model has demonstrated its robustness and relevance. This model deserves further investigation to confirm its validity and broaden its applicability. This would require more rigorous system monitoring, with targeted, comprehensive, reliable, and longer-term data collection, in order to obtain the necessary parameters for a more robust calibration.

For the RDI, this could be achieved by adding temperature sensors, either via fibre optics in the geothermal probe in order to obtain greater accuracy of the fluid temperature, and to record temperature variations at different depths. Sensors would also be needed on either side of the free cooling exchanger in order to analyse the behaviour of the model during free cooling events. Monitoring and quantifying the free cooling phase, which can significantly influence ground temperature regeneration, would also improve model validation and predictive capability. Furthermore, reducing thermal interference between the primary and secondary circuits through improved hydraulic layout would allow for more reliable data acquisition.

Beyond these practical improvements, it would be beneficial to simulate the three-dimensional evolution of ground temperature to better capture spatial dynamics around the geothermal probes and validate the model under more complex conditions. Finally, replacing the sequential parameter calibration with a simultaneous multi-parameter calibration approach would help reduce interdependence effects and increase calibration robustness. A sensitivity analysis could further clarify the impact of each parameter on model response.

By combining high-quality monitoring and robust modelling, this approach contributes to the optimisation of geothermal system design and supports the broader energy transition toward low-carbon heating technologies.

Bibliography

Accueil - Celsius process. (2020, June). *Celsius Process*. Retrieved May 15, 2025, from https://www.celsius-process.com/

Atlas climatique. (2020). *KMI*. Retrieved May 22, 2025, from https://www.meteo.be/fr/climat/climat-de-la-belgique/atlas-climatique/cartes-climatiques/temperature-de-lair/moyenne/annuel

Bloemendal, M., & Hartog, N. (2018). Analysis of the impact of storage conditions on the thermal recovery efficiency of low-temperature ates systems. *Geothermics*, *71*, 306–319. https://doi.org/10.1016/j.geothermics.2017.10.009

Centre Scientifique et Technique de la Construction (CSTC). (2016). Note d'information technique 259: Géothermie peu profonde - Conception et mise en œuvre de systèmes avec échangeurs en forme de U. Retrieved April 22, 2025, from https://www.buildwise.be/fr/publications/notes-d-information-technique/259/

Cerfontaine, B., Radioti, G., Collin, F., & Charlier, R. (2016). Formulation of a 1D finite element of heat exchanger for accurate modelling of the grouting behaviour: Application to cyclic thermal loading. *Renewable Energy*, *96*, 65–79. https://doi.org/10.1016/j.renene.2016.04.034

Coen, T., François, B., & Gerard, P. (2021). Analytical solution for multi-borehole heat exchangers field including discontinuous and heterogeneous heat loads. *Energy and Buildings*, *253*, 111520. https://doi.org/10.1016/j.enbuild.2021.111520

Collignon, V., Brouyère, S., & Orban, P. (2023). Étude de caractérisation des eaux pluviales en Région de Bruxelles Capitale, vulnérabilité intrinsèque du système aquifère phréatique par rapport au transfert de la pollution de surface et ses paramètres hydrodispersifs - Délivrable D03 : Synthèse bibliographique des paramètres hydrodispersifs relatifs au Système Phréatique Bruxellois et développement d'une méthodologie permettant l'évaluation des risques de transfert des polluants pertinents vers les nappes phréatiques. *Handle.net*. https://doi.org/https://hdl.handle.net/2268/312879

Constantz, J. (2008). Heat as a tracer to determine streambed water exchanges. *Water Resources Research*, *44*. https://doi.org/10.1029/2008wr006996

Dassargues, A. (2019). *Hydrogeology : Groundwater science and engineering*. Crc Press, Taylor & Francis Group. C.

Dassargues, A., & François, B. (2024). GEOL1046-1: Geothermal energy [Lecture notes from the course "GEOL1046-1: Geothermal Energy", Faculty of Applied Sciences, University of Liège].

Dewallef, P. (2024). Geothermal energy - Use of heat pumps [Lecture slides from the course "GEOL1046-1: Geothermal Energy", Faculty of Applied Sciences, University of Liège].

Dickson, M. H., & Fanelli, M. (2013, July). *Geothermal energy*. Routledge. https://doi.org/10.4324/9781315065786

Earle, S. (2015, September). 9.2 the temperature of earth's interior. *Opentextbc.ca*. Retrieved April 9, 2025, from https://opentextbc.ca/geology/chapter/9-2-the-temperature-of-earths-interior/

Émissions par secteur. (n.d.). *Klimaat | Climat*. Retrieved March 25, 2025, from https://climat.be/en-belgique/climat-et-emissions/emissions-des-gaz-a-effet-de-serre/emissions-par-secteur

Erol, S., Hashemi, M. A., & François, B. (2015). Analytical solution of discontinuous heat extraction for sustainability and recovery aspects of borehole heat exchangers. *International journal of thermal sciences*, *88*, 47–58. https://doi.org/10.1016/j.ijthermalsci.2014.09.007

Eurostat. (2023, June). Energy consumption in households. *ec.europa.eu*. Retrieved April 3, 2025, from https://ec.europa.eu/eurostat/statistics-explained/index.php?title=Energy_consumption_in_households

Figueira, J. S., Gil, A. G., Vieira, A., Michopoulos, A. K., Boon, D. P., Loveridge, F., Cecinato, F., Götzl, G., Epting, J., Zosseder, K., Bloemendal, M., Woods, M., Christodoulides, P., Vardon, P. J., Borg, S. P., Poulsen, S. E., & Andersen, T. R. (2024). Shallow geothermal energy systems for district heating and cooling networks: Review and technological progression through case studies. *Renewable Energy*. https://doi.org/10.1016/j.renene.2024.121436

Géothermie - Geolys. (2024, September). *Geolys*. Retrieved April 10, 2025, from https://www.geolys.be/service/geothermie/

Gigot, V., Francois, B., Huysmans, M., & Gerard, P. (2023). Monitoring of the thermal plume around a thermally activated borehole heat exchanger and characterization of the ground hydro-geothermal parameters. *Renewable energy*, *218*. https://doi.org/10.1016/j.renene.2023.119250

Herbosch, A., & Blockmans, S. (2012a). Carte géologique de Wallonie - Wavre - Chaumont-Gistoux (40/1-2). Service Public de Wallonie. Retrieved May 12, 2025, from https://geologie.wallonie.be/files/ressources/geologie/planches/40-1-2_Wavre_Chaumont.jpg

Herbosch, A., & Blockmans, S. (2012b). Notice de la carte géologique de Wavre - Chaumont-Gistoux (40/1-2). Service Public de Wallonie. Retrieved May 12, 2025, from https://geologie.wallonie.be/files/ressources/geologie/notices/40-1-2_Wavre_Chaumont.pdf

Hopmans, J. W., Šimunek, J., & Bristow, K. L. (2002). Indirect estimation of soil thermal properties and water flux using heat pulse probe measurements: Geometry and dispersion effects. *Water Resources Research*, *38*, 7-1-7–14. https://doi.org/10.1029/2000wr000071

Kulasekara, H., & Seynulabdeen, V. (2019, September). A review of geothermal energy for future power generation. *IEEE Xplore*. https://doi.org/10.1109/ICAEE48663.2019.8975470

Lee, C., & Lam, H. (2008). Computer simulation of borehole ground heat exchangers for geothermal heat pump systems. *Renewable Energy*, *33*, 1286–1296. https://doi.org/10.1016/j.renene.2007.07.006

Lemort, V. (2023). MECA0002-1: Thermodynamique appliquée et introduction aux machines thermiques [Lecture notes from the course "MECA0002-1: Thermodynamique appliquée et introduction aux machines thermiques", Faculty of Applied Sciences, University of Liège].

Mahmoud, M., Ramadan, M., Abdelkareem, M. A., & Olabi, A. G. (2023). Shallow geothermal energy ground loop systems. *Elsevier eBooks*, 121–141. https://doi.org/10.1016/b978-0-323-95211-8.00017-8

Mahmoud, M., Ramadan, M., Pullen, K., Abdelkareem, M. A., Wilberforce, T., Olabi, A.-G., & Naher, S. (2021). A review of grout materials in geothermal energy applications. *International Journal of Thermofluids*, *10*, 10. https://doi.org/10.1016/j.ijft.2021.100070

Masse d'eau souterraine RWE051 - Sables du Bruxellien. (2006). Retrieved May 15, 2025, from https://sillonblog.wordpress.com/wp-content/uploads/2017/02/masse-deau-souterraine-rwe051-sables-du-bruxellien.pdf

Naicker, S. S., & Rees, S. J. (2019). Long-term high frequency monitoring of a large borehole heat exchanger array. *Renewable Energy*, *145*, 1528–1542. https://doi.org/10.1016/j.renene.2019.07.008

Philippe, M., Bernier, M., & Marchio, D. (2009). Validity ranges of three analytical solutions to heat transfer in the vicinity of single boreholes. *Geothermics*, *38*, 407–413. https://doi.org/10.1016/j.geothermics.2009.07.002

Portail cartographique. (2024). *Le Brabant wallon*. Retrieved May 12, 2025, from https://www.brabantwallon.be/le-brabant-wallon/territoire/portail-cartographique

Preene, M., & Powrie, W. (2009). Ground energy systems: From analysis to geotechnical design. *Géotechnique*, *59*, 261–271. https://doi.org/10.1680/geot.2009.59.3.261

Resolia. (2023a). Drilling report - Relais des Ingénieurs site.

Resolia. (2023b). Hydraulic layout - Relais des Ingénieurs site.

Ruthy, I. (2017). Carte hydrogéologique de Wallonie - Wavre - Chaumont-Gistoux (40/1-2). Service Public de Wallonie. Retrieved May 12, 2025, from https://environnement.wallonie.be/files/eDocs%20Environnement/Milieux/Eau/Hydrogeologie/cartosig/Posters/4012.pdf

Self, S. J., Reddy, B. V., & Rosen, M. A. (2013). Geothermal heat pump systems: Status review and comparison with other heating options. *Applied Energy*, *101*, 341–348. https://doi.org/10.1016/j.apenergy.2012.01.048

Stober, I., & Bucher, K. (2021). *Geothermal energy : From theoretical models to exploration and development*. Springer.

Viessmann BE - Pompe à chaleur eau sol Vitocal 300-G. (2024, June). *Viessmann.be*. Retrieved May 12, 2025, from https://www.viessmann.be/fr/produits/pompes-a-chaleur/vitocal-300-g.html

Walonmap | Géoportail de la Wallonie. (2025). *Wallonie.be*. Retrieved May 13, 2025, from https://geoportail.wallonie.be/walonmap#BBOX=-142148.73063246132

Appendices

A.1 Regional geology

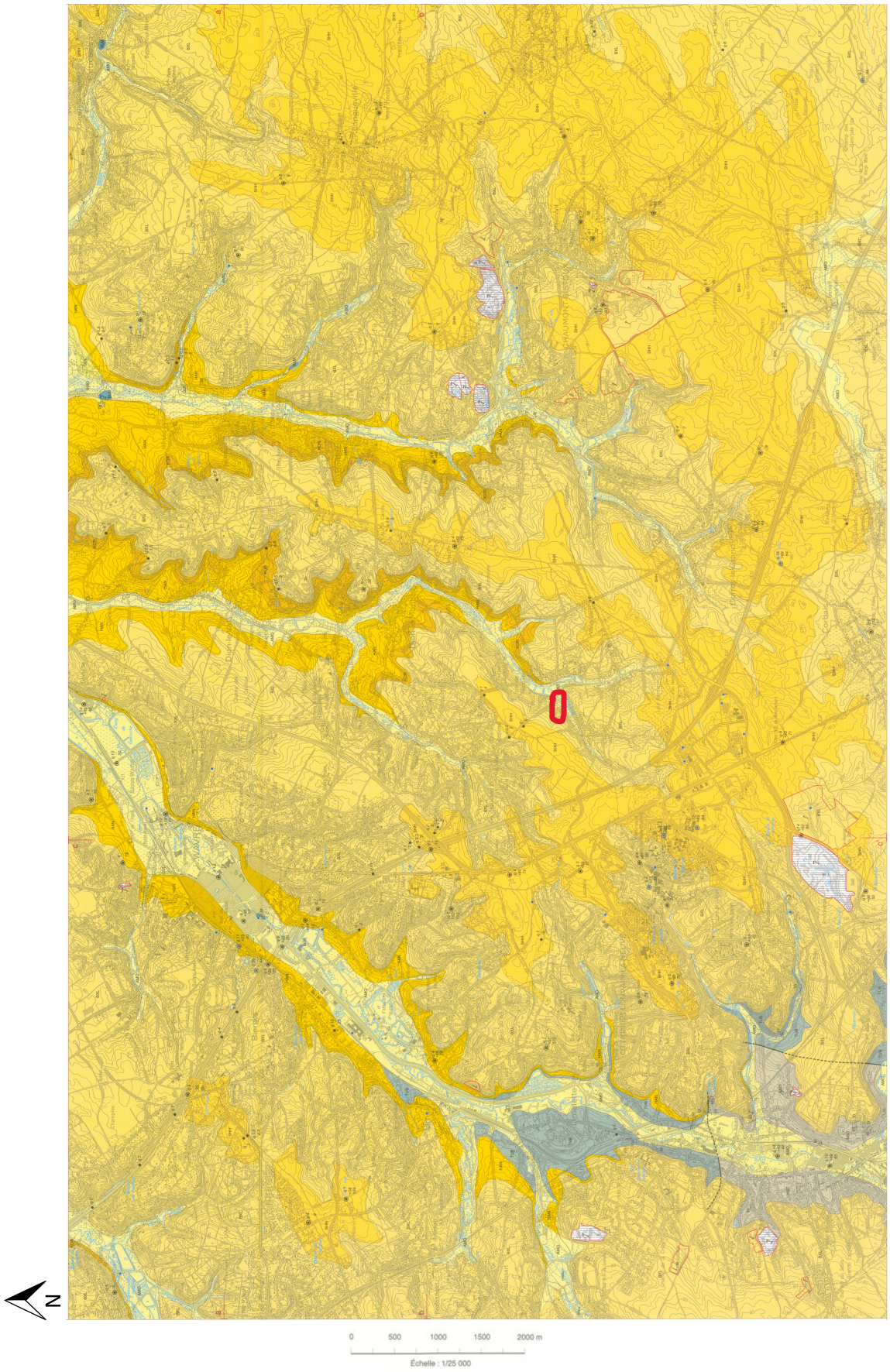

FIGURE A.1: Regional geological map of Wavre-Chaumont-Gistoux (modified from Herbosch & Blockmans, 2012a).

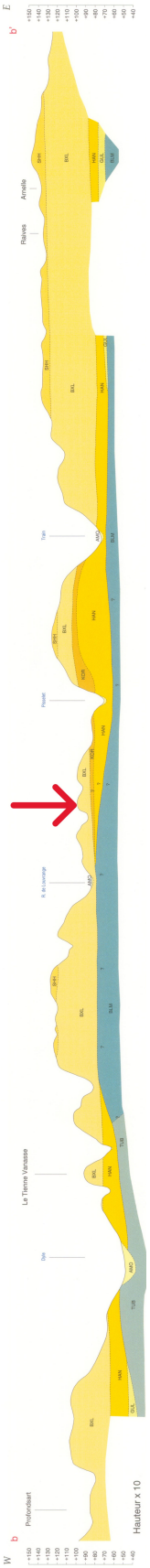

FIGURE A.2: Geological cross-section b-b' from FIGURE A.1 (modified from Herbosch & Blockmans, 2012a).

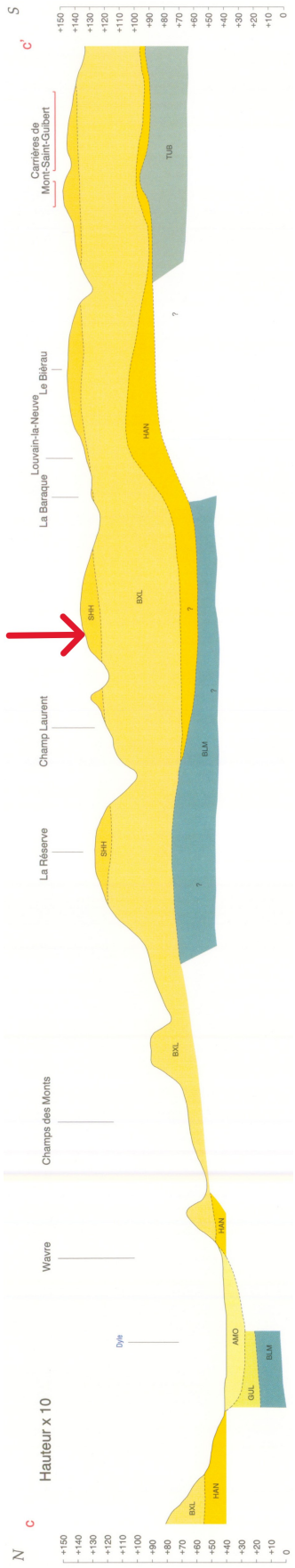

FIGURE A.3: Geological cross-section c-c' from FIGURE A.1 (modified from Herbosch & Blockmans, 2012a).

FIGURE A.4: Legend of the lithologies for FIGURES A.1 to A.3 (Herbosch & Blockmans, 2012a).

A.2 Drilling report

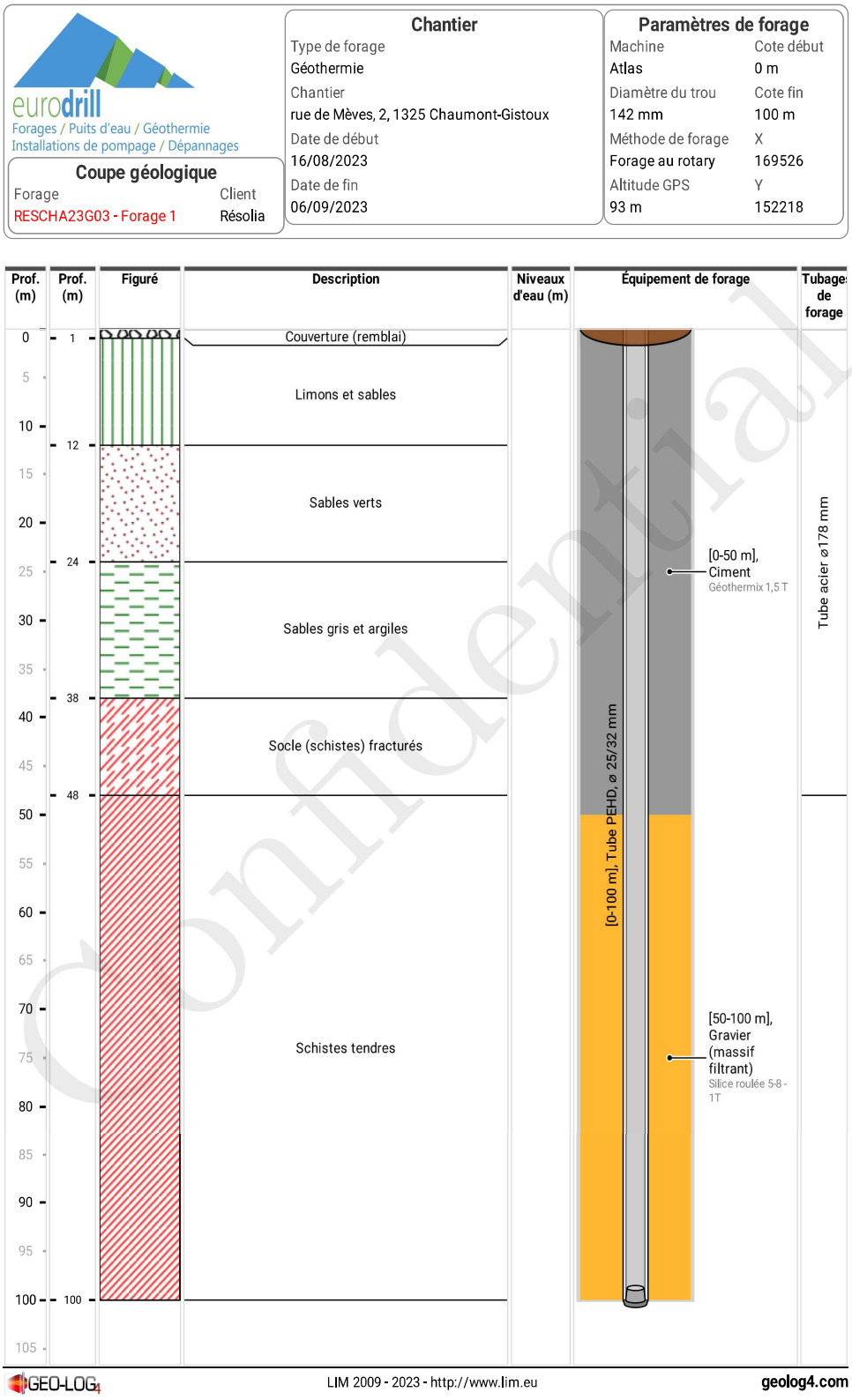

FIGURE A.5: Borehole 1 - located downstream (modified from Resolia, 2023a).[1].

[1]This document may not be distributed without the prior written consent of the issuing company: Resolia Srl.

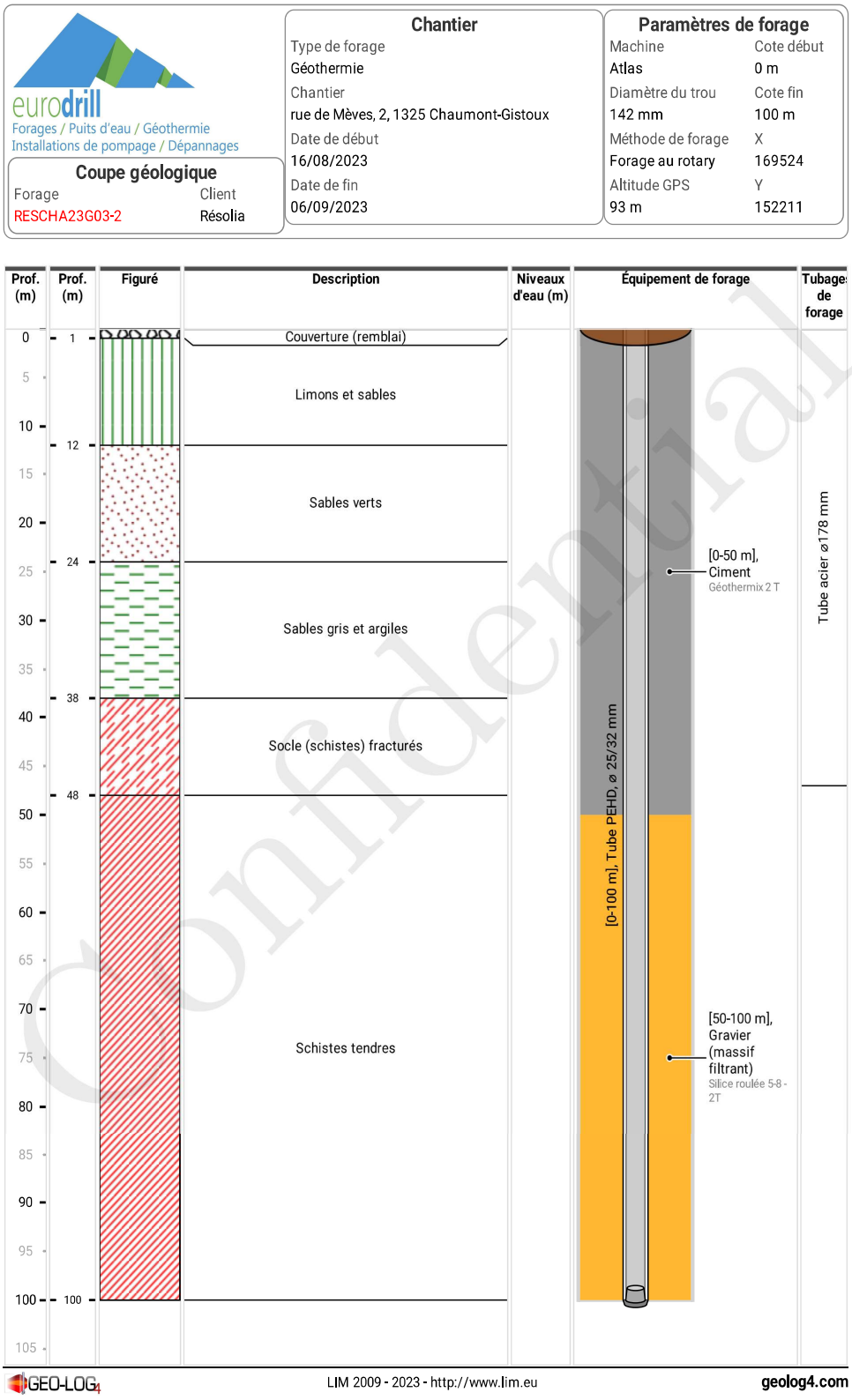

FIGURE A.6: Borehole 2 - located in the middle (modified from Resolia, 2023a).[2].

[2]This document may not be distributed without the prior written consent of the issuing company: Resolia Srl.

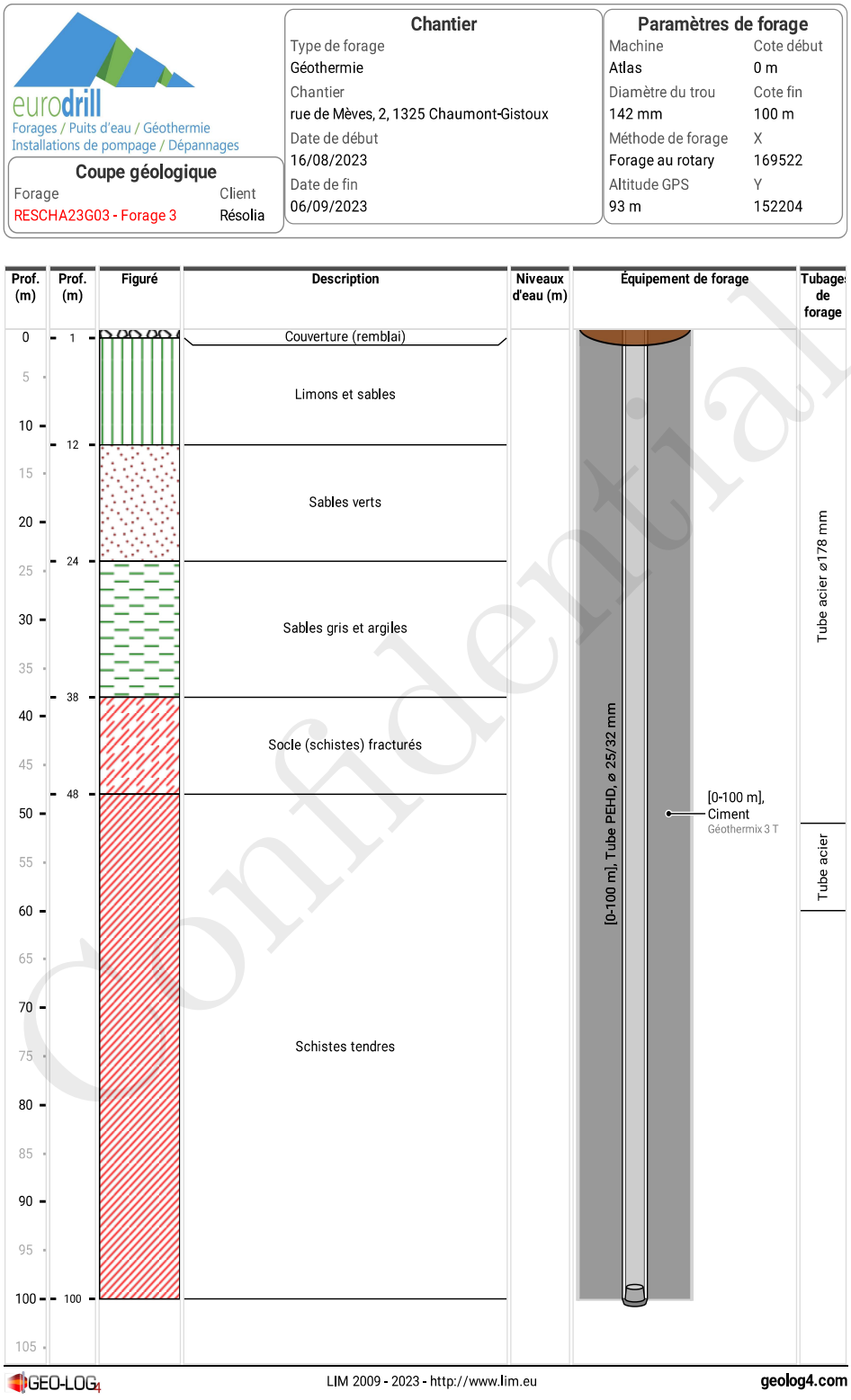

FIGURE A.7: Borehole 3 - located upstream (modified from Resolia, 2023a)[3].

[3]This document may not be distributed without the prior written consent of the issuing company: Resolia Srl.

A.3 Flow meters for the flow rate

FIGURE A.8: Measured flow rate: 19 L/min

FIGURE A.9: Measured flow rate: 28.5 L/min

FIGURE A.10: Measured flow rate: 37 L/min

FIGURE A.11: Flow meters measuring the volumetric flow rate in the geothermal loop for each probe.

A.4 Estimation of glycol-water (20%) mixture properties

FIGURES A.12 to A.15 show the interpolations performed to estimate the properties of glycol-water fluid containing 20% monopropylene glycol ("Accueil - Celsius process", 2020).

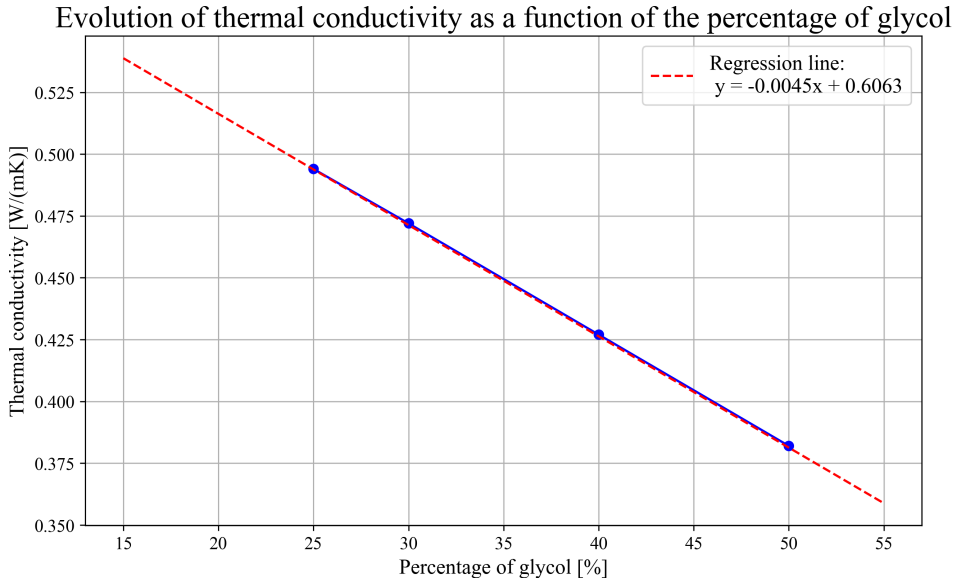

FIGURE A.12: Evolution of the thermal conductivity of glycol-water fluid as a function of glycol concentration.

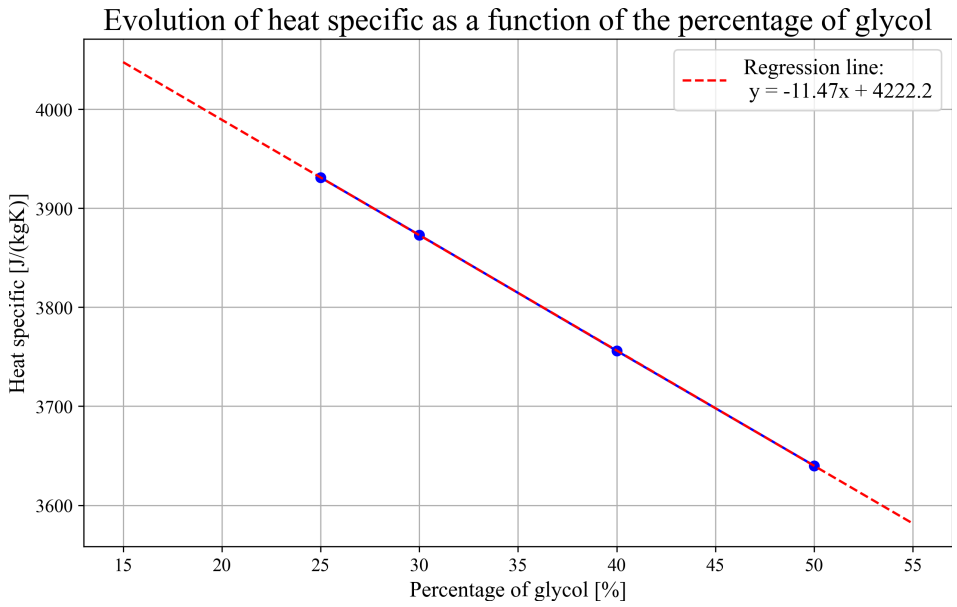

FIGURE A.13: Evolution of the specific heat capacity of glycol-water fluid as a function of glycol concentration.

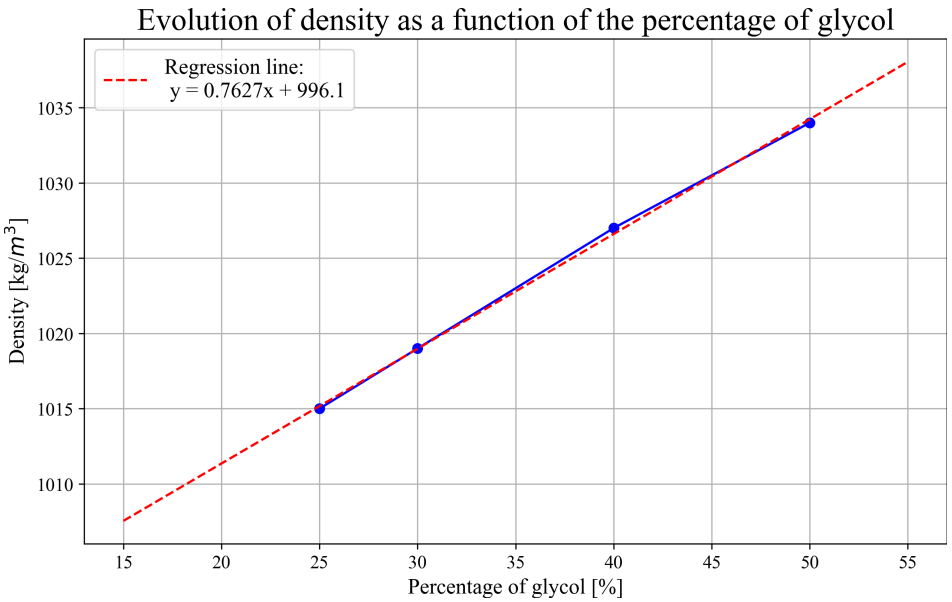

FIGURE A.14: Evolution of the density of glycol-water fluid as a function of glycol concentration.

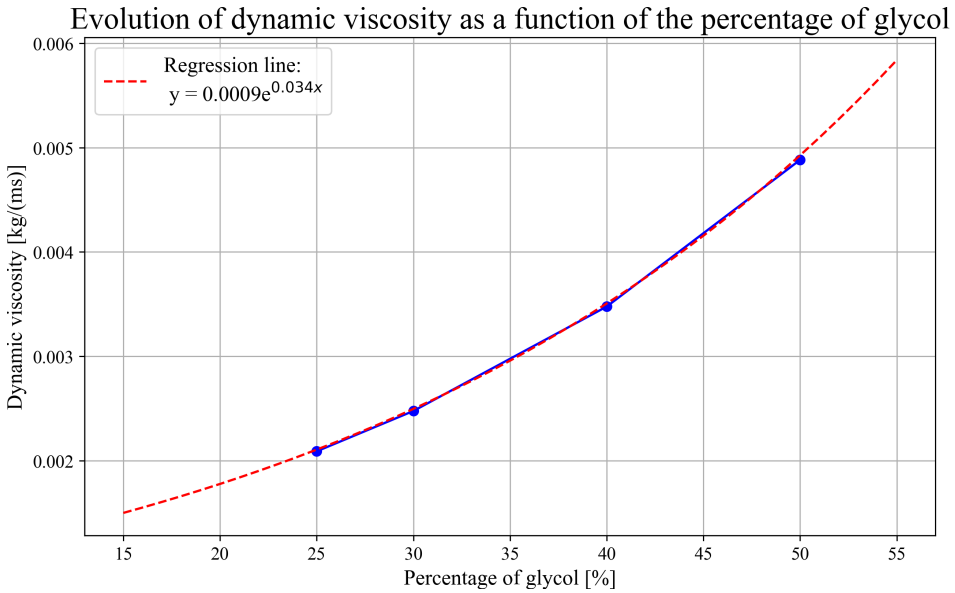

FIGURE A.15: Evolution of the dynamic viscosity of glycol-water fluid as a function of glycol concentration.

A.5 Hydraulic layout of the RDI

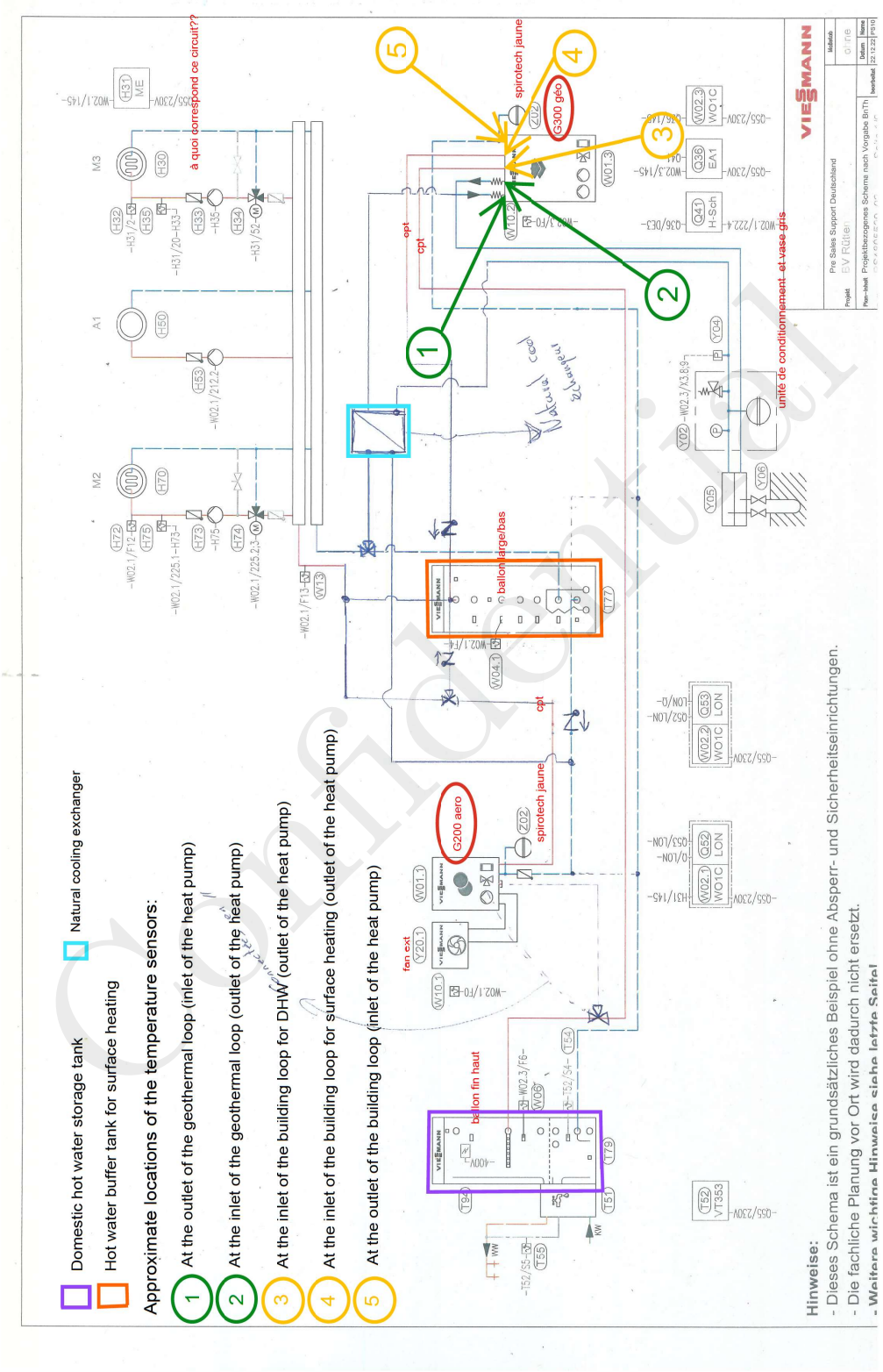

FIGURE A.16: Hydraulic layout of the RDI (modified from Resolia, 2023b)[4].

[4]This document may not be distributed without the prior written consent of the issuing company: Resolia Srl.

A.6 DHW tank and heat pump inlet temperature evolutions

FIGURE A.17 shows the evolution of the temperature in the domestic hot water tank and at the inlet of the heat pump on the primary side, over the period from 01/11/2024 to 21/11/2024. The green arrow highlights the time window used for detailed analysis (from 02/11/2024 to 05/11/2024), which is further illustrated in FIGURE 5.3.

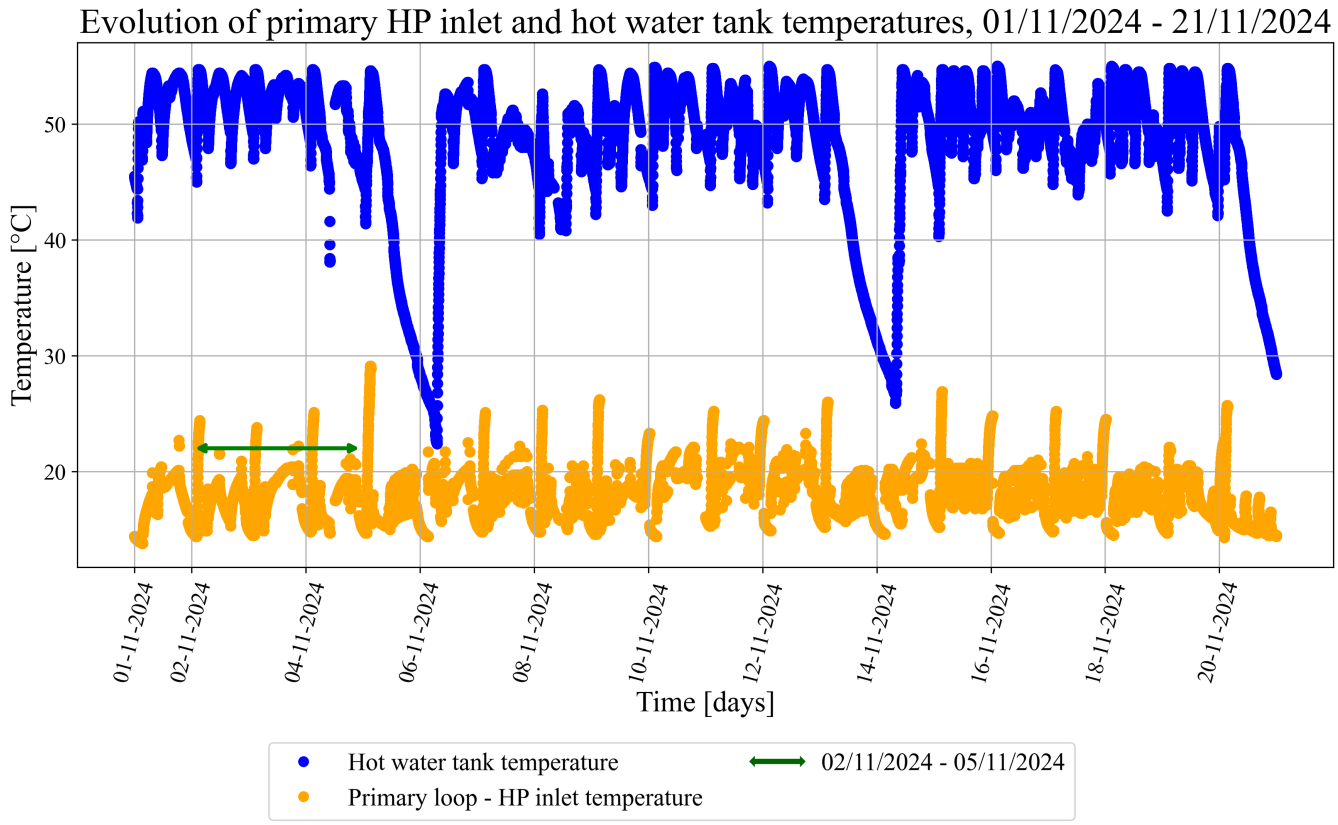

FIGURE A.17: Temperature evolution in the domestic hot water tank and at the inlet of the heat pump (HP) on the primary circuit, from 01/11/2024 to 21/11/2024. The green arrow marks the period selected for further analysis (see FIGURE 5.3).

A.7 Hourly evolution of the two circuits temperatures

FIGURE A.18 shows the hourly evolution of the inlet and outlet temperatures of the heat pump for both the primary and secondary circuits. It also distinguishes between the two operating modes of the heat pump. This FIGURE is similar to FIGURE 5.4, but with greater temperature fluctuation amplitudes.

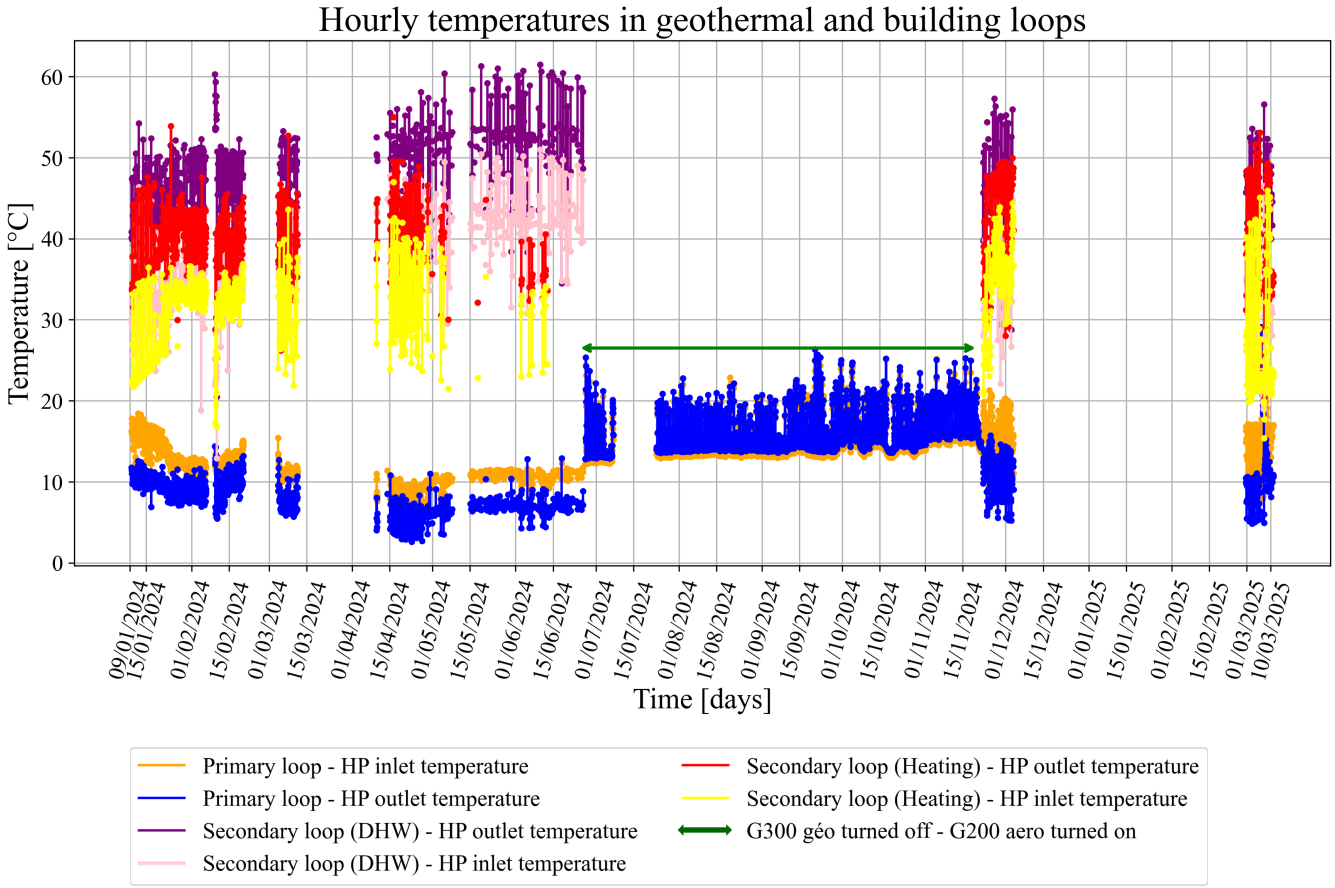

FIGURE A.18: Hourly evolution of heat pump inlet and outlet temperatures for the primary and secondary loops, distinguishing between domestic hot water and heating operation modes.

A.8 Hourly evolution of extracted ground energy over time

FIGURE A.19 compares the hourly evolution of the energy extracted from the ground, calculated using three different methods.

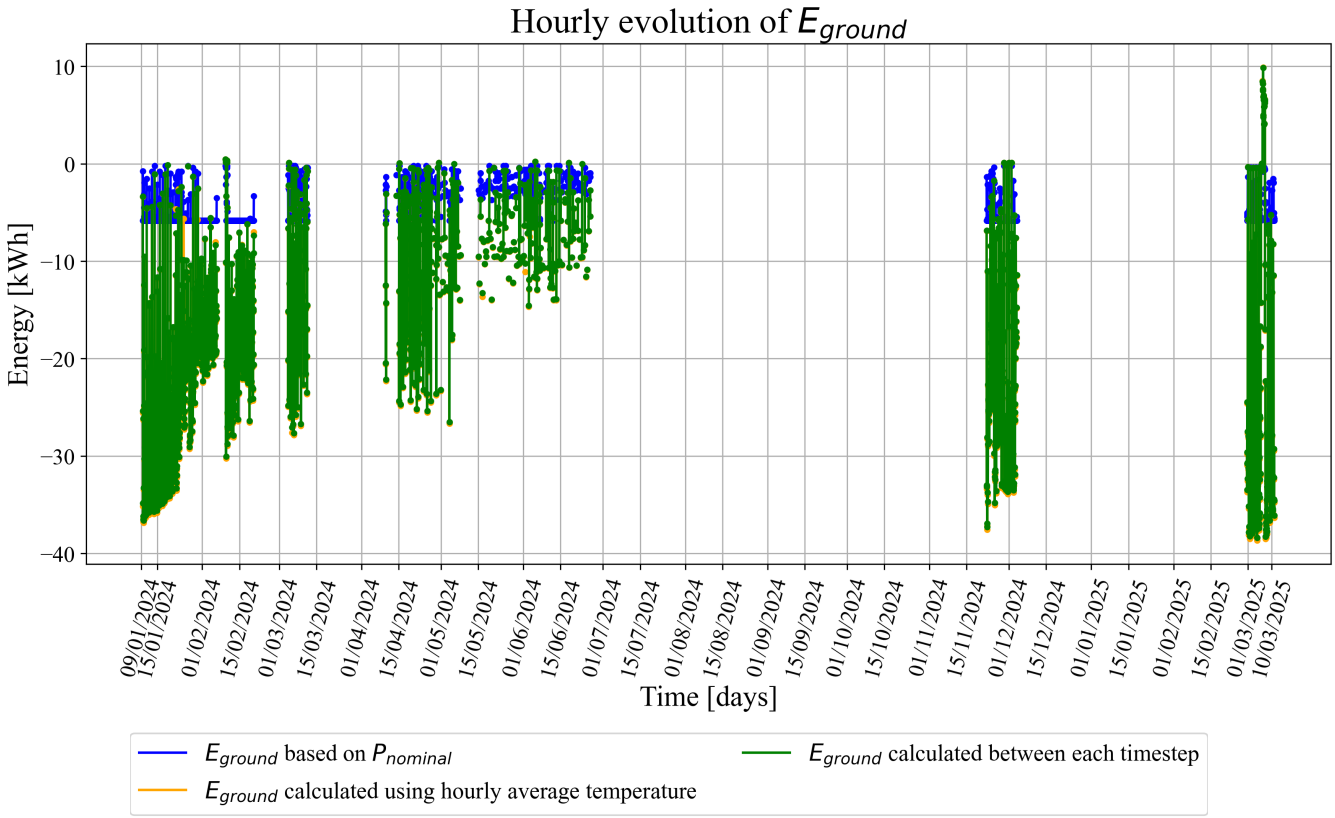

FIGURE A.19: Comparison of hourly evolution of extracted ground energy using three calculation methods.

A.9 Specific discharge

FIGURE A.20 illustrates the very small temperature variations at different observation points located outside the boreholes when no specific discharge is considered.

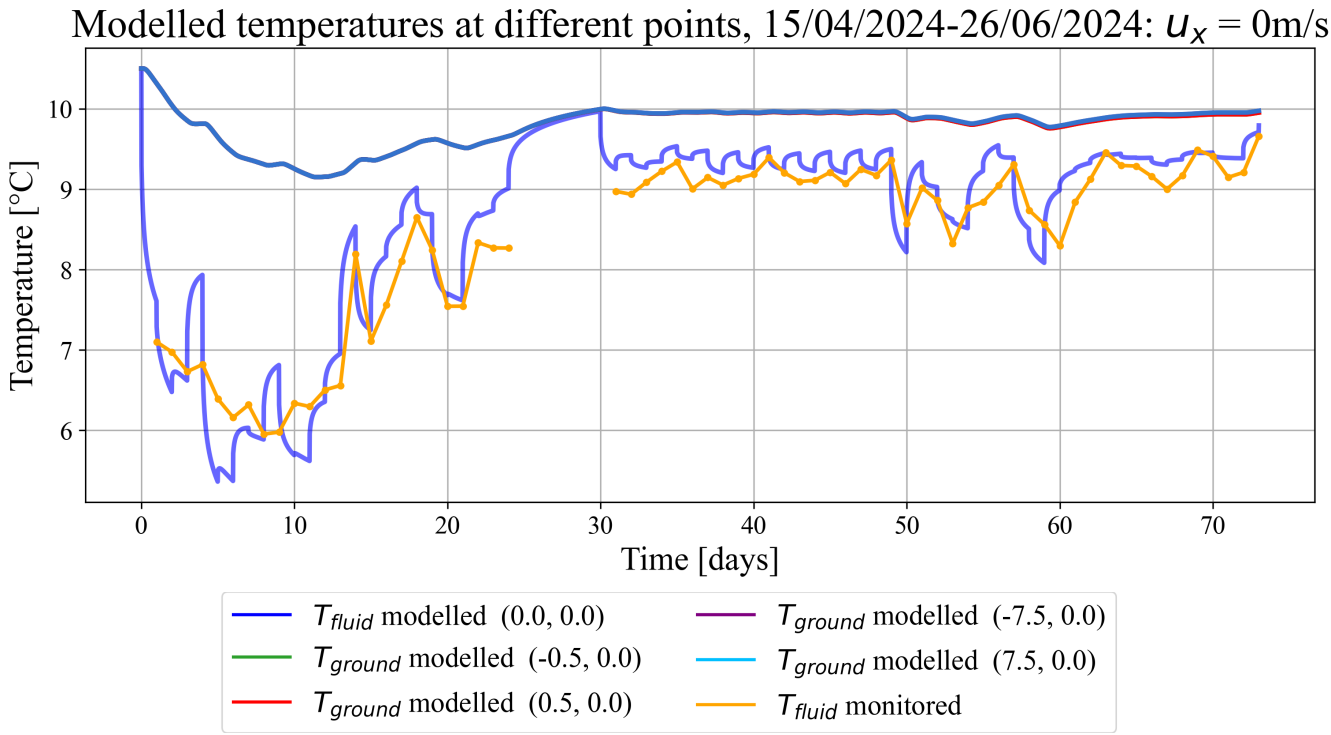

FIGURE A.20: Modelled temperature evolution at multiple observation points located inside and outside the boreholes, and the monitored fluid temperature evolution, for a groundwater specific discharge of 0 m/s.

FIGURES A.21 and A.22 show the modelled temperature evolution at different external observation points for daily and hourly thermal loads, respectively. These plots allow for a better comparison between the curves and highlight the similarities and differences in temperature evolution depending on the observation point considered.

FIGURES A.23 and A.24 illustrate the results discussed in SECTION 6.6.2, and respectively present the modelled fluid temperature evolutions at the centre of each borehole without and with groundwater flow.

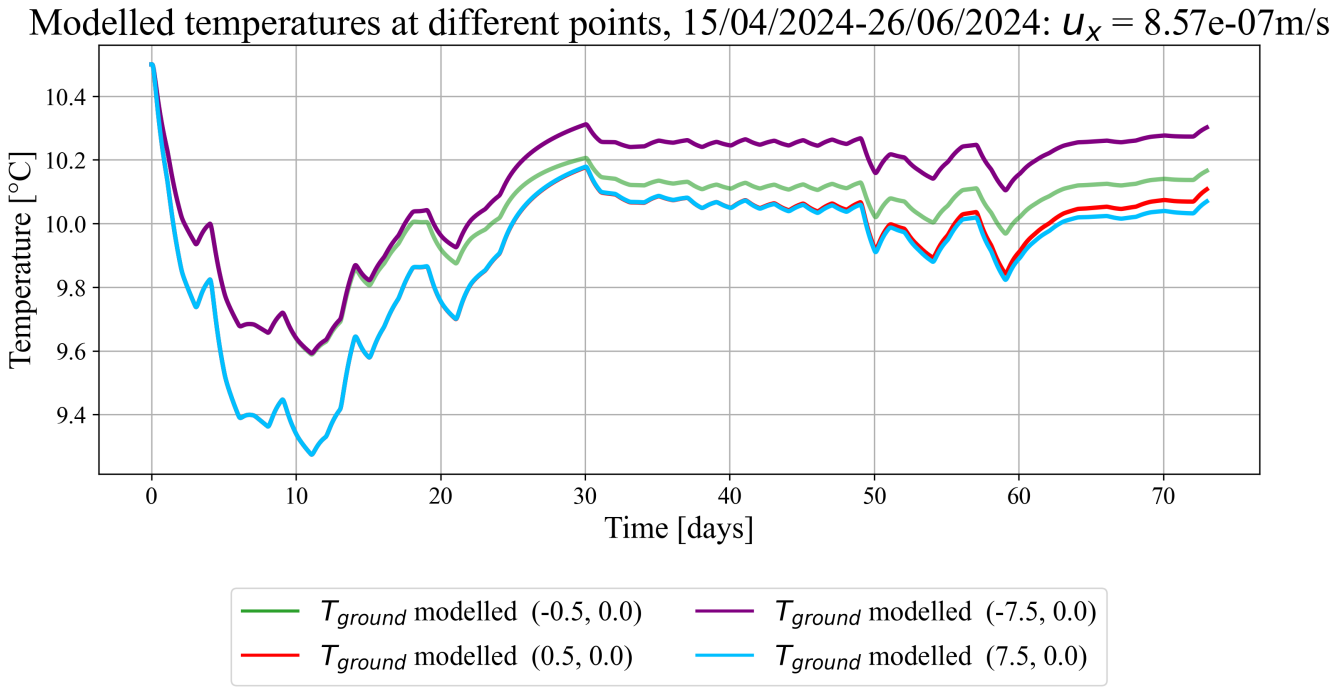

FIGURE A.21: Comparison of modelled ground temperature evolution at different external observation points, using daily thermal loads and a groundwater specific discharge of $8.57 \cdot 10^{-7}$ m/s.

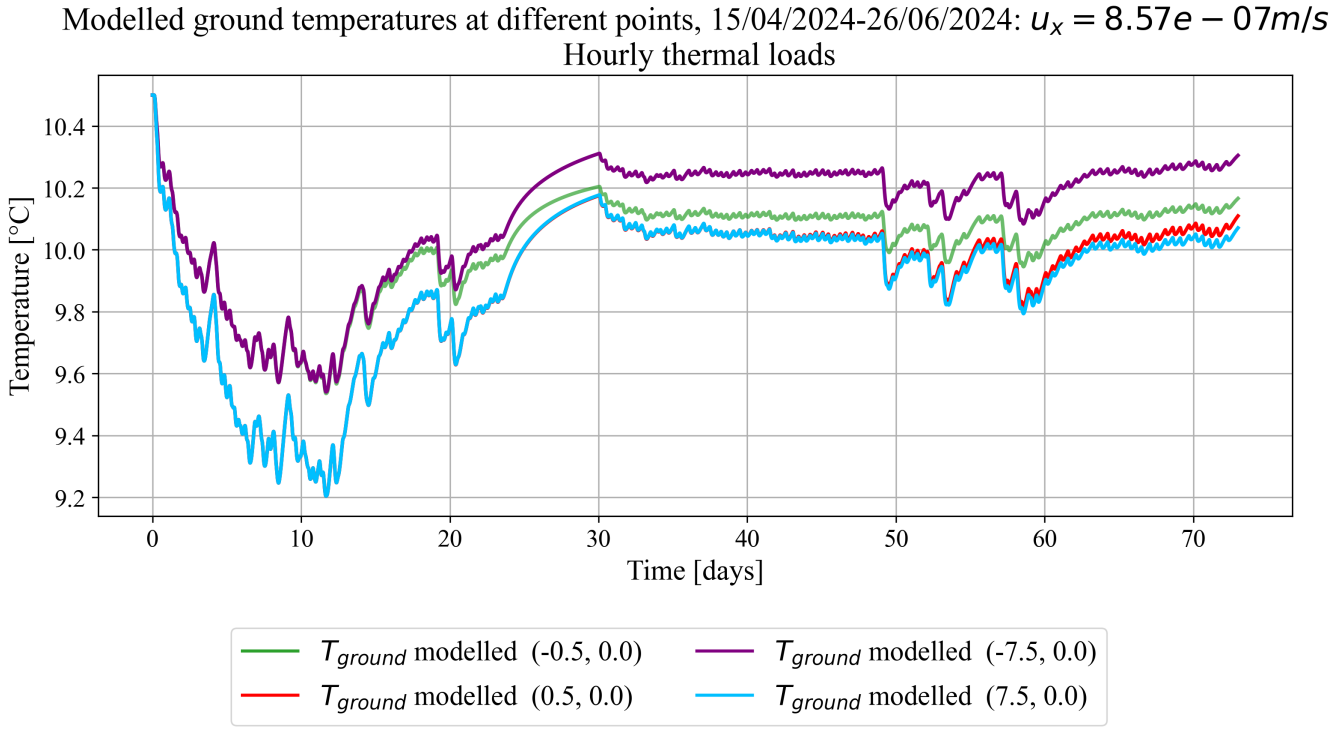

FIGURE A.22: Comparison of modelled ground temperature evolution at multiple external observation points, using hourly thermal loads and a groundwater specific discharge of $8.57 \cdot 10^{-7}$ m/s.

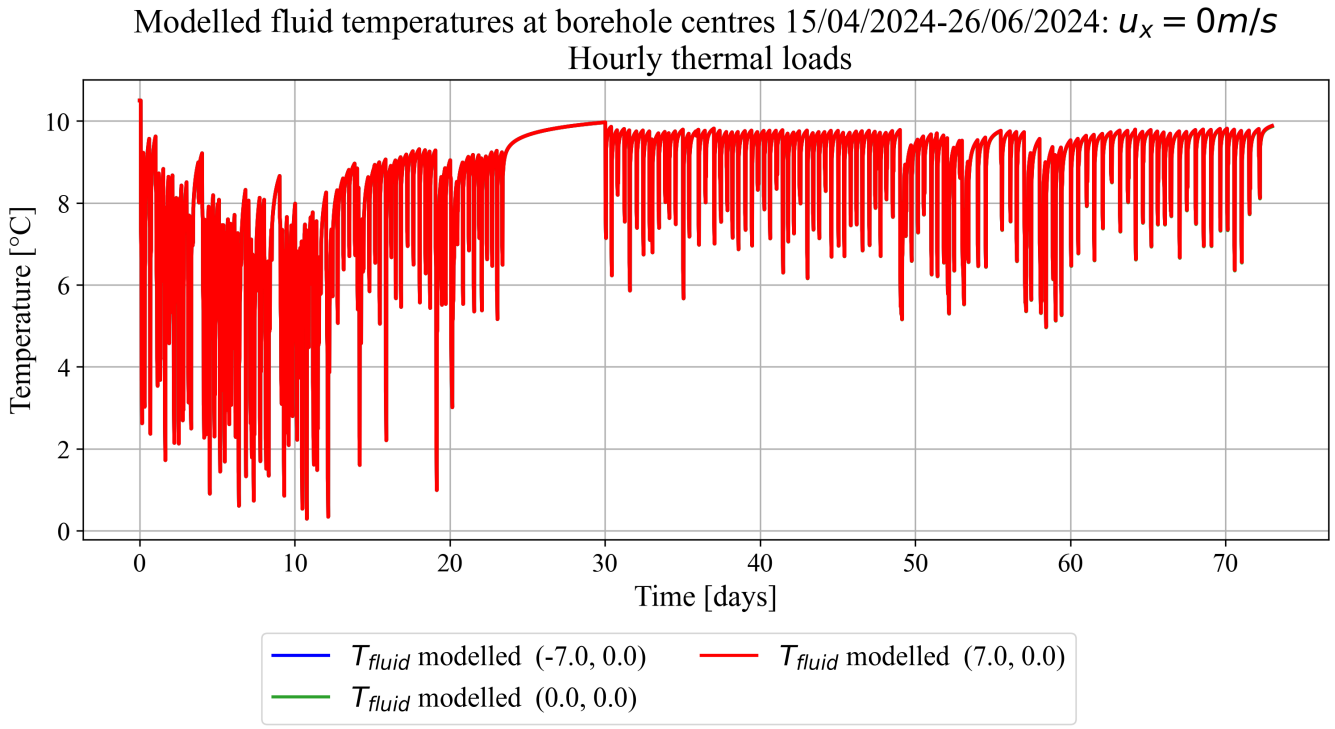

FIGURE A.23: Modelled fluid temperature evolution at the centre of each borehole in the absence of groundwater flow ($u_x = 0$ m/s), using hourly thermal loads.

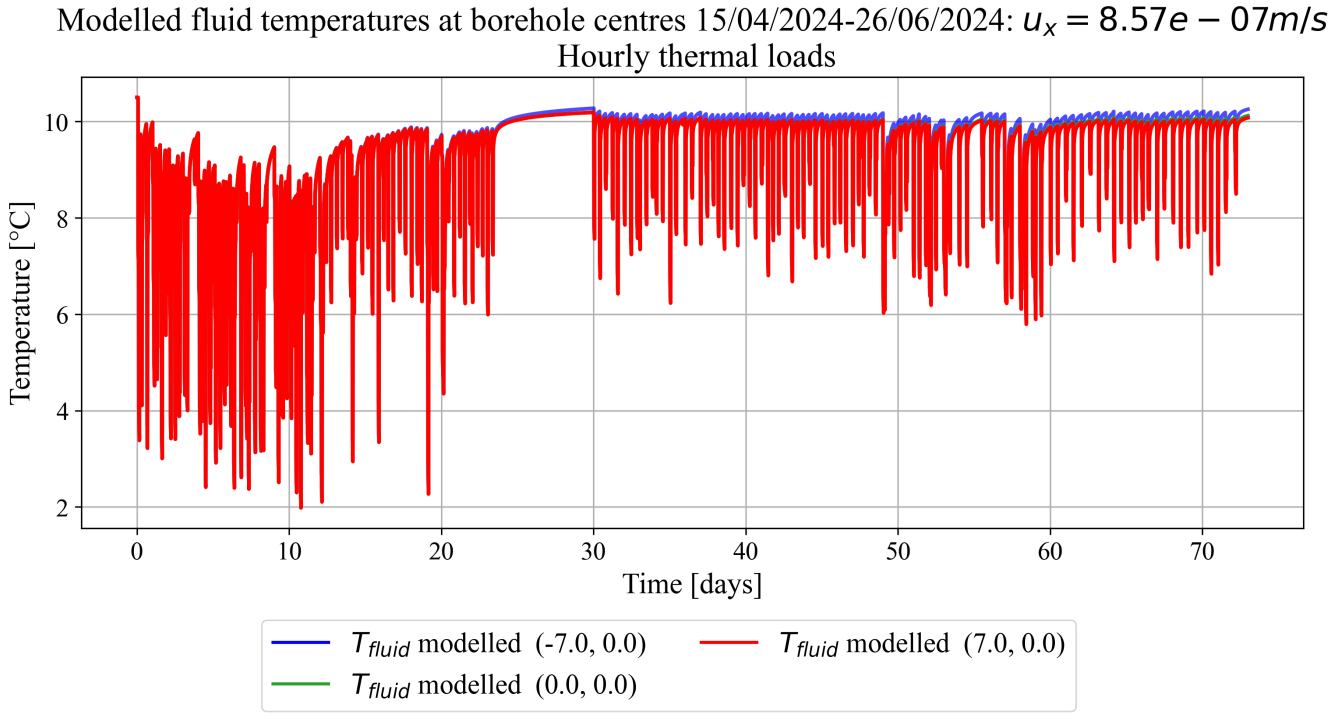

FIGURE A.24: Modelled fluid temperature evolution at the centre of each borehole with a groundwater specific discharge of $u_x = 8.57 \cdot 10^{-7}$ m/s, using hourly thermal loads.